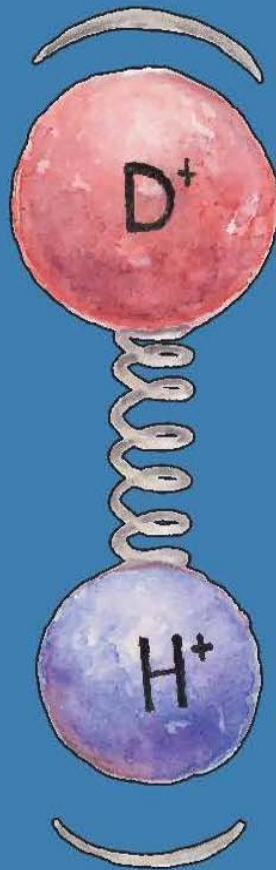


Probing **QED** and fundamental constants through vibrational spectroscopy of **HD⁺**



Jurriaan Biesheuvel

**Probing QED and fundamental constants
through vibrational spectroscopy of HD⁺**

ISBN:978-94-028-0156-9

Printed by: Ipskamp Drukkers B.V., Enschede



The work described in this Thesis was carried out at LaserLaB-VU and the Department of Physics and Astronomy at the Vrije Universiteit Amsterdam, and was funded by the ‘Stichting FOM’ through program nr. 125 ‘Broken Mirrors & Drifting Constants’, and in part by the COST ACTION MP1001 ‘Ion Traps for Tomorrow’s Applications’.

Cover: The figure on the front cover is a representation of a vibrating HD^+ molecule. At the back, the molecule has been dissociated into a D^+ ion and an H-atom. This dissociation process is used as part of a detection method in the research described in this Thesis. The cover is designed by Myrthe Biesheuvel and Elvia Villalta Sancho.

VRIJE UNIVERSITEIT

**Probing QED and fundamental constants
through vibrational spectroscopy of HD⁺**

ACADEMISCH PROEFSCHRIFT

ter verkrijging van de graad Doctor aan
de Vrije Universiteit Amsterdam,
op gezag van de rector magnificus
prof.dr. V. Subramaniam,
in het openbaar te verdedigen
ten overstaan van de promotiecommissie
van de Faculteit der Exacte Wetenschappen
op dinsdag 28 juni 2016 om 15.45 uur
in het auditorium van de universiteit,
De Boelelaan 1105

door

Jurriaan Biesheuvel

geboren te Amsterdam

promotor: prof.dr. W.M.G. Ubachs
copromotor: dr. J.C.J. Koelemeij

This thesis was approved by the members of the reviewing committee:

Prof. dr. L. Hilico

Laboratoire Kastler Brossel, UPMC-Sorbonne Universités, Paris, France

Département de Physique, Université d'Evry Val d'Essonne, Evry, France

Prof. dr. J. Oomens

Radboud University Nijmegen, Netherlands

Dr. O.O. Versolato

Advanced Research Center for Nanolithography, Amsterdam, Netherlands

Prof. dr. S. Willitsch

University of Basel, Basel, Switzerland

Dr. L. Willmann

Van Swinderen Institute, University of Groningen, Netherlands

Contents

1	Introduction	1
1.1	The HD ⁺ molecule	1
1.2	Motivation	2
1.3	Quantum Electrodynamics	3
1.4	Calculations of few-body molecules	4
1.5	Spectroscopy experiments in molecular hydrogen ions	6
1.6	New physics	8
1.7	Outline of this thesis	9
2	Experimental setup	11
2.1	Paul traps	11
2.2	Ion motion in a Paul trap	12
2.3	Linear Paul trap in this experiment	14
	2.3.1 Helical resonator	16
	2.3.2 Stabilization of dc voltages on electrodes	17
2.4	Vacuum housing and trap mount	18
2.5	Loading ions	20
	2.5.1 Beryllium oven	21
2.6	The UV laser-cooling system	23
2.7	Spectroscopy laser setup	25
2.8	Computer control system	25
3	Widely tunable laser frequency offset lock with 30 GHz range and 5 THz offset	27
3.1	Introduction	28
3.2	Experimental setup and principle of operation	29
3.3	Results and discussion	34
	3.3.1 Frequency calibration	34
	3.3.2 Fast linear scanning and frequency reproducibility: demonstration through I ₂ spectroscopy	35

3.3.3	Reproducible frequency tuning: application to a beryllium laser cooling experiment	37
3.4	Conclusion	38
4	High-precision spectroscopy of the HD⁺ molecule at the 1-p.p.b. level	39
4.1	Introduction	40
4.2	Theory	41
4.2.1	Calculation of ro-vibrational frequency transitions in HD ⁺	41
4.2.2	Hyperfine structure and rotational states	41
4.2.3	Determination of transition rates	43
4.3	Experiment	45
4.3.1	Trapping and cooling Be ⁺ and HD ⁺	45
4.3.2	Spectroscopy of HD ⁺	45
4.4	Results and Discussion	49
4.4.1	A spectral lineshape model	49
4.4.2	Estimation of absolute trapped ion numbers	52
4.4.3	Effect of micromotion	54
4.4.4	Effects of chemistry in the Coulomb crystal	57
4.4.5	Background gas reactions	65
4.4.6	Spectrum, systematic effects and final result	68
4.5	Conclusion	74
5	Probing QED and fundamental constants through laser spectroscopy of vibrational transitions in HD⁺	77
5.1	Introduction	78
5.2	Results	78
5.2.1	Experimental Procedure	78
5.2.2	Line shape model for nonlinear least-squares fitting	79
5.2.3	Systematic effects and frequency value	79
5.2.4	Discussion	84
5.3	Supplementary methods informations	87
5.3.1	Experimental procedure	87
5.3.2	Spectral line shape function for fitting	89
Appendix A	Molecular dynamics simulations	93
Appendix B	Derivation of the non-linear fluorescence function	95
Appendix C	Micromotion fit function	99
Appendix D	Stark shift calculations	103

CONTENTS

Bibliography	105
Publications	117
Summary	119
Samenvatting	121
Acknowledgements	123

Introduction

1.1 The HD^+ molecule

This thesis concerns a test of fundamental physics through a high precision measurement on the HD^+ molecule. This molecule consists of a proton, a deuteron and an electron which are held together by the electromagnetic force. The proton and deuteron in turn, are composed of quarks which are bound by the strong nuclear force. Today, quarks and electrons are considered as elementary particles which by definition contain no substructure. According to quantum field theory, both elementary particles and forces can be phenomenologically described as ‘excitations of quantum fields’ and string theory considers them as multi-dimensional vibrating strings with sizes of order 10^{-33} m. Although these descriptions cover a faithful model of nature at the smallest scale, they serve better as mathematical concepts rather than phenomenological ideas and therefore, when depicting a particle, dots, balls or clouds are used. Figure 1.1 shows three different representations of our system of interest: HD^+ . These figures give a qualitative picture of the phenomenon ‘ HD^+ molecule’ and each representation depicts another intrinsic property. Figure. 1.1a shows its properties of angular momentum (including the particle spins and molecular rotation), while Fig. 1.1b shows the two nuclei connected by a helical spring implying the possibility of vibration. The cloud figure of Fig. 1.1c represents the probabilistic nature of the spatial position of the constituents.

At room temperature HD^+ molecules will rotate but none of them will vibrate (at least in a classical picture), i.e. the molecules are in the vibrational ground state $v = 0$. If sufficient energy is added, they can undergo transitions to vibrationally excited states. For example, at a temperature of 2000°C a small fraction of the molecules will vibrate (in $v = 1$ or $v = 2$). The main topic in this thesis is an experiment in which the energy required to excite the

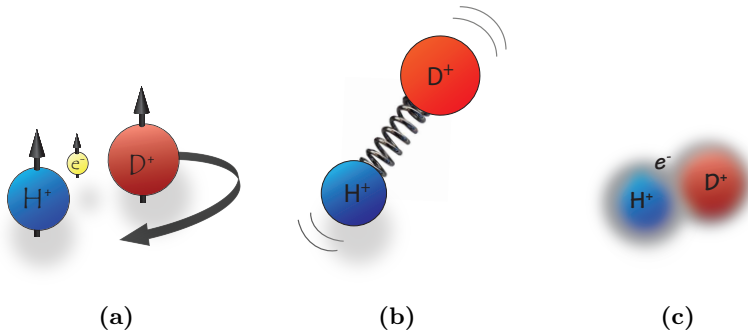


Figure 1.1: Three different representations of the HD^+ molecule.

HD^+ molecule from $v = 0$ to $v = 8$ is measured. This ‘vibrational transition’ is carried out by exciting HD^+ with an infrared laser of 782 nm wavelength. In this transition also the rotational state changes, and thus the name ‘ro-vibrational transition’ is actually more suitable.

1.2 Motivation

Molecular hydrogen ions like H_2^+ and HD^+ are the simplest molecular systems and therefore calculations on such systems can be performed with high accuracy. Today the precision of calculations of such three-body molecules lies at the 10^{-11} level [1, 2]. Owing to currently available techniques like laser cooling, ion trapping, laser frequency stabilization and frequency comb technology, measurements on molecular hydrogen ions can in principle be performed with accuracies at a similar scale as the precision of calculations. An advantageous property of HD^+ is its electric dipole moment, which enables the possibility to induce electric dipole transitions between vibrational states. By comparing high-precision theoretical results with high-precision experimental data, one can test the validity of a theory describing the system.

Besides testing theory, such a theory-experiment comparison can serve as a means to determine (improved) values of fundamental constants like the fine structure constant α or the proton-to-electron mass ratio μ^1 , which are independent parameters in electromagnetic theory. In case of a determination

¹Strictly speaking the proton-to-electron mass ratio is not a fundamental constant, because it contains the electron and proton masses. The former is dependent on the coupling between the electron and Higgs fields. The latter depends mostly on quark and gluon interactions described by quantum chromodynamics. But for the description of atoms and molecules at the 10^{-11} level this is of minor relevance.

of a fundamental constant, one *a priori* assumes that theory is correct, and *vice versa* for testing theory.

The HD^+ molecule is a suitable system for a new determination of μ . For vibrational and rotational transitions in HD^+ the transition frequencies approximately scale as

$$h\nu_{\text{vibr}} \sim R_\infty \sqrt{m_e/\mu_{\text{red}}} \quad h\nu_{\text{rot}} \sim R_\infty m_e/\mu_{\text{red}} \quad (1.1)$$

where μ_{red} is the reduced mass of the two nuclei, m_e is the electron mass and R_∞ the Rydberg energy. The expression m_e/μ_{red} contains the proton-to-electron and proton-to-deuteron mass ratios. The determination of the proton-to-electron mass ratio from the $(v,L):(0,2) \rightarrow (8,3)$ measurement is described in Chapter 5. Besides testing existing theories, high precision measurements in HD^+ can provide constraints on new physical theories as well, which is introduced below.

Another interesting application is the realization of clocks with high stability and high accuracy. Essentially a clock is a system which repeatedly sends a signal to the outside world. If this repetition rate is stable (tomorrow the same rate as today), the clock is said to be stable. Likewise, if this rate can be determined with high accuracy, the clock is said to be very accurate. The highest stabilities and accuracies are currently found in single ions clocks [3–7] and optical lattice clocks [8–12], nowadays having fractional stabilities of $\sim 10^{-16}$ at 1 s and fractional inaccuracies up to order 10^{-18} , which is nearly two orders of magnitude more accurate than cesium fountain clocks which currently define the second [13]. HD^+ or H_2^+ clocks have been proposed [14, 15] which can be used to put new constraints on temporal variation of μ in the current epoch, i.e. variation of the proton-to-electron mass ratio in time can be measured in a laboratory setup [14, 16]. Using techniques like quantum logic spectroscopy [17–19] and ro-vibrational state preparation [20, 21], realization of inaccuracies in HD^+ or H_2^+ clocks at the 10^{-16} level should become feasible, which allow searches for a temporal μ variation with sensitivities at 10^{-16} per year and below.

1.3 Quantum Electrodynamics

The theory submitted to the high-precision test described in this thesis is called *quantum electrodynamics* (QED). In this section we summarize this theory briefly in a conceptual way. A thorough but didactic explanation of quantum electrodynamics can be found in [22].

Quantum electrodynamics is a quantum field theory (QFT) developed in the late 1940s and early 1950s by (among others) Hans Bethe, Julian Schwinger, Sin-Itiro Tomonaga, Richard Feynman and Freeman Dyson [23]. It describes the electromagnetic interaction at the quantum level and incorporates both special

relativity and quantum mechanics. In ordinary quantum mechanics, observables are treated as operators, while in quantum field theory the field itself is treated as an operator. Calculations in QFT are carried out in a framework of approximations, for example, particle interactions are treated in a perturbative way using propagators and quantized path integrals. Feynman developed a tool to write down the first few orders of perturbative approximations of a scattering matrix in a diagram, which is nowadays called the Feynman diagram [24, 25].

During its initial development, QED was plagued by theoretical difficulties such as divergences and infinities appearing in integrals. Those were solved by introducing a trick called renormalization, which is intimately connected to the concept of self-energy. This means that particles can interact with virtual particles. For example, an electron may interact with a virtual photon (Fig. 1.2a) or a photon which is temporarily transformed to a virtual positron-electron pair (Fig 1.2b), which is also called vacuum polarization. These two phenomena are responsible for the famous Lamb shift, observed in 1947 by Lamb and Retherford in the hydrogen atom [26].

Despite the apparent approximative characteristic, QED has been tested with very high precision in several kinds of experiments. The group of Gabrielse determined in 2008 the electron g -factor, which relates the electron spin to its magnetic moment, with less than one part per trillion (1 ppt) precision, using a single electron in a Penning trap [27, 28]. Combining this result with the state of the art calculations of Aoyama *et al.* [29, 30] where 12672 Feynman diagrams of tenth order were evaluated, a new value of $\alpha^{-1} = 137.035999173(35)$ was obtained (0.25 ppb accuracy). In 2011, the group of Biraben in Paris obtained a similar result for α through the determination of the ratio of Plancks constant and the rubidium atomic mass, h/M_{Rb} , by measuring Bloch oscillations in rubidium atoms [31]. Here the relation

$$\alpha^2 = \frac{2R_\infty}{c} \frac{M_{\text{Rb}}}{m_e} \frac{h}{M_{\text{Rb}}} \quad (1.2)$$

was used, which led together with the most up to date determinations of M_{Rb} [32, 33], to a new value of $\alpha^{-1} = 137.035999044(90)$ (0.66 ppb accuracy). A combination of these experimental and theoretical results led to a test of QED theory at the sub-parts per billion level, which is far more stringent than the inventors of QED ever envisioned [28, 34].

1.4 Calculations of few-body molecules

For high-precision calculations on few-body molecules, a successful approach is to consider different regimes of physics and subsequently add their results: the non-relativistic part, which is solved by using the Schrödinger equation, relativistic corrections (obtained through the Breit-Pauli Hamiltonian to leading

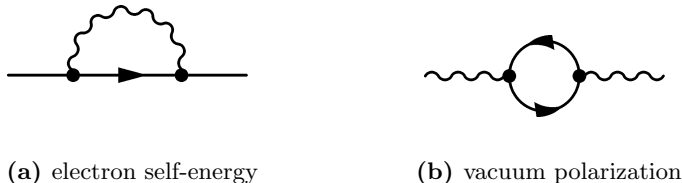


Figure 1.2: Feynman diagrams of first order contributions of a) the electron self-energy and b) photon self-energy, also called vacuum polarization.

order), radiative corrections, finite nuclear size effects and hyperfine structure. The radiative corrections contain the interactions of the molecular constituents with virtual particles (most of them described by QED) and therefore this part is often called ‘QED corrections’.

In 1993, Moss *et al.* calculated the dissociation energies of 462 states in H_2^+ and 619 states in HD^+ with a relative accuracy of $\sim 5 \times 10^{-9}$ including leading order relativistic and leading order radiative corrections (order $\alpha^2 R_\infty$ and $\alpha^3 R_\infty$ respectively) [35, 36]. The recent results of Korobov *et al.* surpass this accuracy by two orders of magnitude. In these results, calculations of molecular hydrogen ions and antiprotonic helium are presented with precisions at the 10^{-11} level including corrections up to the order $\alpha^8 R_\infty$ [1, 2]. In the remainder of this section, we give a brief overview of the customary calculation methods of the non-relativistic part. An introduction of the corrections can be found in [37, 38].

A commonly used first step for calculations of simple molecules is the Born-Oppenheimer (BO) approximation [39], in which the wavefunction of the molecule is split into a nuclear and electronic part, and in which the nuclei are considered clamped, thus ignoring their kinetic energy. Subsequently the electronic energy levels are calculated by solving the Schrödinger equation for various values of the internuclear distance. Then the motion of the nuclei subject to the electronic forces (which are a result of the determined electronic energy) is calculated. In the next step of refinement, called the adiabatic approximation (also called Born-Oppenheimer diagonal correction), the dependence of the electronic energy on the nuclear motion is included. In the ultimate step of refinement, the electronic and nuclear motions are coupled. The difference between the result of this level and the adiabatic correction is called the non-adiabatic correction. An important contribution to non-adiabatic correction methods is the derivation of an effective Hamiltonian by Bunker and Moss based on perturbative methods, and accurate up to second order in perturbation theory [40]. Today, this method is still used to calculate energies in simple molecules.

As a three-body system, the molecular hydrogen ion distinguishes itself from

more complex molecules in that it allows an analytical solution of the Born-Oppenheimer three-body Hamiltonian [41]. However, this solution does not come in a closed form, and various methods to find approximate closed-form expressions to the solution have been developed (see, for example, Refs. [41,42], and references therein). During the late 1990s, numerical methods beyond the Born-Oppenheimer approximation were developed, giving solutions to the non-relativistic three-body problem which are essentially exact up to a certain number of digits [43,44]. Later work by various groups improved the precision [45–47], in some cases up to 30 digits [48]. However, today's most accurate theoretical predictions are based on the numerical method developed initially by Korobov [44].

An alternative method for high precision calculation on molecules is the use of the Dirac equation which makes the need for relativistic corrections unnecessary because this equation incorporates special relativity [49,50]. This method seems attractive at first hand, but fundamental complications arise due to the fact that the Dirac equation is a one-particle equation and HD^+ consists of three bodies. This introduces a problem with the definition of time, since each body has a different inertial system. Therefore, only one constituent, for example the electron, can be described by the Dirac equation and for the nuclei customary relativistic corrections are still required. Another approach to circumvent this problem is an effective field theory called non-relativistic QED (NRQED), which has been successfully used for the molecular hydrogen ion (see for example [51]).

1.5 Spectroscopy experiments in molecular hydrogen ions

Of all molecules, neutral hydrogen, H_2 , is the most abundant molecular species in the universe. Together with its isotopomer HD it plays an important role in astrophysics and cosmology. Molecular hydrogen serves as a main cooling agent during formation of stars and gas condensation because kinetic energy can be efficiently absorbed in their rich structure of rotational and vibrational energy levels. Due to the presence of many strong lines in their spectra, neutral hydrogen molecules are attractive objects of study and they have been extensively studied by astronomical observations and laboratory experiments.

Interstellar concentrations of ionic hydrogen molecules however, are much lower. One cause is the efficient reaction of H_2^+ with H_2 to the relatively stable species H_3^+ [52,53]. Furthermore, their spectral lines are weak due to forbidden ro-vibrational and electronic transitions (due to selection rules and Franck-Condon overlap respectively). The densities of HD^+ are even a much lower than the H_2^+ densities due to the D/H ratio of 10^{-4} – 10^{-5} in the universe. Thus both,

in interstellar clouds and laboratory setups, the number of ionic species stays far behind the numbers of neutrals and they are much harder to observe. For these reasons, spectroscopy on molecular hydrogen ions have remained elusive for a long period, and significant achievements were not obtained before the invention of suitable lasers, ion beam and ion trapping techniques.

The first spectroscopic measurements on H_2^+ were carried out by Jefferts in 1969, who measured 30 magnetic rf transitions between hyperfine levels in ro-vibrational states [54,55]. In this experiment, a linear quadrupole trap was used for ion trapping and a mercury lamp for photodissociation. Based on these results the coefficients of the spin Hamiltonian of H_2^+ were determined. The 1.5 kHz experimental uncertainty challenged theorist for nearly five decades, and only very recently the observations of Jefferts could be explained by theory within the experimental uncertainty [56]. Some years later in 1976, six ro-vibrational lines in HD^+ were measured by Wing *et al.* [57] with 1 part-per-million accuracy and partially resolved hyperfine structure.

An important contribution in the development of molecular hydrogen ion spectroscopy and theory is the work of Carrington *et al.* [58–62], which has been carried out in the 1980s and early 1990s but is still considered as a benchmark in the field. This work includes measurements as well as calculations of microwave and infrared spectra belonging to high v and high L ro-vibrational or electronic transitions in HD^+ and D_2^+ . Also the nuclear hyperfine structure in the electronic transition $2p\sigma_u(v, L) = (0, 2) \rightarrow 1s\sigma_g(v, L) = (18, 3)$ in H_2^+ has been measured. With theoretical and experimental accuracies in the order of 0.0001 cm^{-1} these results provided the most stringent tests of theory of 3-body molecules at that time.

More than a decade later, in 2007, Koelemeij *et al.* performed laser spectroscopy of the $(v, L): (0, 2) \rightarrow (4, 3)$ transition in HD^+ at 1395 nm with 2 ppb accuracy [63]. In 2012, the Düsseldorf group published the first detection of a purely rotational transition [21]. In the same year results on HD^+ were presented in which the individual hyperfine states of the $(v, L): (0, 0) \rightarrow (1, 1)$ transition were addressed. This led to a 1.1 ppb precision in the determination of the line center² [64].

Another approach to determine energy intervals in molecular hydrogen ions is via spectroscopy of Rydberg states of neutral molecules. This was recently demonstrated by Haase *et al.* [65]. By using multichannel quantum-defect theory (MQDT) [66, 67] spectroscopic results could be extrapolated to a pure rotational energy splitting in para- H_2^+ .

²This result differs by 2.4σ from the theoretical prediction [2] of this line.

1.6 New physics

The physics describing electronic, vibrational and rotational transitions in light molecules is fully described by effects of electromagnetism, i.e. by QED theory. The effects of the other forces, strong, weak and gravity, are many orders of magnitude smaller than the uncertainties of both experiment and QED theory and are therefore negligible. This means that any presence of new physics in a molecule could be measured as a deviation from QED theory. Analogous to the Cavendish torsion experiment detecting gravitation between lead spheres [68], hypothetical ‘fifth forces’ at the Ångström scale could be measured in diatomic molecules like H_2 , D_2 , H_2^+ and HD^+ . In [69] and [70] Salumbides *et al.* explain that one can put new constraints on the existence of fifth forces between hadrons by measuring the ro-vibrational transitions in diatomic molecules, while searching for deviations between experiment and (QED) theory.

In quantum field theory, each fundamental interaction is mediated through gauge bosons, which means that any force can be phenomenologically parameterized by a Yukawa-type potential,

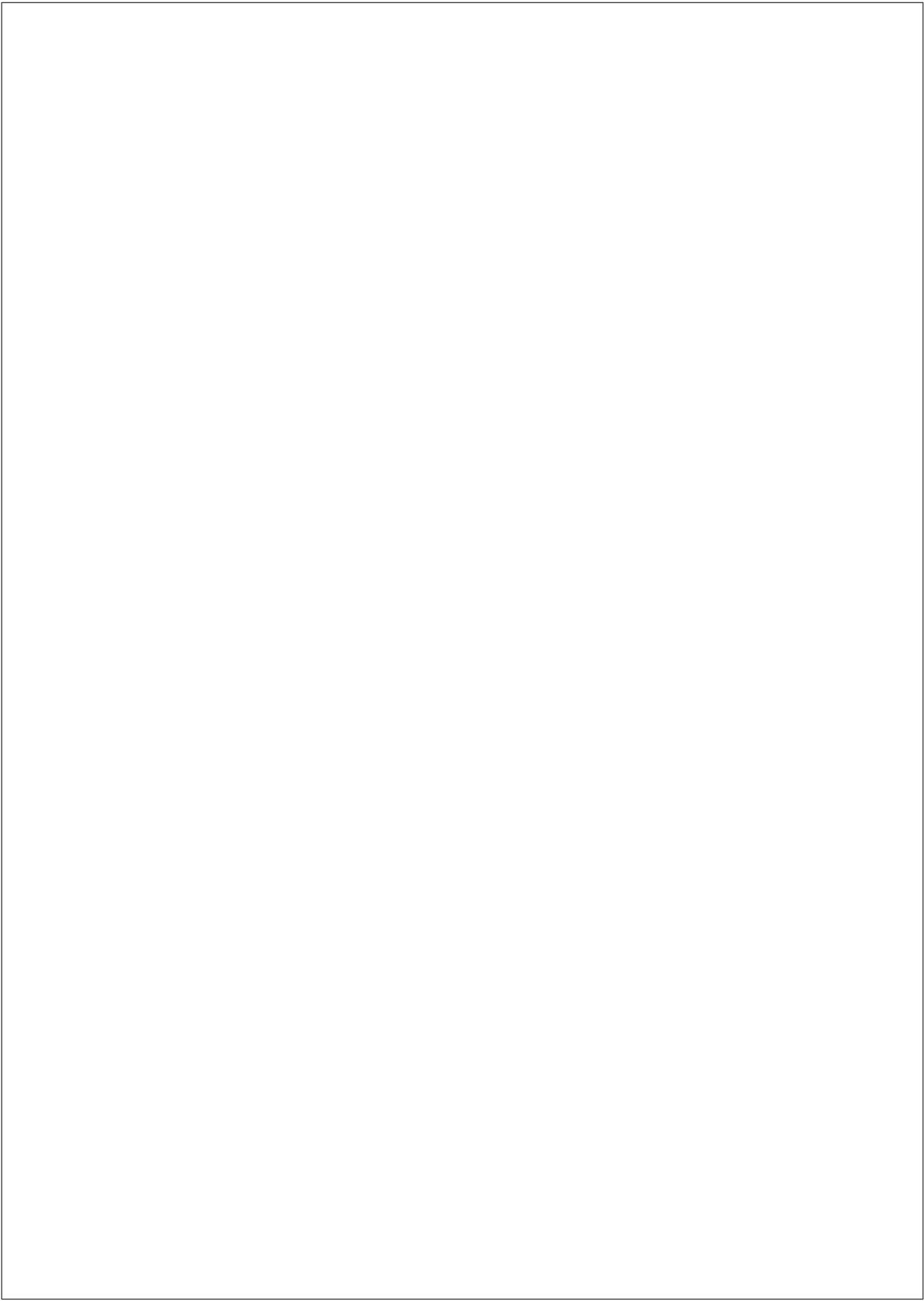
$$V_5(r) = \alpha_5 \frac{\exp(-r/\lambda)}{r} \hbar c \equiv \alpha_5 Y(r), \quad (1.3)$$

where α_5 is the coupling strength and λ the effective range of the force related to the mass m_γ of the gauge boson by $\lambda = \hbar/m_\gamma c$. Considering ro-vibrational transitions in diatomic molecules, energy contributions $\langle V_5 \rangle$ originating from a fifth-force potential can be calculated from perturbation theory. Combining this with experimental measurement uncertainties, new limits can be set on the strength of the coupling constant α_5 . Although the $\langle V_5 \rangle$ sensitivity in transitions in neutral hydrogen molecules is higher, the current precision of both theory and experiment in the ionic species HD^+ is an order of magnitude better, and the latter give the tightest constraints on α_5 and λ .

Not only hypothetical fifth forces can be probed with molecular hydrogen. String theory predicts the presence of compactified dimensions in addition to the (3+1) observable ones. According to the framework of Arkani-Hamed, Dimopoulos, and Dvali [71] (ADD model) molecular hydrogen molecules can be used to set constraints on the compactification radii of extra dimensions [72]. In addition, another theory called the Randall-Sundrum models [73, 74] (RS scenarios) can be used in combination with molecular spectroscopy data to derive limits on the curvature of space due to branes which may be hiding in higher dimensions, and on the separation between ‘our’ brane and the hidden brane.

1.7 Outline of this thesis

In Chapter 2 the setup of the HD^+ experiment is described. First, the concept of ion traps is introduced, followed by the derivation (and solution) of the equations of motion of a single trapped ion. Chapter 3 describes a novel widely tunable offset lock used in the 626 nm laser system, which is an essential part of the laser cooling system. The content of this chapter has been published in Optics Express [75]. Chapter 4 forms the core of this thesis and presents the high precision spectroscopy measurement on HD^+ in detail. Here the spectroscopic data and the model which constructs the fit function of the $(0,2) \rightarrow (8,3)$ spectrum is explained, and various systematic effects that play a role in the spectroscopy are discussed. In Chapter 5, where this measurement is discussed in concise form, the determination of a new value for μ and new constraints of hypothetical fifth forces based on the spectroscopic results are presented. This chapter has been published in journal Nature Communications [76].



Experimental setup

2.1 Paul traps

From Earnshaw's theorem¹ [77] it follows, that one cannot trap a charged particle using dc electric fields only. This problem can be circumvented using additional magnetic fields or an ac electric field in at least one direction. In the 1950s, Wolfgang Paul developed the quadrupole ion trap [78], today also called 'Paul trap' or 'rf trap', which operates through a quadrupole ac electric field that establishes a ponderomotive trapping force for positively charged particles. Such particles, like ions, can be stored in a Paul trap for an, in principle, infinite amount of time. In practice, the trapping duration is dependent on the reaction rate of an ion with molecules from the background gas. In 1989, Paul received the Nobel Prize in Physics 'for the development of the ion trap technique'. Nowadays, many kinds of Paul traps have been developed, like hyperbolic traps, linear traps, planar traps, or 22 pole traps. Besides high precision spectroscopy, typical purposes for which Paul traps are used are high resolution mass spectroscopy [79], studies of ion-neutral reactions [80,81], quantum computing [82–85], or establishing ion clocks [4]. Experiments at CERN use ion traps to study anti-matter, for example in the GBAR experiment (Gravitational Behaviour of Anti hydrogen at Rest) where an ultracold antihydrogen ion, *i.e.* $\bar{p}e^+e^+$, is trapped in a Paul trap and, after laser detachment of one positron, the free fall acceleration of created the antihydrogen atom will be measured [86]. This will test Einstein's weak equivalence principle

¹Samuel Earnshaw developed this idea in 1839 and entitled his publication *On the nature of the Molecular Forces which regulate the Constitution of the Luminiferous Ether*. He calculated the behaviour of Ether particles subjected to electric forces. This was before the concepts of electrodynamics were established and long before constituents of matter like 'atoms', 'ions' and 'electrons' were discovered.

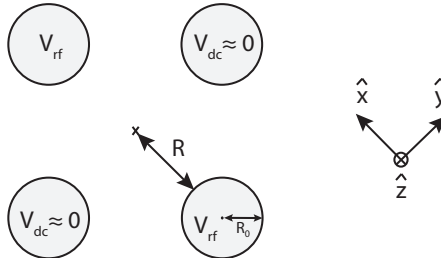


Figure 2.1: Axial view of a linear ion trap (endcaps are not shown here). The diagonally opposing electrode pairs are connected to rf and dc voltages, respectively.

(which states that the trajectory of particles only submitted to gravitational forces is independent on composition or internal structure), directly with matter and antimatter.

In this thesis we describe an experiment in which a linear Paul trap is used which consists of four cylindrical rods. Two diagonally opposing rods are connected to an rf voltage source and the other pair is connected to a dc voltage source, providing confinement of ions in radial direction (See Fig. 2.1). For axial confinement (z -direction) two pairs of dc electrodes, called endcaps, create a nearly harmonic potential at the center of the trap.

2.2 Ion motion in a Paul trap

In this section, we derive the motion of a single trapped ion, following Berkeley's treatment [87]. In general the electric potential in the radial direction of a linear Paul trap near the trap axis can be written as

$$V(x, y, t) = \frac{V_0}{2} \left(1 + \frac{x^2 - y^2}{R^2} \right) \cos(\Omega t) \quad (2.1)$$

where V_0 and Ω are amplitude and angular frequency of the rf and R' is the distance from the trap axis to the electrodes (see Fig. 2.1) and $R' \simeq R$. In the limit where the trap electrodes are hyperbolic surfaces of infinite length, $R = R'$. To approximate this condition with cylindrical rods with radius R_0 (instead of hyperbolic surfaces) as well as possible, the ratio R_0/R should be chosen close to 1.146 [88]. The axial confinement is provided by the endcap

electrodes, of which the voltages U_0 create a dc potential near the center of the trap which can be approximated by:

$$U(x, y, z) = \frac{\kappa U_0}{Z_0^2} \left[z^2 - \frac{1}{2}(x^2 + y^2) \right], \quad (2.2)$$

where κ is a geometrical factor and Z_0 is half the axial distance between the endcaps. From Eqs. (2.1) and (2.2) we obtain the electric field

$$\begin{aligned} \mathbf{E}(x, y, z, t) = & -V_0 \left(\frac{x\hat{x} - y\hat{y}}{R^2} \right) \cos(\Omega t) \\ & - \frac{\kappa U_0}{Z_0^2} [2z\hat{z} - x\hat{x} - y\hat{y}]. \end{aligned} \quad (2.3)$$

Newtons second law, in the form of $E_i Q = m\ddot{u}_i$, gives us the equations of motion for a single trapped ion with charge Q and mass m :

$$\ddot{u}_i + [a_i + 2q_i \cos(\Omega t)] \frac{\Omega^2}{4} u_i = 0, \quad (2.4)$$

where $\mathbf{u} = u_x\hat{x} + u_y\hat{y} + u_z\hat{z}$ is the position of the ion with respect to the minimum of the trap potential, and

$$a_x = a_y = -\frac{1}{2}a_z = -\frac{4Q\kappa U_0}{mZ_0^2\Omega^2}, \quad (2.5)$$

and

$$q_x = -q_y = \frac{2QV_0}{mR^2\Omega^2}, \quad q_z = 0. \quad (2.6)$$

Equation (2.4) is called the Mathieu equation, named after Émile Léonard Mathieu².

If we take $q_i \ll 1$ and $a_i \ll 1$, which is typically the case, the first-order solution of the Mathieu equation is

$$u_i(t) \approx u_{1i} \cos(\omega_i t + \phi_{Si}) \left[1 + \frac{q_i}{2} \cos(\Omega t) \right], \quad (2.7)$$

where $\omega_i \simeq \frac{\Omega}{2} \sqrt{a_i + \frac{1}{2}q_i^2}$ and ϕ_{Si} is a constant phase offset which is determined by the initial position and velocity conditions. The term ω_i represents the secular motion of a trapped ion while the $\cos(\Omega t)$ term corresponds to the micromotion.

The values for a_i and q_i which provide stable and unstable solutions for ions can be expressed in a stability diagram. Figure 2.2 shows the values of these parameters in two dimensions for the case of an infinitely long linear Paul trap.

² Mathieu introduced this equation in 1868 in order to calculate the motion of vibrating elliptical drumheads. Ion traps were unknown at that time.

2. EXPERIMENTAL SETUP

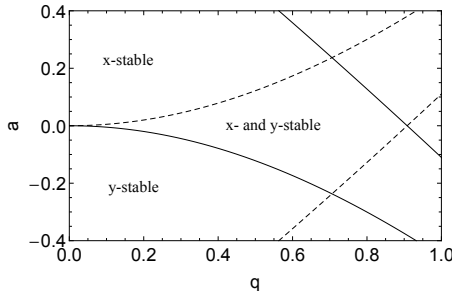


Figure 2.2: Stability diagram of an infinitely long linear Paul trap in two dimensions. Stability regions occur also for larger values of a and q , but only the lowest stability region is shown here. The dashed and solid lines correspond to the boundaries of stable solutions of the Mathieu equation in the y and x -directions, respectively.

To lowest order, the pseudopotential is given by $\frac{1}{2}m\omega_i^2 r^2$. Obviously trapped particles will be lost if they hit the electrodes, so an upper limit to the trap depth is approximately given by $\frac{1}{2}\omega_i^2 R^2$. Note that the trap depth depends on the charge-to-mass ratio of the trapped particles, which is used to selectively remove heavy impurity ions from the trap (see Sec. 4.3).

In ion traps one often deals with multiple ions trapped at the same time. For sufficiently cold ensembles, such that crystallization occurs, the amplitudes of the secular motion of each ion in the crystal can be obtained from solving the eigenfrequencies and eigenmodes of the system (see for example [89]). Such a treatment is valid for ion crystals with temperatures of order 1 mK. For warmer ion ensembles (temperature $\gg 1$ mK), in which individual ions may have sufficient energy to hop from lattice site to lattice site and the crystal becomes partly melted, molecular dynamics (MD) simulations provide a more realistic prediction of the ion motion (Appendix A).

2.3 Linear Paul trap in this experiment

We use a linear Paul trap that consists of four cylindrical molybdenum rods with a length of 60 mm and a diameter of 8.0 mm, of which two diagonally opposing rods are connected to a 13.2 MHz rf voltage source. With $R = 3.5$ mm, the ratio $R_0/R = 1.14$, which is close to the optimum value of 1.146 (Sec. 2.2). The rf amplitude at the location of the ions is about 270 V. The other pair of opposing rods is segmented into five parts of 12 mm length. Each of the segments is ac-coupled to ground (Fig. 2.6), so that, controlled dc voltages can be applied which can be adjusted individually while keeping each electrode at rf ground at all times. This arrangement allows compensating stray electric

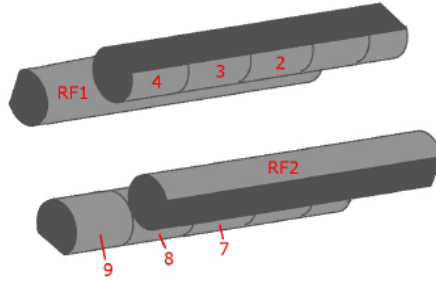


Figure 2.3: Schematic three-dimensional representation of the ion trap electrodes. The two rf electrodes are connected to an rf voltage source oscillating at 13.2 MHz frequency. The other labeled electrodes are ac-coupled to rf ground, and connected to dc voltage sources. With electrode pairs 2,7 and 4,9 configured as endcaps the ions are trapped in between electrodes 3 and 8.

fields due to excess charge that may have accumulated at parts nearby the ions. Only the first three pairs of segments are operational during ion trapping. A schematic drawing of the trap is shown in Fig. 2.3, and a picture of the trap (taken during maintenance of the trap) is shown in Fig. 2.4.

Electrode numbers 2, 7, 4 and 9 serve as endcap electrodes which are connected with a dc voltage of 4 V, and provide confinement in the axial direction. Near the center of the trap the potential is approximately harmonic. Note that since the 4 V endcap voltage is applied to only two of the four rods, the endcap potential at the trap axis is only ~ 2 V. A finite-element analysis performed in SIMION 6.0 yields (with $Z_0 = 6$ mm) a geometric factor $\kappa = 0.144$, so that for an endcap voltage of 4 V the axial frequencies of Be^+ and HD^+ become 93 kHz and 161 kHz, respectively. The center electrode pair (numbers 3 and 8) is connected to ~ 0 V with respect to ground. Electrode number 3 is connected to an rf source producing frequencies in the range of 0.1-2 MHz which are used to excite the secular motion of the trapped ion species. In this trap, secular excitation frequencies of Be^+ and HD^+ ions are obtained at ~ 290 kHz and ~ 830 kHz respectively.

Phase differences between the two rf channels in the order of one degree can lead to ion micromotion heating which leads to temperatures of hundreds of mK [87]. To minimize this effect, the two rf circuits at the electrical feed through of the vacuum chamber leading to the rods are electrically connected by 3 μF ceramic capacitors (with electrical leads of only a few mm length to avoid significant stray inductance); see Fig 2.5. An electrical circuit simulation performed with SPICE software shows that this measure reduces the potential phase difference to < 4 millidegrees.

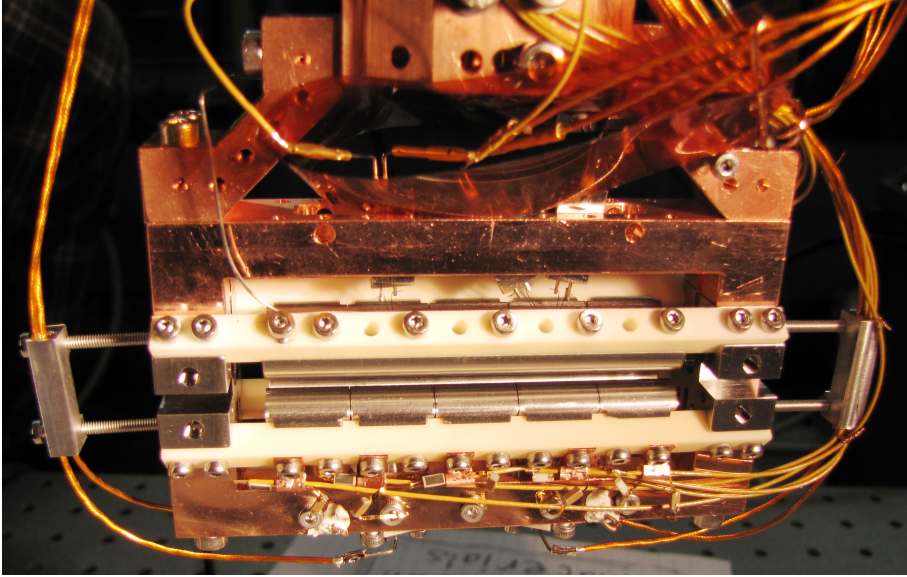


Figure 2.4: Picture of the ion trap used in this experiment, and the OFHC copper structure onto which the trap is mounted. The picture was taken after installation of three new e-guns (thoriated tungsten wires) which are mounted above the trap electrodes.

2.3.1 Helical resonator

The sinusoidal rf voltage is derived from an arbitrary waveform generator (AWG), whose amplitude and frequency can be controlled externally through a GPIB interface. The AWG output is sent through an rf amplifier, resulting in an rf amplitude of 15-20 V. To achieve the ~ 300 V needed to trap ions, the amplifier output is connected to a helical resonator, which acts as a step-up transformer (Fig. 2.5). The secondary coil of the helical resonator (which connects to the rf electrodes) is of the bifilar type, *i.e.* it consists of an identical pair of galvanically isolated wires. This allows applying different dc voltages to each of the rf electrodes. The helical resonator is placed outside the vacuum, on top of the vacuum housing. With the trap connected, the helical resonator has a Q factor of 43 and its resonance frequency is approximately 13.2 MHz. Figure 2.5 shows a schematic design of the helical resonator. The coils are shielded by an oxygen free high conductivity (OFHC) copper housing. The top of the resonator is covered by a brass disk which is tightly clamped to the shield. The disk contains a BNC feed through onto which the rf coupling antenna is mounted. Two teflon-coated wires are pressed against the two pins

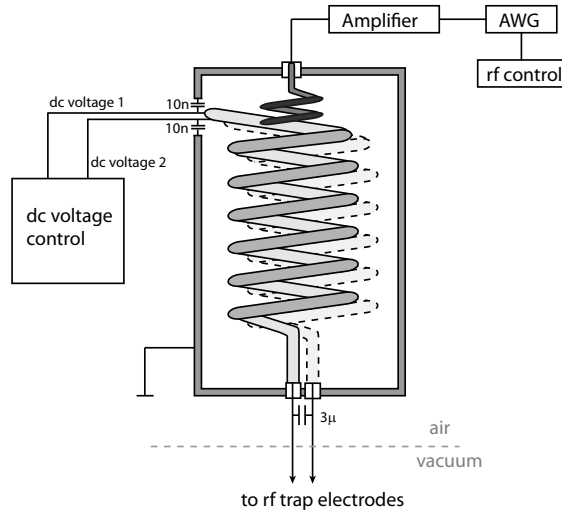


Figure 2.5: A schematic view of the helical resonator. A bifilar secondary coil (grey, with the two wires indicated by solid and dashed lines, respectively) is inductively coupled to the primary coil (black), which is connected to the rf voltage source. The dc voltages on each wire of the secondary coil can be adjusted individually.

of the vacuum feedthrough, and are guided to BNC connectors via the stainless steel vacuum flange using metallic tape. These identical wires act as rf pick-up antennae and are used to estimate the phase and amplitude at the rf electrodes in the trap. The pick-up antennae were calibrated for a wide range of rf voltages before the installation of the helical resonator.

2.3.2 Stabilization of dc voltages on electrodes

To realize an rf ground at the dc electrodes, each dc electrode is connected to an RC filter with the resistor placed in the dc path (Fig. 2.6a). The values of the components are selected such that a corner frequency of 1.6 kHz is achieved, well below the 13.2 MHz rf frequency. Moreover, only voltages with Fourier components below this value are efficiently transmitted from the dc voltage

source to the trap electrodes, thus suppressing possible voltage noise at secular trap frequencies which are typically in the range 50-900 kHz.

With a capacitor value of 1 nF, a resistor value of 100 k Ω is required yields the 1.6 kHz corner frequency. However, during loading of ions by electron bombardment (Sec. 2.5), the emission current of the electron gun is dissipated mostly by the trap electrodes, leading to currents up to 10 μ A. In combination with the 100 k Ω resistor, this may increase the voltage at the electrode by as much as 1 V, which is of the same order as the trap depth.

To ameliorate this effect, the trap electrodes are connected to an electrical circuit which actively stabilizes the voltage at each electrode irrespective of the current dissipated by it. This circuit is shown in Fig. 2.6 and was first described in [90].

2.4 Vacuum housing and trap mount

Figure 2.7 shows a schematic view of the stainless steel vacuum housing. The trap is mounted on an OFHC copper tube, which is mounted vertically from the top flange of the vacuum chamber. This tube consists of a tube and a (bifilar) center conductor, similar to a coaxial waveguide. The rf outputs of the helical resonator (located on the outside of the vacuum chamber) are connected to two OFHC pins of a vacuum feedthrough, which feed into the two segments of the bifilar center conductor. These segments are galvanically isolated by Kapton sheet, and connected by screws made of alumina (amorphous Al_2O_3) ceramic. At the end of the center conductor, the two segments are connected by two additional 1 nF chip capacitors (Novacap) placed in parallel to minimize any rf voltage and phase differences between the segments. From there, two molybdenum wires of equal length feed the rf and dc voltages of each segment to an rf conductor.

The reentrant view ports on the vacuum housing are ConFlat (CF) flanges of 150 mm outer diameter (Larson Electronic Glass, SQ-300-F6), which are sealed with 313 nm anti-reflection coated fused silica viewports with a diameter of 65 mm. Apart from apertures providing optical access parallel and perpendicular to the trap axis, the vacuum chamber is equipped with several CF 40 flanges giving optical access at an angle of 17 degrees with respect to the trap axis. One of these flanges is connected to a leak valve mechanism that is connected to an HD lecture bottle. The leak valve can be opened with a stepper motor which allows introducing small and reproducible amounts of HD gas into the vacuum. The HD gas can be ionized to HD^+ within the vacuum system (see Sec. 2.5). Below the vacuum housing, two turbo pumps and a backing pump are connected series. In addition, the vacuum chamber is fitted with a titanium sublimation pump. After a one-week bakeout of the

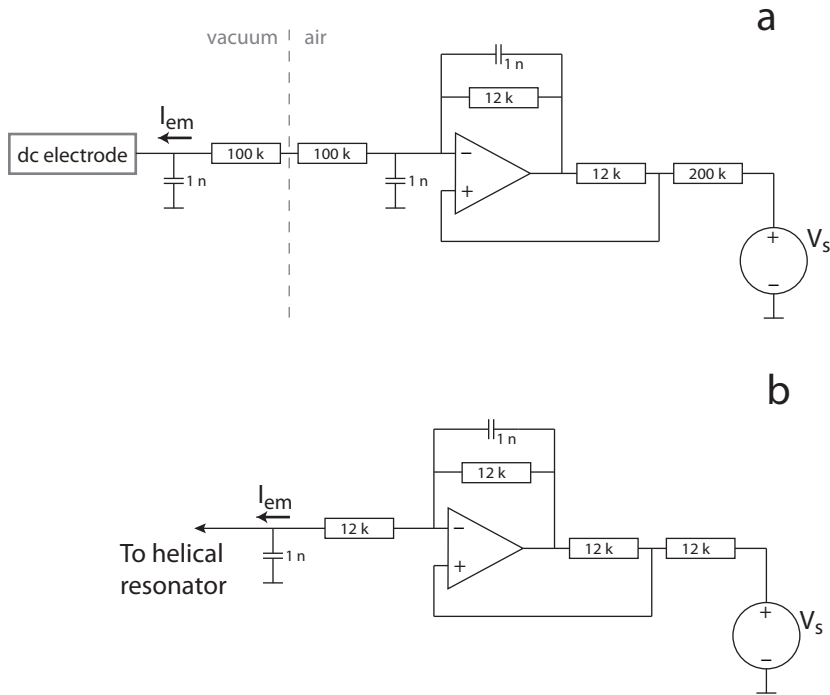


Figure 2.6: Electrode-voltage stabilization circuitries for the dc (a) and rf (b) electrodes employing an reversed operational amplifier. In case a trap electrode connected to the negative input of the operational amplifier dissipates a current I_{em} (e.g. electrons emitted by the electron gun during loading of ions), the resistors at the output of the op-amp convert the dissipated current to exactly the voltage required at the positive input terminal of the op-amp to maintain the set voltage V_s at the electrode.

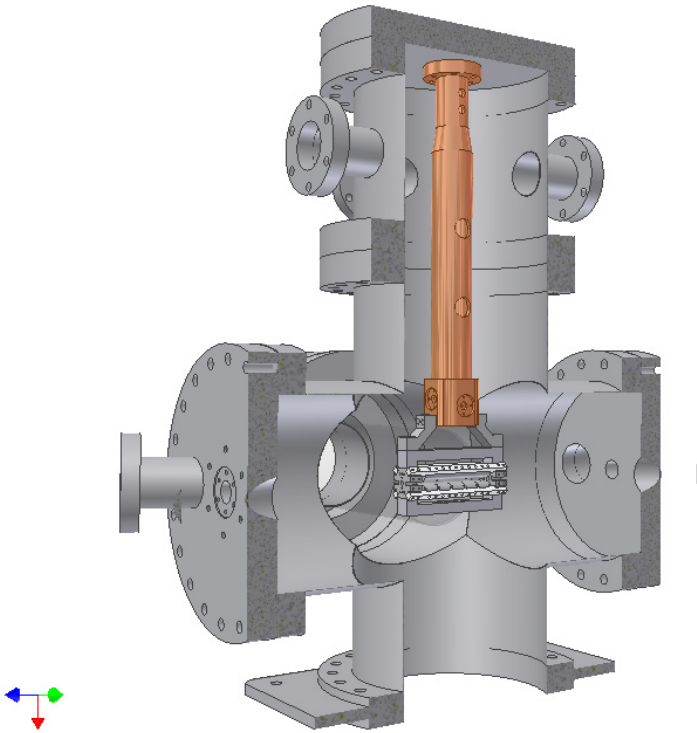


Figure 2.7: Computer-assisted-design (CAD) drawing of a cross section of the vacuum housing, including the ion trap and support structure (center), and one of the re-entrant viewports (translucent tube protruding from the back towards the trap). This drawing was made in INVENTOR.

vacuum chamber at 200 °C, a room-temperature pressure of $\sim 1 \times 10^{-10}$ mbar is obtained, as found from an Bayard-Alpert type ion gauge (Granville-Phillips 274).

2.5 Loading ions

In order to load ions in the trap, HD molecules from an HD gas bottle, and beryllium atoms evaporated from a beryllium oven (see below), are ionized through electron impact ionization. The ionizing electrons are delivered by a negatively biased electron gun (e-gun) which is a thoriated tungsten filament situated near the ion trap (see Fig. 2.4). The basic principle of operation is as follows. The filament is heated by a bias current in order to produce a

significant amount of thermo-electrons. The negative bias voltage subsequently accelerates these electrons away from the filament, and during certain phases of each trap rf cycle some electrons will traverse the center of the trap, where they may collide with neutral Be or HD particles. In total, three e-guns are installed, but during the experiment only one (left one in Fig. 2.4) is used. The maximum electron impact ionization cross sections for Be^+ and HD^+ are near 50 eV and 120 eV of electron energy, respectively [91]. The energies at which electrons arrive at a Be atom or HD molecule depends on the difference between the e-gun bias voltage and the instantaneous rf potential at the time of impact. Optimal e-gun bias voltages for loading Be^+ and HD^+ turn out to be -40 V and -200 V, respectively. In order to load ions, approximately 1 A of filament current is sent through the e-gun, which results in an emission electron current of ~ 20 μA . The emission current is exponentially dependent on the filament temperature, and therefore, in order to load ions in a reproducible manner, the emission current is stabilized with a servo loop system. The circuit diagram of this servo loop is depicted in Fig. 2.8. One salient feature of this setup is that it operates in galvanically separated domains, namely that of the ± 15 V control electronics, and the part which controls the filament current which is biased at -40 to -200 V. This is achieved by use of an opto-coupler which connects the e-gun part with the servo circuitry, thus preventing a high voltage at the servo system part.

2.5.1 Beryllium oven

The beryllium oven design was originally developed at the National Institute of Standards and Technology by P.O. Schmidt and T. Rosenband. The oven consists of a four-bore Al_2O_3 tube, of about 5 mm length and 1.2 mm outer diameter. Each bore has an inner diameter of 0.25 mm. A tantalum wire with 0.25 mm diameter is looped through three of the bores, while the remaining bore is filled with a 0.25-mm-diameter beryllium wire of a few millimeter length. To fix the beryllium wire, one end of the ceramic tube is filled with ceramic paste (Aremco Ceramabond 569-VFG), and subsequently cured for two hours at 90 $^\circ\text{C}$ in an oven.

By sending a current through the tantalum wire, the oven is heated. In order to achieve a sufficiently high beryllium vapor density, the oven should be heated to about 1300 to 1400 K. For an oven at such temperatures mounted in free space, a considerable amount of heat is lost by radiation, and the current through the tantalum filament needed to balance the radiation loss might break the filament. To reduce the burden on the filament, the oven is suspended in a 2.5-mm-wide cylindrical hole inside an aluminum part, such that a part of the radiation is reflected back onto the oven instead of being radiated away, and the current can be reduced to a more tolerable level. Heating the tantalum

2. EXPERIMENTAL SETUP

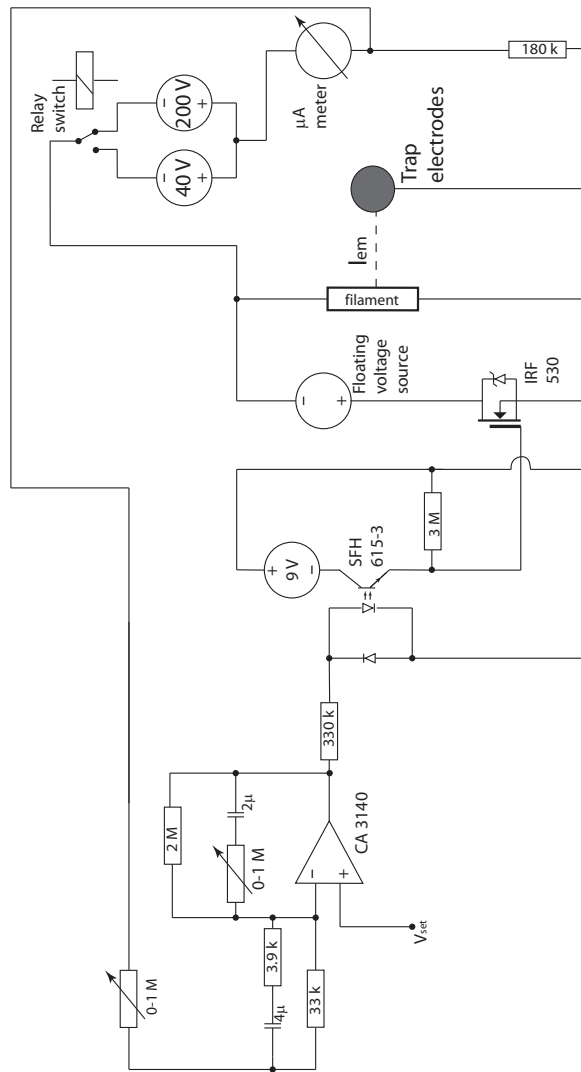


Figure 2.8: The emission current stabilization scheme of the electron gun. The emission current is converted to a voltage at the 180 kΩ resistor placed at the input of the μA meter. This voltage serves as input for the servo electronics, which controls the emission current by adjusting the filament current through a MOSFET (IRF 5320). An opto-coupler (SFH 615 – 3) separates the high voltage (–40 V or –200 V, adjustable by a relay switch) from the servo loop circuitry (left side).

wire with ~ 3 A is sufficient to evaporate a sufficiently large number of beryllium atoms, of which a small part will be ionized and trapped. The oven is covered with an aluminum cone that shields the rest of the vacuum chamber from excessive contamination by a (conductive) layer of beryllium. Evaporated beryllium atoms only escape through the small hole on top of the cone.

2.6 The UV laser-cooling system

In order to reduce the Doppler broadening of the $(v,L):(0,2)\rightarrow(8,3)$ transition linewidth, the HD^+ molecules need to be cooled to the millikelvin range. Since HD^+ cannot be cooled with a laser, Doppler-cooled Be^+ ions are used for sympathetically cooling of the HD^+ molecules. For Doppler cooling of Be^+ , a 313 nm laser is used which is essentially is a frequency-doubled 626 nm continuous-wave (cw) ring dye (sulforhodamine B) laser. This laser is pumped by 8 W of cw 532 nm light from a Nd:YVO₄ (Spectra-Physics Millennia X) laser. The frequency doubling is carried out by directing the 626 nm laser through a Brewster-cut β -barium borate (BBO) crystal housed in a bow-tie shaped enhancement cavity. The latter is kept resonant with the 626 nm laser frequency using a Hänsch-Couillaud locking scheme [92]. About 0.6 W is generated from the dye laser which, after a beam splitter for laser stabilization optics and transmission through an optical fiber, is converted to at most 10 mW of 313 nm. After the doubling cavity, cylindrical and spherical lenses are used to realize a beam waist of the 313 nm beam at the location of the ions of ~ 150 μm .

Selection rules provide a possibility to Doppler cool Be^+ without the use of any repumping lasers. The level scheme of the cooling transition is shown in Fig. 2.9. By using circularly polarized light directed along the quantization axis, σ^- and σ^+ transitions will ensue between the $^2\text{S}_{1/2}(F=2)$ and $^2\text{P}_{3/2}$ levels in Be^+ , which have a corresponding linewidth of $\Gamma = 2\pi \times 19.4$ MHz. This is an almost closed cooling transition which is sufficient to cool trapped Be^+ ions down to a few millikelvin. In order to generate circularly polarized light of high purity, the 313 nm beam is directed through a Glan-Taylor polarizer and a zero order quarter wave plate. Furthermore, to achieve a closed cycling transition, it is essential to align the quantization axis with the propagation direction of the light. For this reason, three orthogonal pairs of Helmholtz coils are installed around the vacuum system, generating a small B-field (1.9 G) which can be precisely aligned along the direction of propagation of the cooling laser. The 313 nm fluorescence is detected with a photomultiplier tube (PMT) and an electron-multiplied charge-coupled-device (EMCCD) camera at an angle of 90 degrees with respect to the trap axis (see Fig. 4.3).

The frequency of the 626 nm laser is locked to a fringe of a Fabry-Perot cavity which is locked to a HeNe laser with a maximum frequency drift of

2. EXPERIMENTAL SETUP

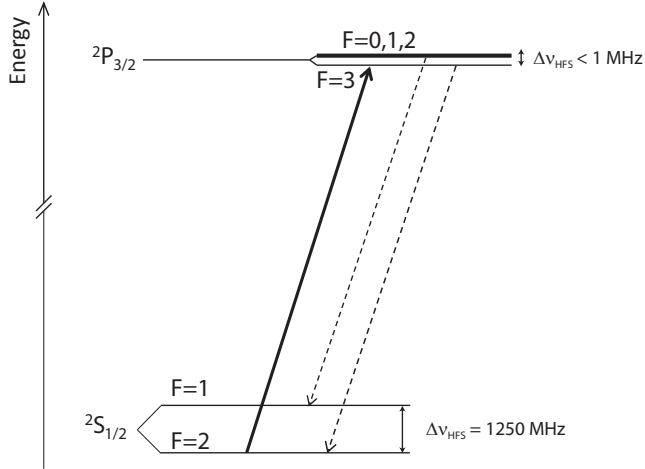


Figure 2.9: A diagram of relevant lines of the 313 nm laser cooling transition in Be^+ . The thick arrow represents the σ^\pm cooling transitions. The dashed arrows represent the dominant spontaneous channels from $F=0,1,2,3$ states. Non-perfect circularly polarized 313 nm light may lead to π transitions which lead to a small population of the ${}^2\text{S}_{1/2}(F=1)$ dark state.

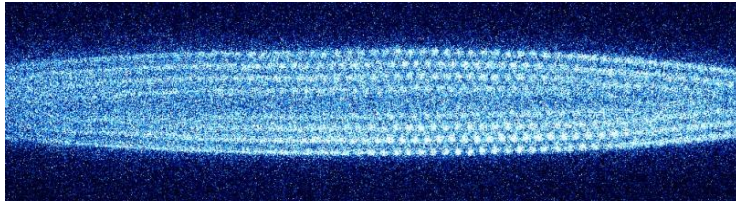


Figure 2.10: EMCCD camera image of a large Coulomb crystal with a height of approximately $100\ \mu\text{m}$. In the center of the Be^+ ion crystal a dark core is situated consisting of HD^+ , H_2D^+ and HD_2^+ . This crystal has temperature of $\sim 6\ \text{mK}$.

1 MHz per day. An AOM is placed within the optical path that is part of the servo loop of the Fabry-Perot cavity and the 626 nm laser. As discussed in detail in Chapter 3, this system offers the possibility to tune the 626 nm light over a frequency range of 30 GHz with a speed of 500 MHz/s without losing the frequency lock. Further details about this system are described in [75] and [93].

2.7 Spectroscopy laser setup

In order to probe the $(v,L):(0,2)\rightarrow(8,3)$ transition, a continuous-wave titanium:sapphire laser at 782 nm is used. This laser is pumped by 6 W of a 532 nm Nd:YVO₄ (Spectra-Physics Millennia V) laser. We use a self-referenced frequency comb in order to stabilize the frequency of the 782 nm light. The frequency comb itself is locked to a rubidium atomic clock for short-term stability. For long-term traceability to the SI second, the rubidium clock is disciplined to the pulse-per-second output of a GPS receiver, located on the roof of the building. The 782 nm light is transferred to the frequency comb (which is located in another laboratory) through a polarization-maintaining (pm) optical fiber. There, the 782 nm laser is mixed with the output of the optical frequency comb to produce a beat note at 63.5 MHz, which is amplified and counted by a frequency counter (Agilent 53132A). The beat note signal from the counter is sent back to the 782 nm laser laboratory and used to generate an error signal as input for a digital servo loop. A schematic overview of the setup is shown in Fig. 2.11. More details of this system are given in Chapter 4.

2.8 Computer control system

The software for control of the setup is written in Python and provides a high level of automation. By using the TkInter graphical user interface (GUI) in combination with a touch screen, complex and parallel experimental routines can be started with a single tap at the screen, such as the secular scan-REMPD-secular scan measurement scheme shown in Fig. 4.5. The computer interfaces physically with the experimental setup through a National Instruments (NI) GPIB and PCI6023 card (analog or TTL outputs). For data acquisition (DAQ) the PCI6023 card and two NI USB6009 DAQ devices are used. To communicate at the level of native NI software (NI-DAQmx), the Python software uses a wrapper based on the ctypes library and a C-library of DAQmx commands. A similar approach is followed for the communication between the Python software and the EMCCD camera (Andor iXon DU885-KCS-VP).

2. EXPERIMENTAL SETUP

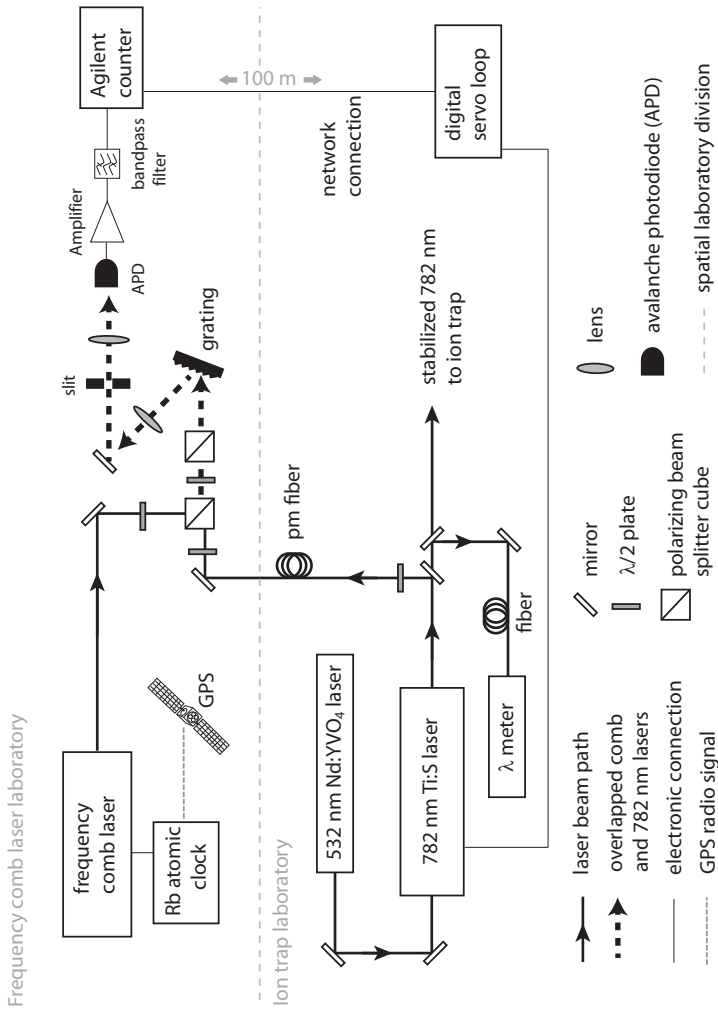


Figure 2.11: A schematic view of the Ti:S laser and the setup for frequency locking. The 782 nm Ti:S laser is pumped by 532 nm light and is directed to a wavemeter, the ion trap and to the frequency comb laboratory. The combination of the grating, lens and slit serves as a spectral filter which reduces the intensity on the avalanche photodiode (APD) by transmitting only the comb modes close to 782 nm. The beat note (63.5 MHz) of the overlapping 782 nm and frequency comb beams is detected with an APD and amplified. An electronic bandpass filter cuts off frequencies that differ by more than 5 MHz from the beat-note frequency. The beat note is counted, and the result is sent back to the ion trap laboratory and used by a digital servo loop in order to lock the 782 nm laser cavity.

Widely tunable laser frequency offset lock

We demonstrate a simple and versatile method to greatly extend the tuning range of optical frequency shifting devices, such as acousto-optic modulators (AOMs). We use this method to stabilize the frequency of a tunable narrow-band continuous-wave (CW) laser to a transmission maximum of an external Fabry-Perot interferometer (FPI) with a tunable frequency offset. This is achieved through a servo loop which contains an in-loop AOM for simple radiofrequency (RF) tuning of the optical frequency over the full 30 GHz mode-hop-free tuning range of the CW laser. By stabilizing the length of the FPI to a stabilized helium-neon (HeNe) laser (at 5 THz offset from the tunable laser) we simultaneously transfer the ~ 1 MHz absolute frequency stability of the HeNe laser to the entire 30 GHz range of the tunable laser. Thus, our method allows simple, wide-range, fast and reproducible optical frequency tuning and absolute optical frequency measurements through RF electronics, which is here demonstrated by repeatedly recording a 27-GHz-wide molecular iodine spectrum at scan rates up to 500 MHz/s. As a further example, we illustrate the use of the method for laser-cooling experiments on trapped ions. General technical aspects that determine the performance of the method are discussed in detail.

3.1 Introduction

Narrowband continuous-wave (CW) stabilized lasers have many applications in experimental atomic and molecular physics, examples including laser spectroscopy, laser cooling, and coherent optical manipulation of atoms and molecules. Such experiments often require wide optical frequency tunability, as well as precise control of the absolute optical frequency. A commonly-used method is to lock a laser source directly to a nearby optical or molecular reference transition, after which part of the laser output is sent through a variable-frequency-shifting device such as an acousto-optic modulator (AOM) or an electro-optic modulator (EOM). Both AOMs and EOMs have the practical advantage that optical frequency tuning is readily accomplished by adjusting the radio frequency (RF) of the device driver electronics. The frequency shift of AOMs is restricted to typically 1 GHz by the limited phase velocity of the acoustic wave in the acousto-optic crystal, while the tuning range is limited to a fraction of the shift (typically 50–100 MHz). In addition, the diffraction efficiency of AOMs tends to decrease with increasing RF frequency. Frequency shifting over larger ranges while maintaining high efficiencies is possible using EOMs. For example, employing serrodyne phase modulation, continuous tuning over 1.5 GHz of a stabilized optical frequency was achieved with an efficiency of over 80% [94,95]. Frequency shifting over ± 32.5 GHz with an efficiency of 60% was achieved with a technique based on cascaded electro-optical traveling phase gratings in a traveling wave EOM [96]. An alternative method is to offset lock a slave laser to a master laser by detecting their beat note with a fast photodiode and stabilizing the beat-note frequency to the output of a microwave synthesizer [97,98]. This method is limited by the detection bandwidth of the photodiode, which may reach up to 100 GHz. A practical disadvantage of the latter two methods is the need for spectrally pure, high-end microwave oscillators.

For optical frequency offset locking and tuning at larger detunings, so-called transfer cavities are often used [99]. Here the length of a Fabry-Pérot interferometer (FPI) is stabilized to the wavelength of a first laser, which is locked to an atomic or molecular reference transition. A second ‘spectroscopy’ laser is subsequently locked to one of the transmission maxima of the cavity, thereby allowing for frequency offsets in the many-THz range. However, the continuous tuning range remains limited by the AOM or EOM needed for frequency shifting from the reference cavity mode. A similar method employs an optical frequency comb laser [100]: here, the spectroscopy laser is locked to a nearby mode of the comb spectrum, for instance by stabilizing the optical beat-note frequency to a tunable RF reference frequency.

Tunable lasers with known frequencies are also of interest to laser spectroscopy. Here, frequency calibration is often achieved by use of an FPI locked

to an atomic or molecular reference frequency, where the free spectral range (FSR) of the FPI is calibrated against two well-known atomic or molecular reference lines [101]. Thus, as the spectroscopy laser is scanned over the spectrum of interest the FPI transmission maxima provide a relative frequency scale. This approach is limited by nonlinear scanning of the spectroscopy laser and interpolation errors in between the FPI transmission maxima.

In this paper, we present a simple and generally applicable RF method to tune optical frequencies over frequency ranges in excess of 25 GHz, and at frequency offsets of several THz from an atomic or molecular reference line. The method combines a transfer cavity, locked to a frequency-stabilized helium-neon (HeNe) laser, with an AOM that is placed inside the servo loop that locks the spectroscopy laser to the transfer cavity. With this method we demonstrate tuning at 500 MHz/s of a narrowband CW laser over its mode-hop-free tuning range of ~ 30 GHz while maintaining reference to the HeNe laser. Furthermore, the absolute optical frequency of the laser can be set with a reproducibility of 1 MHz anywhere in its 30-GHz tuning range. Our method also circumvents nonlinear scanning issues and the need for interpolation in between transmission maxima for laser spectroscopy. To verify the frequency reproducibility and to illustrate the general applicability of the method, we demonstrate spectroscopy of a 27-GHz-wide portion of the spectrum of molecular iodine (I_2), and we discuss how the CW laser is used (after frequency doubling) in an experiment to laser cool trapped beryllium (Be^+) ions at various detunings from the 313 nm resonance line.

3.2 Experimental setup and principle of operation

Figure 3.1 depicts our experimental setup. A central role is played by the FPI which here acts as a transfer cavity. The FPI has a length of 0.5 m and is stabilized to the wavelength of a CW 632.8 nm helium-neon laser as follows. The output of the HeNe laser is coupled into the FPI, and the transmitted power is detected by a first photodiode (PD1). One of the FPI mirrors is mounted onto a piezo-ceramic actuator (PZT), driven by a sinusoidal voltage with frequency $f_M = 735$ Hz. The resulting cavity-length modulation dithers the transmitted power at PD1, which is converted into an error signal using a lock-in amplifier. The error signal is fed into a servo loop with PI characteristic which provides feedback to the PZT to control the FPI length for maximum HeNe transmission. In this way, the 1 MHz long-term frequency accuracy of the HeNe laser is transferred to the length of the FPI. All experiments described below were conducted with the HeNe servo loop closed.

In our setup, the FPI serves to stabilize the wavelength of a second CW laser, which is a commercial ring dye laser running on sulforhodamine B near

3. WIDELY TUNABLE LASER FREQUENCY OFFSET LOCK

626 nm. This laser is used for various purposes, as discussed in more detail in Sec. 3.3. The dye laser frequency is locked to the FPI as follows. A small portion (0.5%) of the dye laser output is picked off and sent through an AOM. Operating the AOM in double-pass configuration [102] allows shifting the optical frequency by an amount $\Delta_{\text{AOM}} = 500 \pm 100$ MHz, without significantly affecting the propagation direction of the doubly-diffracted output beam. The AOM is driven by a voltage-controlled oscillator (VCO), whose output is amplified to 1.5 W. The double-pass diffraction efficiency of the AOM varies between 0.2 and 0.7 over the entire tuning range. The doubly-diffracted beam is subsequently overlapped with the HeNe laser beam using a polarizing beamsplitter cube (PBC), and coupled into the FPI. Care is taken to excite only the TEM₀₀ transverse mode of the FPI. After the transmission, the dye laser light is separated from the HeNe light by a second PBC, and detected by a second photodiode (PD2). Due to the modulation of the FPI length through the PZT, the transmission signal at PD2 is modulated at frequency f_M as well. This signal is fed into a second lock-in amplifier which delivers an error signal to a second PI servo loop. The latter provides feedback to the external scan input of the dye laser's control electronics. Thus, the wavelength of the output of the double-pass AOM is locked to the length of the FPI.

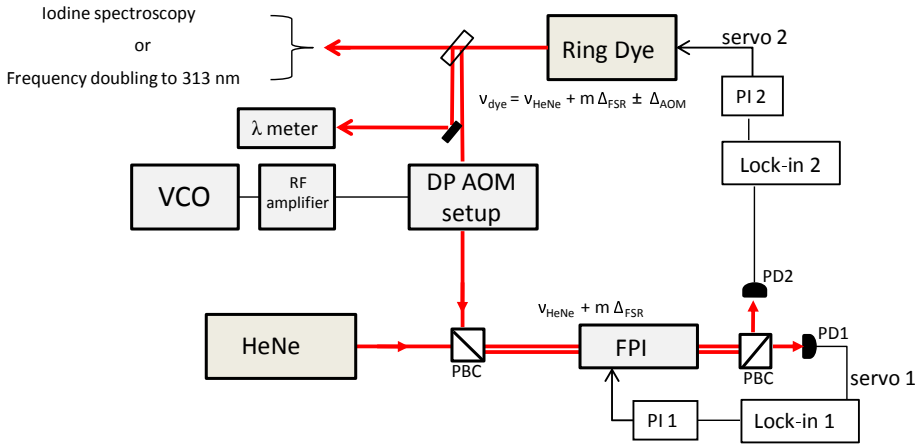


Figure 3.1: Experimental setup scheme. Red lines indicate optical beam paths, whereas electrical connections are colored black. VCO, Voltage Controlled Oscillator; DP AOM, double-pass AOM setup; PI, proportional-integral loop filter; lock-in, lock-in amplifier; PD, photodiode; PBC, polarizing beamsplitter cube; λ meter, optical wavelength meter. The overlapped laser beams traveling through the FPI are offset here for clarity.

The in-loop AOM may be used to tune the frequency of the dye laser over

3.2. Experimental setup and principle of operation

an arbitrary range with respect to the HeNe laser frequency as follows. First, we note that the output frequency of the dye laser, ν_{dye} , and the frequency of HeNe laser, ν_{HeNe} , are related via

$$\nu_{\text{dye}} = \nu_{\text{HeNe}} + m\Delta_{\text{FSR}} \pm \Delta_{\text{AOM}}, \quad (3.1)$$

where m is an integer which corresponds to the number of FPI modes separating ν_{dye} from ν_{HeNe} , and $\Delta_{\text{FSR}} \simeq 149$ MHz stands for the FSR. The absolute values of ν_{HeNe} and m do not have to be known in order to operate the system and use this method. As will become clear below, it is essential that the 200 MHz tuning range of the double-pass AOM setup exceeds the FSR of the FPI.

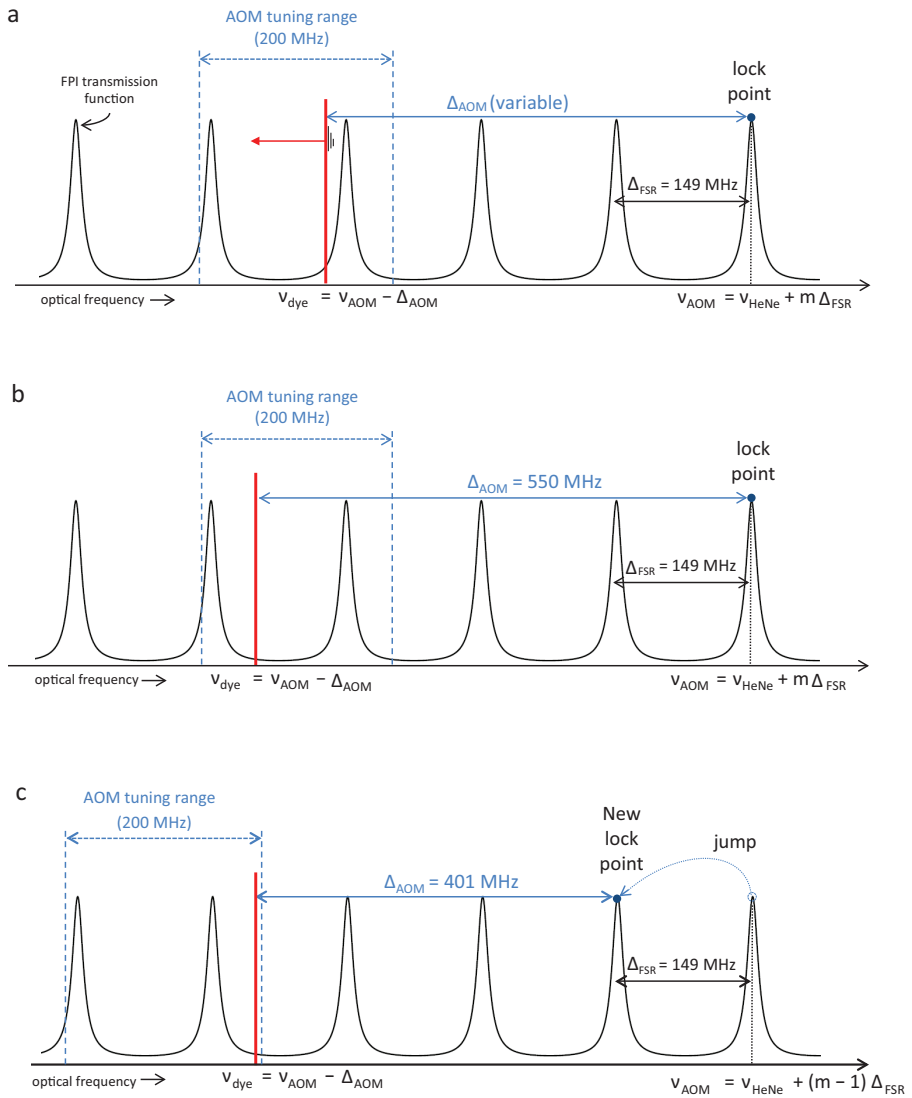
If the AOM frequency is tuned slowly (*i.e.* much slower than the control bandwidth of the dye laser servo loop), the servo loop will act so as to maintain the condition expressed by Eq. (3.1). This allows tuning ν_{dye} by 200 MHz with respect to the fixed mode frequencies of the FPI, as depicted schematically in Fig. 3.2(a). By contrast, if the AOM frequency is tuned rapidly (*i.e.* much faster than the response time of the dye laser servo loop) by exactly one FSR of the FPI, this sudden ‘jump’ in AOM frequency will not be detected by the servo loop, and the dye laser frequency will not be affected. In effect, the lock will be re-established at the next mode of the FPI so that the frequency of the dye laser can now be written

$$\nu'_{\text{dye}} = \nu_{\text{HeNe}} + (m \pm 1)\Delta_{\text{FSR}} \pm \Delta'_{\text{AOM}}, \quad (3.2)$$

where $\Delta'_{\text{AOM}} = \Delta_{\text{AOM}} - \Delta_{\text{FSR}}$ (see Figs. 3.2(b) and (c)).

From the new lock point, the dye laser can again be tuned by slowly adjusting the AOM frequency, but this time within one FSR adjacent to the original tuning range (see Fig. 3.2 (d)). Throughout the following we will refer to the fast AOM frequency adjustments as ‘jumps’, and to the slow AOM-frequency tuning as ‘scanning’. In practice, the bandwidth of the dye laser servo loop allows scanning at rates up to 500 MHz/s, while frequency jumps are made at rates in excess of 10 THz/s. In principle, the process of scanning and jumping can be repeated indefinitely, thus allowing large frequency ranges to be covered. Furthermore, this widely-tunable offset lock method works for frequency scans in either direction (*i.e.* toward higher or lower optical frequencies). An analogy can be drawn between this method and the dragging of a computer mouse over a mousepad: after dragging the mouse from the bottom to the top edge of the mousepad (scanning), the mouse can be lifted and placed back at the bottom edge (jump) to enable a next drag across the mousepad. In this way a mouse pointer on a computer screen can be dragged over arbitrary long

3. WIDELY TUNABLE LASER FREQUENCY OFFSET LOCK



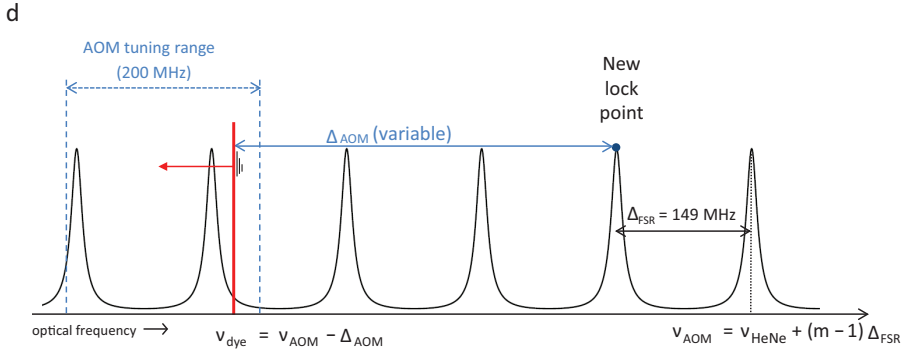


Figure 3.2: Illustration of the ‘AOM-jump method’: (a) the dye laser is scanned in a controlled way by RF tuning of the AOM within the AOM tuning range; (b) near the edge of the AOM tuning range the scan is stopped; (c) subsequently the AOM frequency is rapidly adjusted so that Δ_{AOM} jumps by Δ_{FSR} without perturbing the frequency of the dye laser; (d) the dye laser is ready to be scanned by one FSR adjacent to the previous scan range.

distances while using a space no larger than the dimensions of the mousepad. In the present case of laser frequency tuning, the process can be repeated not only indefinitely but also reproducibly as long as the servo loop remains closed. In practice, the tuning range is limited by any process that will break the servo loop, such as mode-hops of the laser that is being tuned, or the servo loop output voltage hitting the rail voltage of the electronics. Also, the method will cease to work for wavelengths for which the FPI finesse is reduced (due to loss of mirror reflectivity) so that a reliable error signal for locking cannot be obtained. However, all the above limitations are technical and not inherent to the method itself.

The frequency shift applied to the AOM during a jump should be close to Δ_{FSR} , but does not necessarily have to equal this value: the servo loop will compensate for any small frequency mismatch within the linewidth of the FPI after the jump during the scan phase. As a result, a wide-range frequency scan through N successive jumps and scans will cover a frequency range of exactly $N\Delta_{\text{FSR}}$, apart from additional frequency adjustments made before the first jump and after the last jump of the scan.

Even if the exact values of ν_{HeNe} and m from (3.1) and (3.2) are unknown, absolute frequency measurements can be done if the dye laser is calibrated against a well-known optical frequency. In this way (and as shown in 3.3.2

below) optical spectroscopy can be accomplished within the 30 GHz mode-hop-free tuning range of the dye laser with an accuracy dependent on the accuracies of Δ_{FSR} , Δ_{AOM} , the frequency calibration, and the stability of ν_{HeNe} .

3.3 Results and discussion

3.3.1 Frequency calibration

With the wide-tunable offset lock presented here, we are able to tune the dye laser over a range of 30 GHz (the maximum scan range admitted by the dye laser control electronics) with a speed of ~ 500 MHz/s through simple RF tuning. During such wide-range scans, the frequency detuning from the initial frequency can be inferred by summing two parameters, namely the instantaneous VCO frequency, and the number of FSRs jumped over. This necessitates calibration of the voltage-frequency relationship of our VCO, as well as the FSR of the FPI. To calibrate the VCO, the VCO output is first mixed with the output of a stable RF signal generator of known frequency, after which the low-passed mixer output is fed into a frequency counter. The calibration accuracy is 10 kHz limited by long-term drifts of the VCO.

In order to make a jump of one FSR one has to know the approximate value of the FSR. In case the FSR of the FPI is unknown a coarse value can be easily obtained by making a series of jumps within a frequency range that encompasses the FSR. By monitoring the change in transmission at each jump using PD2 (Fig. 3.1), the line shape of the FPI transmission maximum can be traced out. In our case a series of 69 jumps (each starting from the same initial frequency which in this case corresponds to a transmission maximum of the FPI) in the range of -21 MHz to $+166$ MHz revealed the FPI transmission function from which a value of the FSR is extracted with better than one percent accuracy.

We also point out that instead of using a length-stabilized FPI, one might use a self-referenced optical frequency comb laser which is locked to some optical atomic or molecular reference frequency by stabilizing the repetition rate of the frequency comb [100]. In this case, the fixed frequency comb spectrum can replace the FPI in our method. For example, the servo loop of our method may stabilize the beat-note frequency between the double-pass AOM output beam and the nearest mode of the frequency comb. Again, fast AOM jumps by exactly one repetition rate of frequency comb would not influence the servo loop that controls the CW laser frequency.

3.3.2 Fast linear scanning and frequency reproducibility: demonstration through I₂ spectroscopy

As a first demonstration, we employ our widely-tunable offset lock to record a 27-GHz-wide portion of the absorption spectrum of I₂. To this end, the dye laser output is directed to an existing setup for saturated absorption spectroscopy in an I₂ vapor cell [103]. As the I₂ spectrum has been well calibrated [104, 105], it can also serve to independently determine the FSR of the FPI, and to assess the overall performance of our method. To demonstrate the wide tuning range and reproducibility offered by the widely-tunable offset lock, we acquire six copies of the 27-GHz-wide iodine absorption spectrum by alternately scanning the dye laser upward and downward across the spectrum. The servo loop remained closed throughout all scans, which were taken in the course of 1.5 hours. The absorption signal and the output voltage sent to the VCO are simultaneously recorded by two analog voltage input channels of the PC that also controls the experiment. To achieve a linear frequency scan over time, a nonlinear voltage ramp is applied to the VCO which precompensates the nonlinearity of the VCO. The horizontal axis is converted from voltage to frequency by counting the number of jumps (each of which corresponds to one FSR), and using the VCO calibration to find the frequency between the jumps (Sec. 3.3.1). Each spectrum in Fig. 3.3 is taken at two different scan rates: the two regions containing strong absorption features (separated by about 20 GHz) are taken at 25 MHz/s to achieve a good signal-to-noise ratio, whereas the intermediate 20 GHz span is covered at a higher rate of 300 MHz/s to speed up the data acquisition. Figure 3.3 only shows the parts of the spectra taken at 25 MHz/s. The I₂ spectra in Fig. 3.3 are ordered chronologically with the final spectrum on top.

We have compared the frequencies of the various absorption features in Fig. 3.3 with their known values from literature [104, 106] to infer an independent value for the FSR of our FPI. For example, the frequency difference between the features indicated by the thick dashed lines in Fig. 3.3 is 24908.7(1) MHz [106]. We find that this corresponds to 167.18(2) times the FSR, which yields $\Delta_{\text{FSR}} = 148.99(2)$ MHz.

In order to obtain absolute optical frequencies we calibrated the dye laser frequency with respect to the a₁ hyperfine component of the I₂ P60(7,3) transition ($\nu_{\text{I}_2} = 476.300358(3)$ THz [106]), indicated by the thick dashed line at 0 GHz in Fig. 3.3. Within the entire frequency tuning range of 30 GHz with respect to the optical frequency standard the absolute frequency accuracy is better than 6 MHz.

The spectra taken at 25 MHz/s in opposite scan directions reveal a frequency lag of 6(1) MHz of the dye laser frequency with respect to the frequency as determined from the VCO control voltage. The lag is clearly visible

3. WIDELY TUNABLE LASER FREQUENCY OFFSET LOCK

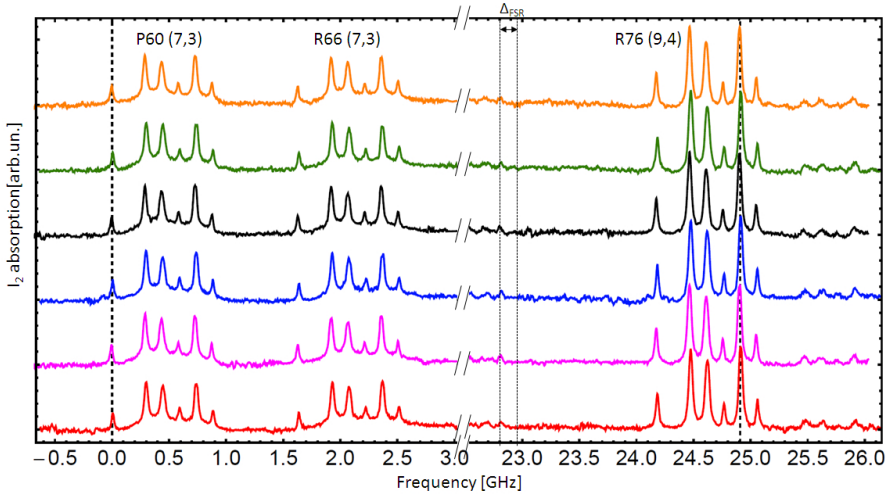


Figure 3.3: Six traces of part of the I_2 spectrum recorded using the widely-tunable offset lock. The curves were alternately taken in upward and downward scan directions, starting from -0.65 GHz upward (bottom spectrum was taken first). The frequency difference between the absorption features indicated by the thick dashed lines is 24908.7 MHz. The left thick dashed line at zero frequency corresponds to 476.300358(3) THz.

in Fig. 3.4, and stems from the limited response time of the electronics. A Laplace-transform analysis of the servo-loop electronics predicts a contribution to this lag of 0.1 MHz, while a similar analysis of the I_2 spectroscopy electronics reveals a 7 MHz lag caused by the low-pass-filter time constant chosen to record spectra with good signal-to-noise-ratio. The 7.1 MHz total lag is in agreement with the observed lag. Note that this frequency lag is not inherent to the method, apart from the small 0.1 MHz lag which may be reduced by an increased servo loop bandwidth or a reduced scan speed.

Apart from the frequency lag, Fig. 3.4 confirms that our widely-tunable offset lock can reliably and reproducibly set the dye laser frequency with a precision of 1 MHz. In principle, this precision may be further improved by using a more stable optical reference frequency to stabilize the FPI, and by using an FPI with a larger finesse so that a tighter frequency lock of the dye laser is achieved. Laser frequency stabilization to FPIs at the 1 Hz level is nowadays routinely achieved, while optical frequency standards have achieved sub-Hz accuracy [4]. A tighter lock may also increase the maximum scan rate: given the 10–15 μ s response time of our VCO, we could in principle improve the response time of our servo loop by a factor of 1000 to a few 100 μ s, while

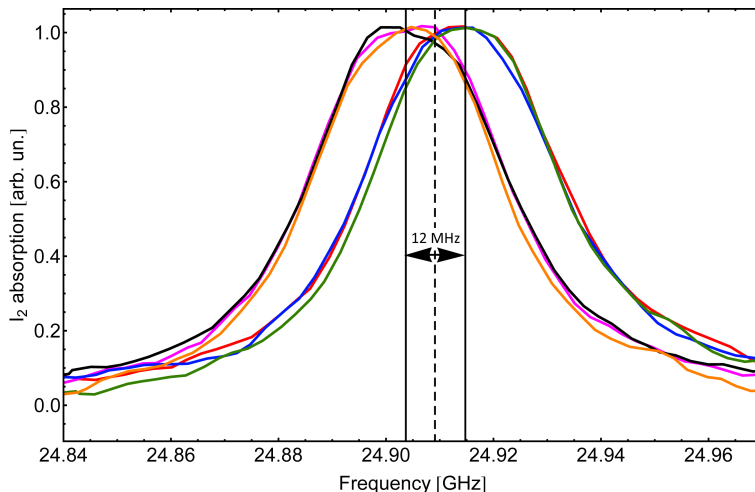


Figure 3.4: Zoom-in of the spectra of Fig. 3.3 between 24.84 and 24.97 GHz. The scans taken in forward direction and in backward direction display a relative displacement of about 12 MHz, caused predominantly by the finite response time of the I_2 signal detection electronics.

still keeping the AOM jumps invisible to the servo loop. It therefore appears feasible to increase the maximum scan rate from 0.5 GHz/s to 0.5 THz/s.

3.3.3 Reproducible frequency tuning: application to a beryllium laser cooling experiment

We have used our widely-tunable offset lock for laser cooling and detection of trapped Be^+ ions, and spectroscopy of sympathetically cooled HD^+ molecular ions [93]. Laser cooling of Be^+ is accomplished by driving the $^2\text{S}_{1/2}(\text{F} = 2) \rightarrow ^2\text{P}_{3/2}(\text{F} = 3)$ first resonance line at 313 nm, at an appropriate fixed red detuning from the cooling resonance. The 313 nm radiation is obtained by second-harmonic generation (SHG) of 626 nm radiation, produced by our dye laser, in an external optical resonator containing a nonlinear crystal. Fluorescence photons emitted by the Be^+ ions are collected and imaged onto an electron-multiplied charge-coupled-device (EMCCD) camera. These photons are also used for indirect detection of vibrational resonances in HD^+ [93], which furthermore requires that the 313 nm laser frequency be scanned once every minute between two values separated by 1 GHz, with an absolute frequency accuracy of a few MHz, and for periods of time exceeding one hour. Moreover, to achieve high power levels at 313 nm it is preferable that the full output

power of the 626 nm dye laser be available for SHG. These requirements are difficult to meet using standard AOMs or EOMs due to their finite modulation bandwidth and efficiency. Our widely-tunable offset lock provides the required tunability, absolute accuracy, and optical power. These features are also of particular interest for coherent optical manipulation experiments which require high-intensity laser beams at large (10 – 200 GHz) detuning from resonance lines in atoms [107] and ions [108].

3.4 Conclusion

We have demonstrated a simple RF method to continuously scan the frequency of a narrowband CW dye laser within its 30 GHz mode-hop-free tuning range, with a controlled offset from an optical reference frequency at 5 THz. The method employs an AOM placed inside the servo loop that locks the dye laser to a length-stabilized FPI, and allows automated RF scanning and relocking to adjacent FPI modes without breaking the servo loop. Frequency stability and reproducibility of better than 1 MHz within the entire 30-GHz tuning range and over time scales longer than one hour were demonstrated, and linear scanning at rates up to 500 MHz/s achieved. Moreover, calibration of the dye laser frequency using a well-known optical transition leads to an absolute optical frequency accuracy of better than 6 MHz. We expect that considerably higher accuracy and faster scan rates can be achieved using high-finesse FPIs and high-bandwidth control loops.

We have addressed various technical aspects that determine the performance of our method. The stability and reproducibility of our widely tunable offset lock have been verified through spectroscopy of a known portion of the spectrum of I_2 , and we have illustrated the usefulness of the method for laser cooling and detection of Be^+ ions. The method is generally applicable to other types of single-frequency CW lasers in other wavelength ranges, which makes it potentially useful for other areas of research, requiring stable yet widely-tunable laser sources, including atom interferometry [107], and quantum information processing using trapped ions [108].

Acknowledgments

This work was supported through FOM Program 125 "Broken Mirrors and Drifting Constants". J.C.J.K. thanks the Netherlands Organisation for Scientific Research (NWO) for support. The work of K.T.S. was funded by the COST action MP1001 IOTA.

High-precision spectroscopy of the HD^+ molecule at the 1-p.p.b. level

We present a high precision frequency measurement of the vibrational overtone transition $(v,L):(0,2)\rightarrow(8,3)$ in the deuterated molecular hydrogen ion HD^+ . This measurement has a resolution of 0.85 parts-per-billion (p.p.b.) and is in agreement with molecular theory within 0.6(1.1) p.p.b. We here provide the details of the experimental procedures and spectral analysis. A model is devised to obtain a spectral lineshape function which is subsequently fitted to the recorded spectrum. This model, which is generally applicable to any form of Doppler-broadened, destructive spectroscopy of finite samples of trapped ions, is sensitive to the shape of the velocity distribution. In particular we find that deviations from a thermal (Gaussian) distribution, due to laser-induced chemistry, leads to a lineshift. We perform realistic molecular dynamics simulations to obtain an estimate of the relative frequency correction, which is found to be -0.6(6) p.p.b.

4.1 Introduction

Because of their relative simplicity, molecular hydrogen ions such as H₂⁺ and HD⁺ can be used as probes to test fundamental physics. Already four decades ago, Wing *et al.* [57] performed measurements of the ro-vibrational transitions in HD⁺ and proposed that such measurements could be used to test quantum electrodynamics (QED) theory in molecules, and improve on the existing value of the proton-to-electron mass ratio μ . With the assumption that the precision of theoretical calculations and measurements would increase in the upcoming years, precision tests of theory would increase in stringency.

Nowadays, values of ro-vibrational transition frequencies in H₂⁺ and HD⁺ have been calculated up to the order $m_e\alpha^8$, with m_e the electron mass, and α the fine-structure constant, leading to relative uncertainties at the level of 10^{-11} [1, 2]. The frequencies of these transitions are typically in the (near-)infrared with linewidths below 10 Hz, which makes them amenable to high-resolution laser spectroscopy. Optical clocks based on trapped ions have shown that laser spectroscopy at very high accuracy (below one part in 10^{17}) is possible [4]. Recent theoretical studies point out that for molecular hydrogen ions experimental uncertainties in the 10^{-16} range should be possible [14, 15]. High-precision measurements on molecular hydrogen ions can also be used to probe physics beyond the standard model, which could manifest itself in the form of hypothetical fifth forces between hadrons [69, 70] or gravitational effects from compactified higher dimensions [72]. If present, such effects might result in a discrepancy between molecular theory and experiment.

The most precise measurement of a ro-vibrational transition in HD⁺ so far resulted in a 2.4σ discrepancy with more accurate theoretical data [64]. The question whether this offset is a statistical outlier, or is caused by an experimental systematic effect or by possible new physics has remained unanswered. Therefore, additional experimental data on HD⁺ are needed. In this article we present a high-precision frequency measurement of the ro-vibrational transition $(v,L):(0,2)\rightarrow(8,3)$ in the HD⁺ molecule, and compare it with state-of-the-art molecular theory. From this comparison one can derive new constraints on possible new physics in HD⁺ and determine a value of μ for the first time from a molecular system [76].

This article is organized as follows. In Sec. 4.2 we briefly review the theory of HD⁺ relevant to this experiment. In Sec. 4.3 we describe a setup where HD⁺ is trapped in a Paul trap and sympathetically cooled with beryllium ions. A non-destructive detection scheme is presented which is used as a diagnostic tool for spectroscopy. The analysis of the data based on a line-shape fit model is described in Sec. 4.4. Here a significant effect of chemical processes in a Coulomb crystal is discussed for the first time.

4.2 Theory

4.2.1 Calculation of ro-vibrational frequency transitions in HD^+

The calculation of ro-vibrational energies in quantum mechanical three-body systems can be split into two main parts: the non-relativistic energies and the other contributions, *i.e.* relativistic and radiative energies and finite nuclear size effects. The non-relativistic part is calculated through solving the three-body Schrödinger equation, which can be done with practically infinite precision [44] (up to relative precision of $\sim 10^{-30}$ [48]). The resulting wavefunctions allow an analytical evaluation of the Breit-Pauli Hamiltonian and the leading-order radiative corrections.

The precision of relativistic and radiative energy corrections to the non-relativistic energies was recently strongly improved. With the inclusion of the full set of contributions of order $m\alpha^7$ and leading-order terms of order $m\alpha^8$, the relative uncertainty is now below 4×10^{-11} . For example, the theoretically determined value of the ro-vibrational $(v,L):(0,2) \rightarrow (8,3)$ transition frequency in HD^+ , ν_{th} , is 383,407,177.150(15) MHz, and has a relative uncertainty of 4×10^{-11} [1, 2]. Note that the specified error (within parentheses) does not include the uncertainty of the fundamental constants used. By far the largest contribution is due to the 4.1×10^{-10} uncertainty of μ (2010 CODATA table), which translates to a frequency uncertainty of 59 kHz.

4.2.2 Hyperfine structure and rotational states

Since the HD^+ constituents possess nonzero spin, the ro-vibrational transition spectra contain hyperfine structure due to spin-spin and spin-orbit couplings. In [109] the hyperfine energy levels and eigenstates in HD^+ are calculated by diagonalization of the effective spin Hamiltonian:

$$\begin{aligned}
 H_{\text{eff}} = & E_1(\mathbf{L} \cdot \mathbf{s}_e) + E_2(\mathbf{L} \cdot \mathbf{I}_p) + E_3(\mathbf{L} \cdot \mathbf{I}_d) + E_4(\mathbf{I}_p \cdot \mathbf{s}_e) \\
 & + E_5(\mathbf{I}_d \cdot \mathbf{s}_e) + E_6 K_d(\mathbf{L}, \mathbf{I}_p, \mathbf{s}_e) + E_7 K_d(\mathbf{L}, \mathbf{I}_d, \mathbf{s}_e) \\
 & + E_8 K_d(\mathbf{L}, \mathbf{I}_p, \mathbf{I}_d) + E_9 K_Q(\mathbf{L}, \mathbf{I}_d),
 \end{aligned} \tag{4.1}$$

where the spin coefficients, E_i , are obtained by averaging the Breit-Pauli Hamiltonian over the nonrelativistic wavefunctions, \mathbf{L} is the rotational angular momentum operator, and \mathbf{s}_e , \mathbf{I}_p and \mathbf{I}_d are the electron, proton and deuteron spin operators. K_d and K_Q are spherical tensors composed of angular momenta, whose explicit form is given in [109]. The strongest coupling is the proton-electron spin-spin interaction (the term in E_4 in Eq. (4.1)), which is the Fermi contact term on the proton, and the preferred angular momentum coupling

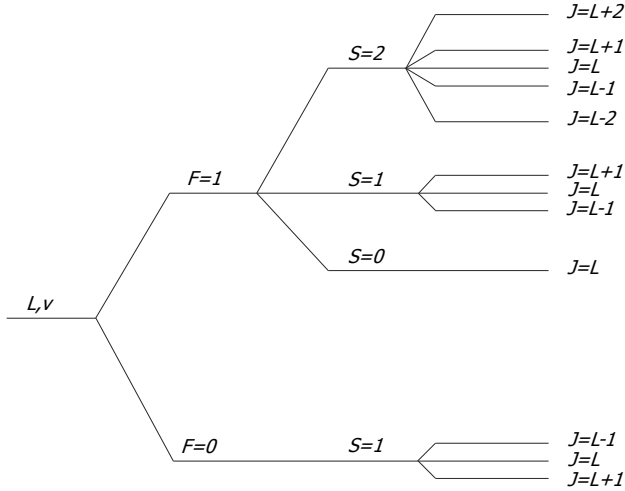


Figure 4.1: Schematic diagram of hyperfine states of the lower vibrational energy levels in HD⁺ with $L \geq 2$.

scheme is

$$\mathbf{F} = \mathbf{I}_p + \mathbf{s}_e \quad \mathbf{S} = \mathbf{F} + \mathbf{I}_d \quad \mathbf{J} = \mathbf{L} + \mathbf{S}. \quad (4.2)$$

This leads to hyperfine levels spread out over an energy range of ~ 1 GHz, as schematically depicted in Fig. 4.1. Diagonalization produces eigenstates $\phi_{\tilde{F}\tilde{S}JM_J}$, with the magnetic quantum number M_J corresponding to the projection of J onto the laboratory-fixed z -axis. Note that after diagonalization the quantum numbers ($\tilde{F}\tilde{S}$) are only approximately good (which is why they are labeled with a tilde), and a hyperfine eigenstate can be expressed in the ‘pure’ basis states $|FSJM_J\rangle$ as follows:

$$\phi_{\tilde{F}\tilde{S}JM_J} = \sum_{F,S} \beta_{FSJ} |FSJM_J\rangle, \quad (4.3)$$

with real-valued coefficients β_{FSJ} . In [109] the hyperfine levels in vibrationally excited states in HD⁺ are calculated with an uncertainty of ~ 50 kHz, but the uncertainty effects on the $(v,L):(0,2) \rightarrow (8,3)$ transition are much smaller due to a large common mode cancellation (see Sec. 4.4.6).

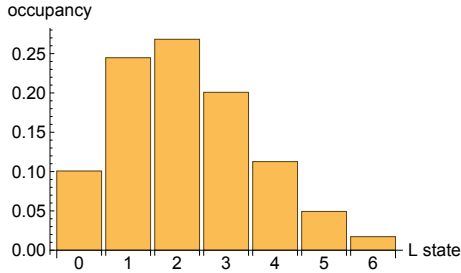


Figure 4.2: Bar chart of the L occupancy of HD^+ at 300 K for $L = 0$ to $L = 6$. Higher L states obviously are less occupied than $L = 6$ and are not shown here.

4.2.3 Determination of transition rates

Because of the hyperfine structure, the spectrum of the $(0,2) \rightarrow (8,3)$ electric dipole transition consists of a large number of hyperfine components. Together with Doppler broadening, this leads to an irregular lineshape function. In addition, the excitation laser may address multiple hyperfine states simultaneously, which are furthermore coupled to other rotational states by the ambient 300 K blackbody radiation (BBR) field. Therefore, for the analysis of the $(0,2) \rightarrow (8,3)$ signal we develop a model based on Einstein rate equations which take all resonant molecule-electric field interactions into account. We note that at 300 K, states with $v = 0$ and $L = 1-6$ are significantly populated, with 27% in $L = 2$ (see Fig. 4.2). Below, we calculate the Einstein rate coefficients at the level of individual hyperfine states for transitions driven by the laser and BBR fields.

Following the approach of Koelemeij [93], we first ignore hyperfine structure and solve the radial Schrödinger equation which gives the radial wave function of nuclear motion $\chi_{v,L}$:

$$-\frac{\hbar^2}{2\mu} \frac{d^2}{dR^2} \chi_{v,L}(R) + \left[V(R) + \frac{\hbar^2 L(L+1)}{2\mu_{\text{red}} R^2} \right] \chi_{v,L}(R) = E_{v,L} \chi_{v,L}(R) \quad (4.4)$$

where R is the nuclear separation, μ_{red} stands for the reduced mass of the molecule, v labels vibrational state, L is the angular momentum and $E_{v,L}$ is the ro-vibrational energy. $V(R)$ is the potential energy curve belonging to the 1σ electronic ground state of HD^+ which is shown in Fig. 4.4a. The transition dipole moment is then given by

$$\mu_{vv'LL'} = \int_0^\infty \chi_{v',L'}(R) D_1(R) \chi_{v,L}(R) dR \quad (4.5)$$

where $D_1(R)$ denotes the permanent electric dipole moment of the $1s\sigma$ state which is calculated along with the potential energy curve in [42].

To take hyperfine structure into account we write the dipole transition matrix elements between the states $\phi_{\tilde{F}\tilde{S}JM_J}\chi_{v,L}$ and $\phi_{\tilde{F}'\tilde{S}'J'M'_J}\chi_{v',L'}$ as [93, 110, 111]:

$$\begin{aligned}
 & \langle \phi_{\tilde{F}\tilde{S}JM_J}\chi_{v,L} | \vec{E} \cdot \vec{\mu} | \phi_{\tilde{F}'\tilde{S}'J'M'_J}\chi_{v',L'} \rangle \\
 &= \sum_{F'S'} \beta_{FSJ} \beta_{F'S'J}^* E_p (-1)^{J+J'+S-M_J+1+L'+L} \\
 & \quad \times [(2J+1)(2J'+1)(2L+1)(2L'+1)]^{1/2} \\
 & \quad \times \begin{pmatrix} L & 1 & L' \\ M_J & p & M_J - p \end{pmatrix} \begin{pmatrix} L & 1 & L' \\ 0 & 0 & 0 \end{pmatrix} \begin{Bmatrix} L' & J' & S \\ J & L & 1 \end{Bmatrix} \\
 & \quad \times \mu_{vv'LL'}. \tag{4.6}
 \end{aligned}$$

Here we have used a transformation from the molecule fixed frame to the laboratory frame with $p = -1, 0, 1$ denoting the polarization state of the electric field with respect to the laboratory frame [110].

The linestrength is subsequently calculated by squaring and summing over the M_J states [112]:

$$S_{\alpha\alpha'} = \sum_{M_J} |\langle \phi_{\tilde{F}\tilde{S}JM_J}\chi_{v,L} | \vec{E} \cdot \vec{\mu} | \phi_{\tilde{F}'\tilde{S}'J'M'_J}\chi_{v',L'} \rangle|^2, \tag{4.7}$$

with $\alpha \equiv vLFSJ$. The Einstein rate coefficients for spontaneous emission, absorption and stimulated emission ($A_{\alpha\alpha'}$, $\bar{B}_{\alpha'\alpha}$ and $B_{\alpha\alpha'}$) are obtained through the relations

$$A_{\alpha\alpha'} = \frac{2\omega_{vv'LL'}^3}{3\epsilon\hbar c^3} \frac{S_{\alpha\alpha'}}{2J'+1} \tag{4.8}$$

$$B_{\alpha\alpha'} = \frac{\pi^2 c^3}{\hbar\omega_{vv'LL'}^3} A_{\alpha\alpha'} \tag{4.9}$$

$$\bar{B}_{\alpha'\alpha} = \frac{2J'+1}{2J+1} B_{\alpha\alpha'}. \tag{4.10}$$

Note that we use the hyperfineless transition frequency $\omega_{vv'LL'}$ rather than $\omega_{\alpha\alpha'}$, which has a negligible effect on the value of the rate coefficients. These results are used in Sec. 4.4.1 to calculate the expected $(0,2) \rightarrow (8,3)$ signal, which is incorporated into a model describing the dynamics during the spectroscopic measurement.

4.3 Experiment

4.3.1 Trapping and cooling Be^+ and HD^+

To achieve narrow linewidths and small systematic shifts, we choose to perform spectroscopy on small samples of HD^+ molecules in a radiofrequency (rf) ion trap. We reduce the motional temperature of the HD^+ ions by storing them together with HD^+ ions which are Doppler-cooled by a continuous-wave (cw) 313 nm laser beam (see [75,93] and [113] for details). The rf trap is placed inside an ultra-high vacuum chamber with a background pressure of 1×10^{-10} mbar. The rf trap operates at a frequency of 13.2 MHz, leading to Be^+ radial trap frequencies of $\omega_r = 2\pi \times 290$ kHz. The trap geometry and rf circuitry are designed so as to minimize unwanted rf fields and phase differences between the rf electrodes. The two dc electrodes are segmented into two endcaps and a center electrode (Fig. 4.3). The dc voltages of the center electrodes, rf electrodes and endcap pairs can be individually adjusted to compensate stray electric fields. Be^+ and HD^+ are loaded by electron-impact ionization as done by Blythe *et al.*, and monitored with a photomultiplier tube (PMT) and an electron-multiplied charge-coupled-device (EMCCD) camera [114]. EMCCD images show ellipsoidal mixed-species Coulomb crystals, with a dark core of molecular hydrogen ions surrounded by several shells of fluorescing Be^+ ions. The apparatus and procedures for loading and compensation of stray electric fields is described in more detail in [93].

4.3.2 Spectroscopy of HD^+

The $(0,2) \rightarrow (8,3)$ transition in HD^+ is detected destructively through resonance enhanced multi-photon dissociation (REMPD), see Fig. 4.4a. A 782 nm cw titanium:sapphire laser is used to excite HD^+ from its vibrational ground state to the $v=8$ state, which is efficiently dissociated by the field of a co-propagating 532 nm cw laser beam. Both lasers are directed along the trap axis and counter-propagate the 313 nm laser (see Fig. 4.3). Since all HD^+ are initially in the vibrational ground state, dissociation via the $v=8$ level only takes place if the 782 nm laser is resonant with the $(0,2) \rightarrow (8,3)$ transition. We used 90 mW of 532 nm radiation, focused to a beam waist of $140 \mu\text{m}$, which is sufficient to dissociate an HD^+ molecule from this level within a few ms, much faster than the spontaneous decay of the $v=8$ state (lifetime 12 ms).

A single REMPD cycle lasts 10 seconds. During the first seconds of REMPD the majority of the HD^+ in $L=2$ is dissociated, leading to depletion of the $L=2$ state (Fig. 4.4). During the remainder of the cycle, BBR repopulates the $L=2$ state from other rotational levels, and this enhances the number of dissociated HD^+ ions by approximately a factor of 2.

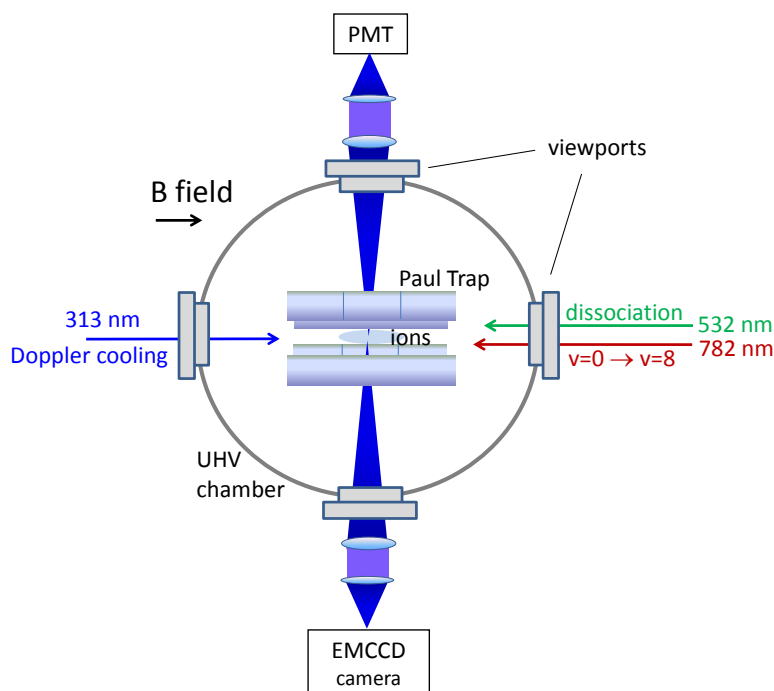


Figure 4.3: Schematic view of the trap setup. An ultrahigh vacuum (UHV) chamber houses a linear rf trap in which Be^+ ions and deuterated molecular hydrogen ions are loaded by electron-impact ionization. Be^+ ions are Doppler-cooled by the 313 nm laser, which is directed in parallel to the trap axis and B field direction. The 313 nm Be^+ fluorescence is imaged onto and detected with a PMT and an EMCCD camera. The 782 nm and 532 nm cw REMPD lasers are overlapped with the 313 nm laser and the ions, but propagate in the opposite direction.

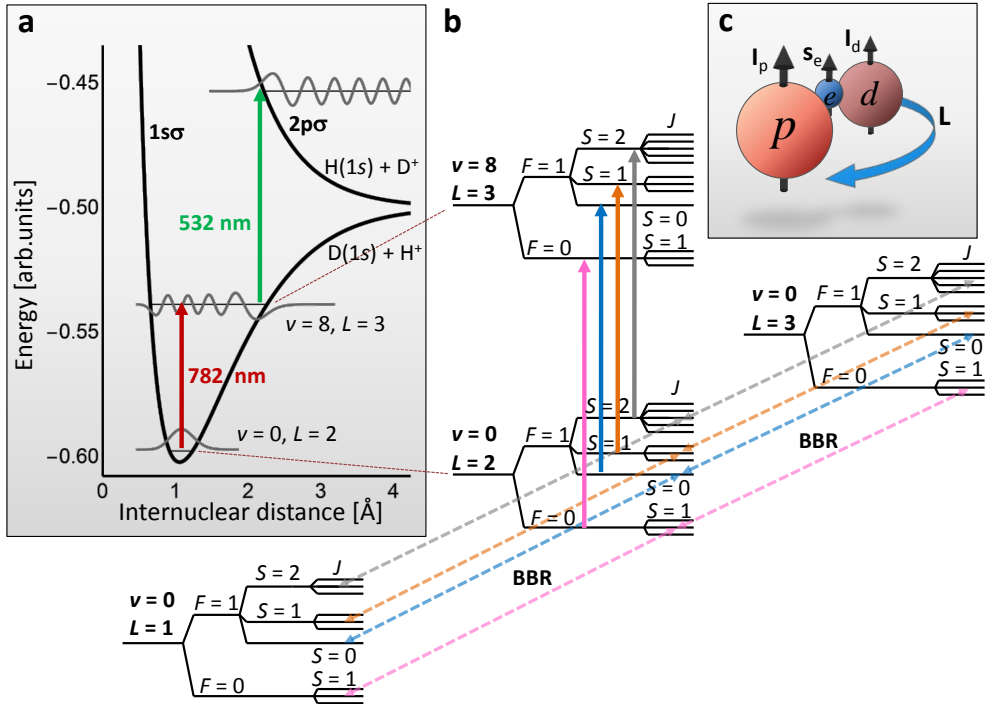


Figure 4.4: (a) Potential energy curves of the $1s\sigma$ and $2p\sigma$ electronic states are plotted together with the radial nuclear wave functions for $v=0$, $v=8$ and for the dissociative wave function in the $2p\sigma$ state. The REMPD scheme is also shown, with the red arrow indicating the $(v, L): (0, 2) \rightarrow (8, 3)$ transition by the 782 nm laser and the green arrow corresponding to the 532 nm photon which photodissociates the molecule. (b) Detailed partial level scheme showing the $(0, 2) \rightarrow (8, 3)$ transition including hyperfine levels together with the BBR interaction which couples the rotational levels $L=1, 2, 3$. Coupling to $L=0$ and $L=4, 5, 6$ also occurs, but is not shown here. (c) A schematic view of the HD^+ molecule showing the angular momenta responsible for the hyperfine structure and rotational motion.

The 782 nm laser has a linewidth of ~ 0.5 MHz and is frequency-stabilized by locking its frequency to a nearby mode of a self-referenced optical frequency comb laser. To this end, a 63.5 MHz beat note is created by mixing the light of the 782 nm laser and the frequency comb. The frequency comb itself is locked onto a rubidium atomic clock for short-term stability, which is disciplined to the 1-pps signal of a GPS receiver for long-term accuracy and traceability to the SI second. The resulting relative accuracy of the frequency measurement system is 2×10^{-12} .

The ~ 25 strongest hyperfine components of the $(0, 2) \rightarrow (8, 3)$ transition are located in the range (-110 MHz, 140 MHz) around the hyperfine-less frequency. As we expect Doppler broadening to ~ 16 MHz, we divide this range into a set of 140 evenly spaced frequencies at which REMPD spectroscopy is performed. To convert possible time-varying systematic effects into random noise, we randomize the ordering of the frequency list. For each frequency point, six to seven REMPD measurements are made, which gives us a set of ~ 900 REMPD measurements in total.

During REMPD, about 300 mW of 782 nm light is used with a beam waist of $\sim 120 \mu\text{m}$ at the location of the ions. The 313 nm cooling laser is detuned to -80 MHz from the cooling resonance and reduced in power to $\sim 70 \mu\text{W}$, which results into an intensity of two times the saturation intensity of the 313 nm cooling transition, and leads to an ion temperature of about 10 mK.

To obtain a measure of the fraction of HD⁺ ions lost during REMPD, we employ so-called secular excitation [115]. This procedure is based on the indirect heating of the Be⁺ which occurs when the motion of HD⁺ ions is resonantly excited by an additional radial rf field. The heating of Be⁺ leads to a change of the 313 nm fluorescence, which is connected to the number of HD⁺ ions. Before and after each REMPD cycle an rf frequency scan is scanned over the secular motional resonance of HD⁺ at ~ 830 kHz. This induces a temporal rise of temperature in the Coulomb crystal up to a few Kelvin. At a detuning of the 313 nm cooling laser of -300 MHz and using a few mW of laser power, such a ‘secular scan’ shows up as a peak of the 313 nm beryllium fluorescence yield (see Fig. 4.5). In Appendix B we show that the area under this peak, A , scales with the number of HD⁺ ions, although not linearly. A single measurement cycle consists of a secular scan (10 s), followed by 10 s of REMPD and another 10-s secular scan (see Fig. 4.5). We define our spectroscopic signal as the relative difference between the areas of the initial and final secular scan peaks:

$$S = \frac{A_i - A_f}{A_i} \quad (4.11)$$

Repeating this procedure for all frequencies ν of the 782 nm laser while recording fluorescence traces with both the PMT and EMCCD camera, we obtain a total set of 1772 of data points (ν, S) .

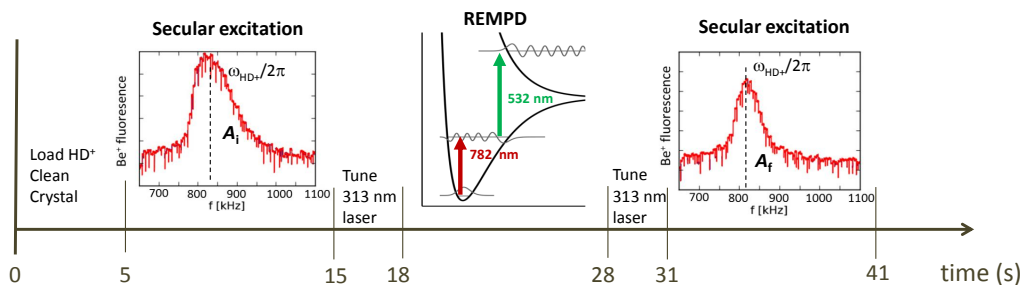


Figure 4.5: The secular scan - REMPD - secular scan detection scheme. Each cycle starts with loading a new sample of HD^+ ions in the ion trap. During loading the Be^+ ions are exposed to neutral HD gas, leading to the formation of a small number of BeH^+ and BeD^+ ions (see also Table 4.1). These are expunged from the trap by applying a dc quadrupole potential of ~ 0.9 V, which reduces the trap depth such that only ions with mass ≤ 9 amu remain trapped (see Sec. 2.2). Five seconds after loading, the HD^+ is motionally excited by scanning an rf electric field over the secular motional resonance frequency at 830 kHz. A 313 nm laser detuning of -300 MHz is used, in which case the secular excitation results in a rise in the Be^+ fluorescence. Ten seconds later, the 313 nm laser is detuned to -80 MHz from the Be^+ resonance and its intensity reduced to $I \sim 2I_{\text{sat}}$. After 10 s of REMPD, the 313 nm laser settings are restored to their values as used for the first secular scan, and a second secular scan is executed. A smaller 313 nm fluorescence peak indicates loss of HD^+ .

4.4 Results and Discussion

4.4.1 A spectral lineshape model

In order to determine the spinless ro-vibrational $(0,2) \rightarrow (8,3)$ transition in HD^+ , having frequency ν_0 , we need a realistic lineshape model which includes the relevant physics present during REMPD. Here the aim is to obtain a spectral lineshape function which parametrizes all effects. Parameters are estimated by independent means where possible, or included as a fit parameter otherwise. Importantly, the fit function will contain $\nu - \nu_{0,\text{fit}}$, where $\nu_{0,\text{fit}}$ is a fit parameter from which we later deduce the value of ν_0 . Before fitting, the (ν, S) data is corrected for reactions with background gas (primarily H_2). This procedure is described below in Sec. 4.4.5.

We start with building a state vector $\rho(t)$ which contains the population in all 62 hyperfine levels in the rotational states ranging from $L=0$ to $L=5$ in the $v=0$ level. This includes 97.6% of the total internal states of $v=0$ given a blackbody-radiation temperature of 300 K. We neglect the Zeeman splitting

due to 0.19 mT B-field at the location of the trapped ions, as this splitting is negligibly small compared to the Doppler linewidth and the width of the BBR spectrum. The lineshift due to the Zeeman effect is considered separately in Sec. 4.4.6. Also the Stark effect, the electric-quadrupole shift and 2nd order Doppler shift are not included in this model, but addressed in Sec. 4.4.6.

During the 10 s of REMPD the hyperfine levels in the $L=2$ initial state interact with the 782 nm laser and BBR. We here make the simplifying assumption that any population in the $v = 8$ target state will be dissociated by the 532 nm laser. The interaction with the 782 nm laser is therefore modeled as a simple loss process. The evolution of the state vector $\rho(t)$ is obtained by solving the set of coupled rate equations:

$$\frac{d\rho(t)}{dt} = M_R \rho(t) + M_{\text{BBR}} \rho(t), \quad (4.12)$$

where M_R and M_{BBR} are the matrices describing the interaction with the REMPD lasers and BBR field. The matrix elements of M_R are given by

$$M_{R,ij} = B_{ij} D_z(\omega, T_{\text{HD}^+}) I_{\text{laser}}/c, \quad (4.13)$$

where B_{ij} denotes the Einstein coefficient belonging to a particular transition between hyperfine levels in $v = 0$ and $v = 8$. I_{laser} is the intensity of the 782 nm laser and D_z represents a normalized response function averaged over the distribution of z -velocities of the HD⁺ ions. This involves an integration over all frequencies $\omega = \omega' - k_z v_z$, where ω' is the (fixed) angular frequency of the 782 nm laser in the laboratory frame, k_z the wavevector of the laser and v_z the velocity in the z -direction. If the HD⁺ velocity distribution is thermal (Gaussian), D_z depends only on the temperature in the z -direction, T_{HD^+} . However, the effects of micromotion and chemistry during REMPD in the Coulomb crystal lead to deviations from a thermal distribution. This implies that D_z cannot be described by a single Gaussian lineshape. In Secs. 4.4.3 and 4.4.4 those processes are explained in detail and the precise shapes of D_z are determined.

M_{BBR} is given by

$$M_{\text{BBR}} = A_{ij} + (\bar{B}_{ij} + B_{ji}) W(\omega, T_{\text{BBR}}) \quad (4.14)$$

with A_{ij} , \bar{B}_{ji} and B_{ij} the Einstein coefficients of spontaneous emission, absorption and stimulated emission by BBR, respectively. $W(\omega, T_{\text{BBR}})$ denotes the BBR energy distribution function, which is given by:

$$W(\omega, T_{\text{BBR}}) = \frac{\hbar\omega^3}{\pi^2 c^3} \left(e^{\frac{\hbar\omega}{k_B T_{\text{BBR}}}} - 1 \right)^{-1}. \quad (4.15)$$

Since the typical frequency of the internal degrees of freedom (> 1 THz) differs from that of the external degrees of freedom (< 1 MHz) by many orders of

magnitude, any energy transfer mechanism between them must be of extremely high order and consequently negligibly small. Laser cooling of the external degrees of freedom may therefore be expected to have no significant effect on the temperature of the internal degrees of freedom, which are coupled strongly to (and in equilibrium with) the BBR field [116].

We use MATHEMATICA to solve Eq. (4.12) in order to obtain $\rho(t)$. We subsequently find the relative HD⁺ loss, ϵ , by summing over the hyperfine state populations (62 hyperfine states in $v, L=(0,2)$) before ($t = 0$) and after ($t = 10$) REMPd and computing:

$$\epsilon = \frac{N_i - N_f}{N_i} = \frac{\sum_j^{62} \rho_j(0) - \rho_j(10)}{\sum_j^{62} \rho_j(0)}. \quad (4.16)$$

Here N_i and N_f are the numbers of HD⁺ ions present in the trap directly before and after REMPd, respectively. Note that for a thermal ensemble of HD⁺ ions, $\epsilon \equiv \epsilon(\nu - \nu_{0,\text{fit}}, T_{\text{HD}^+}, I_{\text{laser}})$, which is furthermore assuming an blackbody radiation field at $T = 300$ K.

The question arises what the relation is between the signal S defined in Eq. (4.11) and the fractional loss ϵ defined above. In previous work it was assumed that S and ϵ are interchangeable [63, 93, 115, 117]. In Appendix B we study the dependence of the signal S on the initial number of ions N_i and the dissociated fraction ϵ in detail using realistic molecular dynamics (MD) simulations. We find that the fraction ϵ (which is a theoretical construct) can be mapped to the 'signal domain' S by use of a slightly nonlinear function,

$$S_{\text{fit}} = f_{\text{NL}}(\bar{T}_0, \epsilon) \quad (4.17)$$

where \bar{T}_0 is defined as the average Be⁺ temperature along the z -axis during the initial secular scan of the REMPd cycle. This means we have to use a five-dimensional fit function

$$S_{\text{fit}}(\bar{T}_0, \epsilon(\nu - \nu_{0,\text{fit}}, T_{\text{HD}^+}, I_{\text{laser}})) = S_{\text{fit}}(\nu - \nu_{0,\text{fit}}, T_{\text{HD}^+}, I_{\text{laser}}, \bar{T}_0). \quad (4.18)$$

An analytical solution of the fit function proves difficult to find, whereas a numerical implementation of the fit function takes excessively long to compute. Therefore we compute values of S_{fit} on a dense grid of values $(\nu - \nu_{0,\text{fit}}, T_{\text{HD}^+}, I_{\text{laser}}, \bar{T}_0)$, which we interpolate (again using MATHEMATICA) to find a fast, continuous and smooth approximation to the function S_{fit} , which is suitable for nonlinear least squares fitting. A 3D projection of this interpolated function (assuming fixed values of I_{laser} , \bar{T}_0 and $\nu_{0,\text{fit}}$) is plotted in Fig. 4.6. The reason for treating I_{laser} as a fit parameter instead of inserting a single fixed value is the following. The entire spectroscopy measurement is divided into 15 sessions each taken at a different day. To ensure reproducible laser

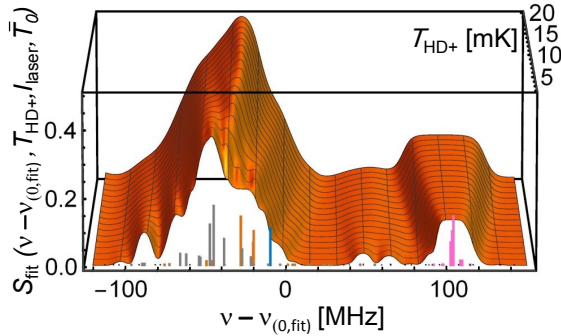


Figure 4.6: A plot of the fit function S_{fit} with $I_{\text{laser}}=1.0 \times 10^7 \text{ Wm}^{-2}$, $\bar{T}_0=4 \text{ K}$ and $\nu_{0,\text{fit}} = \nu_{\text{th}}$. On the frequency axis, the theoretical values of transitions between the particular hyperfine levels are depicted as sticks. The height of the sticks corresponds to their linestrengths. The colors of the sticks are the same colors used in Fig. 4.4 and distinguish different groups of transitions with similar F and S quantum numbers. For decreasing HD⁺ temperature, Doppler broadening is reduced and the hyperfine structure becomes more resolved. Effects of saturation are also visible in the spectrum.

beam intensities from session to session, we used diaphragms to overlap all laser beams with the 313 nm cooling laser, which itself is aligned with the Be⁺ Coulomb crystal visually using the EMCCD camera. Using a mock version of this setup, we verified that this procedure leads to beam pointing errors up to 40 μm . Assuming a Gaussian distribution of beam pointing errors, we find an intensity at the location of the HD⁺ ions which varies from the intensity in the center of the beam by a factor of 0.6 to 1. Since the spectral line shape is strongly saturated, these variations of the intensity only lead to small signal changes. It is therefore allowed to treat I_{laser} as a free fit parameter which represents the average 782 nm laser intensity for all data points. Similarly, the variables T_{HD^+} and \bar{T}_0 cannot be determined accurately *a priori* and are treated as free fit parameters as well.

4.4.2 Estimation of absolute trapped ion numbers

As explained in Sec. 4.4.4, effects of chemistry in the Coulomb crystal significantly influence the measured lineshape of the (0,2)→(8,3) transition. The impact of such effects depends on (and can be estimated from) the absolute numbers of beryllium ions and molecular hydrogen ions. In order to estimate absolute numbers we combine results from MD simulations and spectroscopy. Similar as observed by Blythe *et al.* [114], our mixed-species ion ensembles

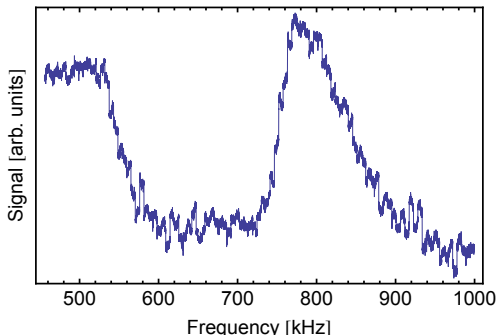
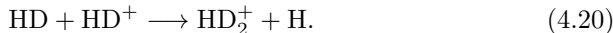


Figure 4.7: Fluorescence at 313 nm recorded by the PMT during a secular scan from 450 to 1000 kHz. The peak at 800 kHz indicates the presence of trapped HD^+ . The fluorescence signal at 500 kHz indicates the presence of particles with a charge-to-mass ratio of 1:4 and 1:5 which can be attributed to H_2D^+ and HD_2^+ . Note that peaks belonging to the two species overlap and are not resolved.

contain not only Be^+ and HD^+ , but also BeH^+ , BeD^+ , H_2D^+ , and HD_2^+ . In this paragraph we focus on the latter two species which are created during the HD^+ loading procedure through the exothermic reactions



and



Triatomic hydrogen ions can be detected by secular excitation. An example is shown in Fig. 4.7, where the peak in the PMT signal at the left is attributed to the overlapping peaks belonging to species with charge-to-mass ratios 1:4 and 1:5, corresponding to H_2D^+ and HD_2^+ , respectively. In rf traps, lighter species experience stronger confinement (Sec. 2.2). This is evident from EMCCD camera images which exhibit fluorescing Be^+ ions surrounding a dark core of lighter species (Fig. 4.8). The size of the core reflects the total number of light ions. We analyze this by means of MD simulations (Appendix A), from which a relation is obtained between the size of the dark core and the number of trapped ions. By comparing simulated and real EMCCD images, an average number of ~ 750 Be^+ ions is obtained. From the analysis of the intensity profiles, we cannot distinguish the HD^+ from the triatomic molecular species. To solve this we use a collection of 140 EMCCD images taken before and after REMPD while the 782 nm laser was tuned at the same fixed frequency near the maximum of the $(0,2) \rightarrow (8,3)$ spectrum. From the lineshape model we estimate that the average relative HD^+ loss is 0.57 at this frequency. By comparing the

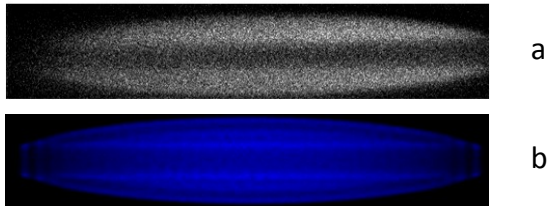


Figure 4.8: (a) An EMCCD image of the Be^+ fluorescence just before a secular scan. (b) An image of ions obtained from a MD simulation based on 750 Be^+ ions and 50 ions with masses 3, 4 and 5 amu

EMCCD images taken before and after REMPD with the simulated images, we also determine the total initial and final numbers of light ions. Combining this with the expected loss of 57 % of the HD^+ ions, we infer the ratio of HD^+ numbers to heavier molecular species (H_2D^+ , HD_2^+). An average number of 43 HD^+ ions is obtained together with 60 ions of heavier species. We cannot determine the relative abundance of H_2D^+ and HD_2^+ , but previous observations indicate a branching ratio between Eqs. (4.19) and (4.20) of 1:1 and, thus, equal abundances [53, 118]. The set of EMCCD images shows an appreciable spread in the size of the dark core and, in particular, the ratio of HD^+ to heavier triatomic hydrogen ions. Variations in both are due to uncontrolled shot-to-shot fluctuations of the HD background pressure during HD^+ loading. The resulting standard deviation of the number of HD^+ is 41 ions. This also indicates that analysis of EMCCD images (under the present conditions) is not suitable to replace the signal obtained by mass-selective secular excitation (Eq. (4.11)).

For the treatment of effects of chemistry on the lineshape below, we consider two scenarios:

- Scenario a: $N_{\text{HD}^+} = 43$, $N_{\text{H}_2\text{D}^+} = N_{\text{HD}_2^+} = 30$
- Scenario b: $N_{\text{HD}^+} = 84$, $N_{\text{H}_2\text{D}^+} = N_{\text{HD}_2^+} = 60$,

where scenario b reflects the one sigma upper variation.

4.4.3 Effect of micromotion

The rf quadrupole field of the ion trap inevitably leads to micromotion of ions with non-zero displacement from the trap z -axis. In addition, excess micromotion may be caused by unwanted rf fields arising from geometrical

imperfections of the trap electrode structure or phase differences between the rf electrodes [87]. In an ideal linear rf trap, micromotion is strictly radially oriented, but small imperfections in the trap geometry can cause excess micromotion with a component along the trap axis and laser direction, thus adding sidebands to each hyperfine component in the $(0,2)\rightarrow(8,3)$ spectrum. Due to the combination of an asymmetric and saturated lineshape of the $(0,2)\rightarrow(8,3)$ spectrum, these sidebands can lead to a shift of ν_0 . Therefore the micromotion amplitude along the 782 nm laser needs to be determined. As the laser propagates virtually parallel to the trap axis, and since the HD^+ ions are always located near the trap axis, we are primarily concerned with the possible axial micromotion component.

The HD^+ axial micromotion amplitude x_{HD^+} , can be determined through fluorescence measurements of a trapped string of beryllium ions by using a modified version of the photon-rf field correlation technique [87]. The idea here is to displace a string of about 10 Be^+ ions by $\sim 100 \mu\text{m}$ by applying a static offset field. This will induce significant radial micromotion, in addition to the axial micromotion. The 313 nm cooling laser propagates at an unknown but small angle θ ($\theta < 10 \text{ mrad}$) with respect to the trap axis, and may therefore have a nonnegligible projection along the radial direction. In Appendix C we show that if the rf voltage, V_0 , is varied, the axial micromotion amplitude scales linearly with V_0 , while the radial one varies as θ/V_0^2 . The latter behavior stems from the V_0 -dependent confinement and the concomitant variation of the Be^+ radial displacement with V_0 . Thus, measuring the micromotion amplitude for various values of V_0 allows separating the radial and axial contributions.

To determine the micromotion amplitude, we use a similar setup as described in [87]. Photons detected with the PMT are converted to electrical pulses and amplified by an amplifier-discriminator, which generates a START pulse at time t_i . Subsequently, a STOP pulse is generated at time t_f through another amplifier-discriminator at the first downward zero crossing of the rf signal. A time-to-amplitude converter (TAC) converts the duration between the START and STOP pulses to a voltage. We record the TAC output voltage with a digital phosphor oscilloscope for 400 ms. We subsequently process the stored voltage trace with a computer algorithm to obtain a histogram of START-STOP time delays, employing 1-ns bins in a range 0-76 ns (*i.e.* one rf cycle). The bin heights thus reflect the scattering rate as a function of the rf phase, and micromotion will lead to a modulation of the scattering rate about its mean value (Fig. 4.9). The Be^+ scattering rate (indicated as R^{MB} , where

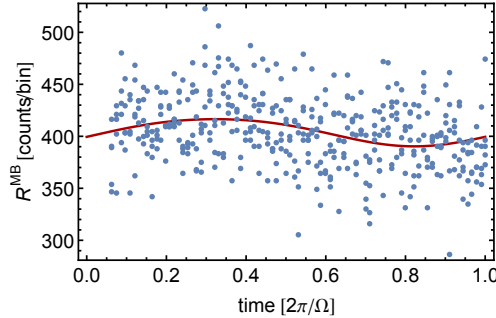


Figure 4.9: Be^+ Fluorescence modulation detected with the TAC setup. The data are fitted using Eq. (4.21).

MB stands for Maxwell-Boltzmann) is given by:

$$R^{\text{MB}} = \frac{\Gamma}{2} \sqrt{\frac{m_{\text{Be}}}{2\pi k_B T}} \int \frac{I/I_{\text{sat}}}{I/I_{\text{sat}} + 1 + (2(\Delta - \mathbf{k} \cdot (\mathbf{v}_\mu - \mathbf{v}))/\Gamma)^2} \exp\left(-\frac{m_{\text{Be}} v^2}{2k_B T}\right) dv \quad (4.21)$$

where m_{Be} is the Be^+ mass, T is the Be^+ temperature, I and I_{sat} the laser intensity and saturation intensity respectively, $\Delta = 2\pi \times -25$ MHz is the detuning of the 313 nm laser light, \mathbf{k} the wavevector of the 313 nm laser, and \mathbf{v} and \mathbf{v}_μ the secular and micromotion velocities of the Be^+ ions. While the rf voltage is being varied, the 313 nm laser is displaced so that the ions always are at the maximum of the Gaussian laser intensity profile. The $\mathbf{k} \cdot \mathbf{v}_\mu$ term can be written as

$$\mathbf{k} \cdot \mathbf{v}_\mu = k x_{0,k} \Omega \sin(\Omega(t - t_0)), \quad (4.22)$$

where $x_{0,k}$ is the amplitude of Be^+ micromotion along the direction of the laser wavevector and t_0 is a time offset. We extract $x_{0,k}$ by fitting Eq. (4.21) to the acquired fluorescence histogram. Repeating this procedure for various values of V_0 , a list of data points of the form $(V_0, x_{0,k})$ is obtained. We subsequently extract the radial and axial micromotion components by fitting a model function to these data. The model function is derived in Appendix C.

The procedure of displacing a string of Be^+ ions and varying V_0 is carried out for both the horizontal and vertical directions. The data and fit functions are shown in Fig. 4.10 and an average axial micromotion amplitude x_{HD} of 11(4) nm is found. As explained in Appendix C, the radial micromotion contribution (due to a possible small angle of the 782 nm laser with the trap axis) averages to zero.

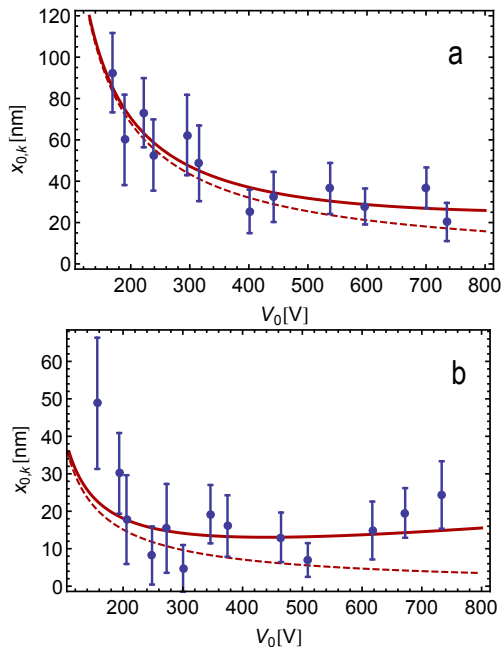


Figure 4.10: Be^+ micromotion amplitude along the 313 nm wavevector versus rf voltage amplitude for an offset in the horizontal (Fig. 4.10a) and vertical (Fig. 4.10b) direction. The red solid curve is the model fit function [Eq. (C.8)] which includes x_{HD^+} as a fit parameter. For comparison the fitted curve with $x_{\text{HD}^+} = 0$ is also shown (dashed curve).

We incorporate the micromotion effect by extending the lineshape function D_z in Eq. (4.13) with sidebands at frequencies $m\Omega$ with amplitudes $J_m^2(k_{782}x_{\text{HD}^+})$. Here, the J_m are Bessel functions of the first kind, with m an integer in the range $[-3, 3]$.

4.4.4 Effects of chemistry in the Coulomb crystal

During REMPD, H_2 molecules from the background gas can react with the ions in the Coulomb crystal. Those reactions can be divided into two classes: (i) elastic collisions, and (ii) inelastic collisions, during which a chemical reaction or charge exchange occurs, and chemical energy is converted to kinetic energy. In general, the kinetic energy transfer to the ion from elastic collisions with room-temperature particles is much lower than the chemical energy released from inelastic collisions.

4. HIGH-PRECISION SPECTROSCOPY OF THE HD⁺ MOLECULE

At close range r , the electric field of the ion polarizes the neutral molecule which results in an attractive interaction potential $U(r) = -\alpha Q^2/(8\pi\epsilon_0 r)^4$. Here α denotes the polarizability volume (in m³)¹ of the molecule, ϵ_0 is the electric constant, and Q is the elementary charge. If we integrate the interaction force over the trajectory of the neutral near the ion (assuming a relatively large impact parameter $b > b_{\text{crit}}$; see below), we obtain a change of momentum which corresponds to a velocity kick of tens of meters per second for most species.

If a neutral atom or molecule and an ion approach each other within a critical impact parameter $b_{\text{crit}} = (\alpha q^2/\pi\epsilon_0\mu_{\text{red}}v)^{1/4}$, where μ_{red} and v are the reduced mass and relative velocity of the pair, a so called Langevin collision occurs, during which particles spiral towards each other and a chemical reaction can occur at very short range [119]. The chemical reaction products contain hundreds of meV of kinetic energy, which is dissipated into the ion crystal which itself only contains about 2 meV of kinetic energy (at 10 mK). A possible adverse side effect is that such collisions may lead to time-averaged velocity distributions which deviate from thermal distributions. Table 4.1 shows the relevant reactions during REMPD along with the released chemical energy and their reaction rates. Reaction (1) corresponds to the REMPD process itself. From observations reported in [42] we infer that the ratio of HD⁺ → D⁺ + H and HD⁺ → H⁺ + D is approximately 1:1. The charge-to-mass ratio of H⁺ is too large for this product to be stably trapped, but the D⁺ ions can stay

Table 4.1: Chemical reactions occurring in the Coulomb crystal during REMPD.

Nr	Reaction	Energy of ionic product (eV)	Rate(s ⁻¹)
1)	HD ⁺ + $h\nu + h\nu'$ → D ⁺ + H	0.41	0-10 ²
2)	HD ⁺ + H ₂ → H ₂ D ⁺ + H	0.36	0.0042
3)	HD ⁺ + H ₂ → H ₃ ⁺ + D	0.66	0.0014
4)	H ₂ D ⁺ + H ₂ → HD + H ₃ ⁺	0.016	0.0019
5)	HD ₂ ⁺ + H ₂ → D ₂ + H ₃ ⁺	0.017	0.0004
6)	HD ₂ ⁺ + H ₂ → HD + H ₂ D ⁺	0.022	0.0015
7)	Be ⁺ (² P _{3/2}) + H ₂ → BeH ⁺ + H	0.25	0.0019/0.005 ³

² The rate (in s⁻¹ per molecule) of D⁺ production is dependent on time and frequency in the (0,2)→(8,3) spectrum.

³ The rate is dependent on the fraction of time a Be⁺ ion spends in the excited ²P_{3/2} state, which is dependent on the 313 nm laser intensity and detuning (−80 MHz or −300 MHz, respectively).

¹The polarizability volume and the polarizability in SI units are related through $\alpha = \alpha_{\text{SI}}/(4\pi\epsilon_0)$

trapped and can orbit the Coulomb crystal for many seconds. The reaction rate of (1) is calculated from the REMPD model described in Sec. 4.4.1, and is dependent on the frequency of the 782 nm laser.

Reaction (7) occurs most frequently due to the large number of Be^+ ions present in the trap. The reaction rate is obtained from a decay measurement of the 313 nm fluorescence from a loaded Be^+ crystal, and is in good agreement with the rate estimated from the Langevin cross section given the background pressure of 1×10^{-8} Pa in our apparatus [120]. The different rate constants of reactions (2) and (3) illustrate the fact that HD^+ can react with H_2 in two ways: either the H_2 breaks apart, donating an H atom to the HD^+ molecule, or the HD^+ breaks apart, after which an H^+ or D^+ is added to the neutral molecule. According to [53] and [118] the probability of each scenario is approximately 50 %. In case the ion breaks apart, the probability that either a H^+ or a D^+ is donated to the H_2 molecule is also 50 %. This leads to a ratio of reaction (2) to (3) of 3:1. The rate of reaction (2) can be measured (keeping in mind that HD^+ and H_3^+ in reaction (3) have the same charge-to-mass ratio and therefore cannot be distinguished) by applying the measurement scheme depicted in Fig. 4.5 without 782 nm laser, which is further described in Sec. 4.4.5. The rates of reactions (4), (5) and (6) are obtained from [121]. The kinetic energies of the chemical products are calculated by using the binding energies and energy and momentum conservation laws.

Realistic MD simulations show that the fast ionic chemical products may heat up the Coulomb crystal by 1–2 mK (depending on the REMPD rate), and that the HD^+ velocity distribution becomes slightly non-thermal. A MD simulation of a Coulomb crystal containing 750 laser-cooled Be^+ ions, 40 sympathetically cooled HD^+ ions and 14 fast D^+ ions produces the HD^+ z -velocity distribution shown in Fig. 4.11. A detailed explanation of the MD code is given in Appendix A. It turns out that the z -velocity distribution deviates clearly from a Gaussian curve and is better described by a q -Gaussian [122], which is a Gaussian curve with higher wings parameterized by a parameter q :

$$Q(\omega, \beta, q) = \frac{\sqrt{q-1} \left(1 + \frac{(q-1)(\omega_0 - \omega)^2}{2\beta^2}\right)^{\frac{1}{1-q}} \Gamma\left(\frac{1}{q-1}\right)}{\sqrt{2\pi} \beta \Gamma\left(-\frac{q-3}{2(q-1)}\right)} \quad 1 < q < 3 \quad (4.23)$$

where ω and ω_0 are the frequency and center frequency, Γ is the gamma function, and β is analogous to the standard deviation of a Gaussian distribution, and which is related to the Doppler width. For $q = 1$, the function reduces to a regular Gaussian distribution. This function is merely used as a mathematical tool to describe the simulated data and we have not derived this velocity distribution based on a particular physical model. Since the value $\nu_{0,\text{fit}}$ turns out to be sensitive to the shape of the velocity distribution, it is important that

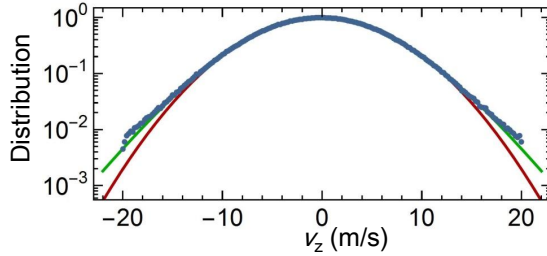


Figure 4.11: The z -velocity distribution of 43 HD⁺ molecules obtained from 100 ms simulation. 14 D⁺ ions with an initial velocity of 6300 ms⁻¹ heat up the ion crystal and give rise to a velocity distribution which differs slightly from a Gaussian (red curve, fitted temperature 11.60(3) mK) and is better described by a q -Gaussian (green curve, fitted temperature 11.00(3) mK, and fitted q parameter 1.070(3))

we insert the lineshape based on the correct velocity distribution in Eq. (4.13), and specify the bounds to within this distribution is valid. An initial analysis reveals that $\nu_{0,\text{fit}}$ may shift several hundreds of kHz by implementing a q -Gaussian with a q varying between 1.0 and 1.1. Note that recently, another study of MD simulations independently confirmed the non-thermal character of velocity distributions of laser-cooled ion crystals due to collisions with background gas molecules [123].

In the remainder of this section, we determine the q -values applicable to our REMPD measurement with the help of MD simulations. The value of q is dependent on the number of trapped fast ions, N_{fast} . The more fast ions, the higher the q -value. We note that N_{fast} is frequency dependent (more D⁺ produced near the peak of the REMPD spectrum) as well as time dependent (the production rate of D⁺ is governed by the rate equations, Eq. (4.12)).

When a fast ion collides with a cold ion, each particle may undergo a nonadiabatic transition to a different solution of the Mathieu equation which governs its motion in the trap [124]. This implies that a fast ion can either lose or gain energy during such a collision. Since the energy change per collision is relatively small, fast ions can retain their high speeds in the trap for many seconds. Values for N_{fast} can be obtained by solving the rate equation:

$$\frac{\partial N_{\text{fast}}}{\partial t} = \alpha_{\text{prod}} N_{\text{source}} - \alpha_{\text{relax}} N_{\text{fast}} - \alpha_{\text{esc}} N_{\text{fast}} \quad (4.24)$$

The term α_{prod} is the production rate from a number of N_{source} particles, such as Be⁺ or HD⁺. In Sec. 4.4.2 we determined $N_{\text{source,Be}^+} = 750$ and $N_{\text{source,HD}^+} = 43$ or $N_{\text{source,HD}^+} = 84$. α_{relax} is the rate at which fast ions are cooled and become embedded within the Coulomb crystal, while α_{esc} is the rate at which

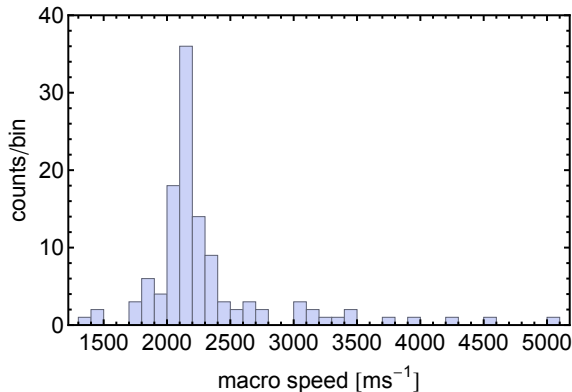


Figure 4.12: The (secular) speed distribution of approximately 100 BeH^+ ions after a simulated time of 100 ms. All BeH^+ ions had an initial velocity of 2200 ms^{-1} in random directions. Comparing such histograms for various initial velocities points out that there is a tendency for faster ions to acquire ever larger velocities (presumably by micromotion heating), which will ultimately lead to the loss of these ions. Likewise, ions which happen to slow down have an ever increasing chance to be cooled down to the 10 mK temperature of the Coulomb crystal.

ions escape from the trap. The values of α_{prod} correspond to the reaction rates in Table 4.1. However, obtaining such rates requires a multitude of individual MD simulations, with simulation periods of several seconds each. Even with current academic supercomputers, the total time to perform such simulations is prohibitively long. Nevertheless, boundaries on α_{relax} and α_{esc} can be inferred from many short simulations which can be run in parallel. We use a set of 10 simulations per fast ion species, each containing approximately 10 fast ions together with a trapped and laser-cooled Coulomb crystal of 750 Be^+ and 40 HD^+ ions. Each simulation lasts 100 ms, and at the start of each simulation the initial velocities of the ions have the same magnitude but a different, randomly chosen direction.

We here outline the procedure followed to obtain the relaxation rate for BeH^+ . Starting with 10 fast ions with an initial velocity of 2200 ms^{-1} (see Table 4.1), and running the simulations 10 times, we obtain the histogram of velocities (averaged over one cycle of the rf trap potential) after 100 ms shown in Fig. 4.12. None of the simulated 100 fast ions have escaped or relaxed, and it is clear that both heating and cooling occurs. Running a similar set of 10 simulations, but this time with an initial velocity of 1200 ms^{-1} , we find that all 100 ions are sympathetically cooled and embedded within the Coulomb crystal after 100 ms.

We obtain an estimate of the average relaxation time of BeH⁺ by running similar sets of simulations for 2200, 2000, 1800, 1600, and 1200 ms⁻¹. From each set of simulations we collect the percentage of fast ions that decelerate during 100 ms to below the initial velocity of the next set of simulations. The results are shown in Table 4.2. Obviously, sympathetic cooling starts to become efficient at the 100-ms time scale for velocities below 1600 ms⁻¹. The percentages (see column 3 of Table 4.2) are treated as probabilities, which we denote as p_i , from which the time constant, α_i , of the 'decay' from speed category v_i to speed category v_{i+1} is calculated through $\alpha_i = -(100ms)^{-1} \ln(1 - p_i)$. Next, the coupled differential equations

$$\begin{aligned}
 N'_0(t) &= -\alpha_0 N_0(t) \\
 N'_1(t) &= -\alpha_1 N_1(t) + \alpha_0 N_0(t) \\
 N'_2(t) &= -\alpha_2 N_2(t) + \alpha_1 N_1(t) \\
 N'_3(t) &= -\alpha_3 N_3(t) + \alpha_2 N_2(t) \\
 N'_4(t) &= -\alpha_4 N_4(t) + \alpha_3 N_3(t)
 \end{aligned} \tag{4.25}$$

are solved, where N_i stands for the number of fast ions in the i^{th} velocity category. The category index i corresponds to the row of Table 4.2, *i.e.* $i=0$ for 2200 m/s and $i=4$ for 1200 m/s. We omit level $i=5$ for 0 m/s because a particle that reaches 1200 m/s certainly relaxes within tens of milliseconds. From the solutions of Eq. (4.25) we obtain an effective relaxation time for BeH⁺ of 1.5 s. The relaxation times for the products of reactions (1), (2) and (3) are too long to determine within reasonable computation time because of their higher initial velocities and smaller cooling efficiencies (due to the larger mass

Table 4.2: Summary of simulations performed to obtain the relaxation time of BeH⁺. The third column shows the percentage of ions having a speed lower than v_{i+1} after 100 ms simulated time. The fourth column shows the percentage of ions which relax (*i.e.* become fully embedded within the Coulomb crystal) within 100 ms.

v_i	v_{i+1}	percentage of ions ending at $v < v_{i+1}$ within 100 ms	percentage of ions that relaxes within 100 ms
2200	2000	14	0
2000	1800	25	0
1800	1600	35	6
1600	1200	80	60
1200	800	100	100

difference with Be^+). The same holds for the time it takes a for a fast ion to escape the trap. Histograms as in Fig. 4.12 are produced for the other species as well, but only for a few initial speeds. Since those histograms are fairly symmetric in shape (with respect to the initial velocity) we assume that the ratio of escaping and relaxing is approximately 50:50. The chemical products of reactions (4), (5) and (6) have relatively low velocities. They are found to relax within tens of milliseconds with zero probability of escaping from the trap. The MD simulations point out that their influence on the HD^+ z -velocity distribution is negligible.

Based on the results described above, we set $\alpha_{\text{relax,BeH}^+}$ at 0.67 s^{-1} . Concerning the relaxation and escape rates of the reactions (1)–(3), we consider two extreme scenarios:

- Scenario 1: A minimum number of fast ions is present in the trap. α_{relax} and α_{esc} are set to their maximum value of one per second for all species, which is based on the observation that no ion loss and since no relaxation are observed over simulated times up to 800 ms. This scenario will produce the smallest value of q .
- Scenario 2: A maximum number of fast ions is present in the trap, which means α_{relax} and α_{esc} are set to their minimum value of zero. All fast ions remain in the trap at high speed for the entire 10 seconds of REMPLD. This scenario leads to the largest value of q .

We assume that fast ions do not mutually interact when present in numbers of ten or less, so that the observations based on MD simulations with ten fast ions are also valid for smaller numbers of fast ions. Note that BeH^+ ions are already created during the first secular scan before the REMPLD phase starts. The fast specimen of the species of fast H_2D^+ and H_3^+ occur less frequently in the trap, and in line with the concept of extreme scenarios we assume zero H_2D^+ and H_3^+ for scenario 1, and 3 H_2D^+ and 1 H_3^+ for scenario 2. Together with scenarios a and b described in Sec. 4.4.2 this gives us four scenarios in total, and therefore four different spectral fit functions and four different ν_0 results.

For all possible combinations of fast ions present during REMPLD (*e.g.* 1 D^+ , 2 BeH^+ and 1 H_2D^+ or 3 D^+ , 3 BeH^+ and 3 H_2D^+) an MD simulation is carried out. From these simulations, the HD^+ z -velocity distribution is determined and a q -Gaussian is fitted which results in one q value for each simulated case. As mentioned before, the production rate of fast D^+ depends on the REMPLD rate (and thus on the 782 nm laser frequency ν), which itself depends on the time-dependent number of available HD^+ ions in the target state. To take this properly into account we introduce a time and frequency dependent parameter $q(t, \nu)$ as follows. For each of the four scenarios, the number of fast

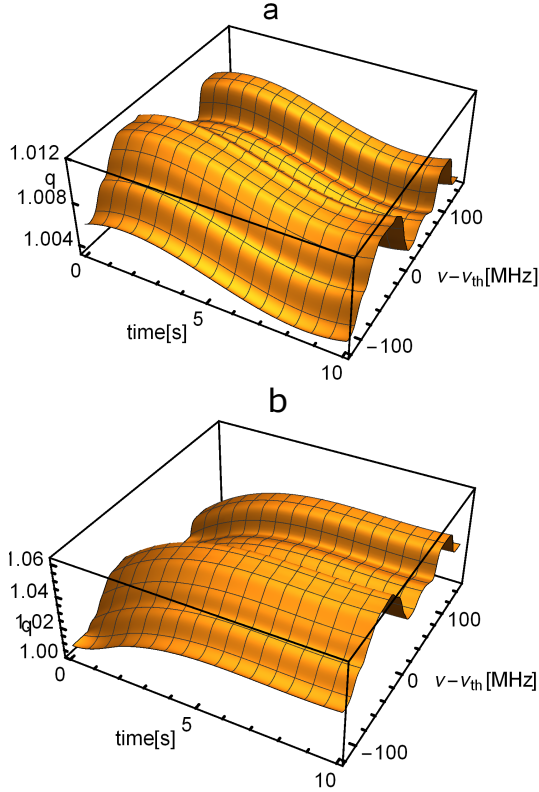


Figure 4.13: 3D $q(t, \nu)$ plots for scenario 1a (a) and 2b (b). Note that scenario 1a nearly corresponds to the case $q = 1$, *i.e.* the case in which all chemistry-induced effects can be ignored. See text for further details.

D⁺ is simulated on a grid of different REMPD durations, t_j , and of different frequencies, ν_j of the 782 nm laser. On each point of this two-dimensional grid, the number of fast D⁺ is combined with the number of other fast ions, and the corresponding value of $q(t_j, \nu_j)$ is looked up in a library of q values, obtained from many MD simulations performed with various combinations and abundances of fast ion species. Interpolation of the grid $q(t_j, \nu_j)$ leads to a smooth continuous function $q(t, \nu)$, which is subsequently inserted into the lineshape function D_z used in Eqs. (4.12) and (4.13). Figure 4.13 shows the 3D plots of $q(t, \nu)$ for the different scenarios.

Besides the q value, also the ion temperature T_{HD} is frequency and time dependent. Due to a larger number of D⁺ ions at the top of the spectrum than

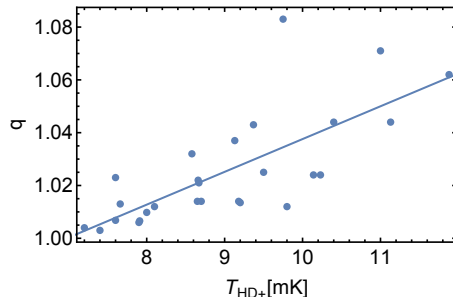


Figure 4.14: The relation between the temperature of a simulated Coulomb crystal and the q value. Each point represents a simulation of approximately 100 ms. The data are best fitted with a linear function (blue line).

at the wings, the temperature differences between top and wings can reach a few mK. We note that the increase of q and T_{HD} share the same origin (namely collisions with fast ions), and in Fig. 4.14 we show the relation between q and T_{HD^+} , obtained from fitting q -Gaussians to simulated velocity distributions. In scenario 1, the temperature difference between top and wings is found to be 0.5 mK. For scenario 2, the estimated temperature difference is 2.5(5) mK, where the uncertainty of 0.5 mK is treated as one standard deviation. The t and ν dependent temperature is also included in D_z .

4.4.5 Background gas reactions

During the REMPD phase the number of HD^+ is not only reduced through photodissociation by the lasers. As described in Sec. 4.4.4, trapped ions can react with H_2 molecules of the background gas in the vacuum setup. In order to correct the spectroscopic signal for these so-called background losses, the rates of reactions (2) and (3) in Table 4.1 are measured and included into the rate equations, Eq. (4.12), as an additional loss channel.

The spectral data were acquired over the course of several months during 15 independent measurement sessions lasting several hours each (Fig. 4.15). During this period the background pressure varied from session to session. For each session, the HD^+ background signal is obtained by using the measurement scheme depicted in Fig. 4.5, but with a shutter blocking the 782 nm laser, thus preventing REMPD. Typically, a few HD^+ ions react with H_2 which is detected as a small difference between the secular scan peak areas $A_{\text{bg},i}$ and $A_{\text{bg},f}$. During each measurement session, a background loss measurement is carried out approximately three times, providing a data set of about 20 background measurement per session. From the average background loss signal per session a

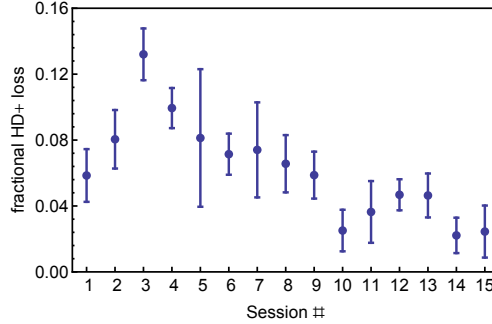


Figure 4.15: Signals corresponding to background gas losses per measurement session. During some sessions the background pressure of the vacuum was high, which results in a higher signal. The dots are the averages of a set of measurements, the error bars represent a $\pm 1\sigma$ standard deviation.

reaction rate γ_{bg} is extracted from the relation

$$1 - e^{-\gamma_{\text{bg}} t} = \frac{N_{\text{bg},i} - N_{\text{bg},f}}{N_{\text{bg},i}} = f_{\text{NL}}^{-1} \left(\bar{T}_0, \frac{A_{\text{bg},i} - A_{\text{bg},f}}{A_{\text{bg},i}} \right) \quad (4.26)$$

with $t = 10$ s and f_{NL}^{-1} mapping $(A_{\text{bg},i} - A_{\text{bg},f})/A_{\text{bg},i}$ onto $(N_{\text{bg},i} - N_{\text{bg},f})/N_{\text{bg},i}$ (see Appendix B). The values of γ_{bg} are inserted into a modified set of rate equations, which include the process of background loss reactions:

$$\frac{d\rho_{\text{bg}}(t)}{dt} = (M_{\text{rempd}} + M_{\text{BBR}} + M_{\text{bg}}) \rho_{\text{bg}}(t). \quad (4.27)$$

Here ρ_{bg} is ρ from Eq. (4.12) including two additional rows which describe the occurrence of ions in the form of H_2D^+ or H_3^+ . M_{bg} is a diagonal matrix containing γ_{bg} which describes the HD⁺ losses. We take into account the fact that conversion of HD⁺ to H_3^+ in reaction (3) in Table 4.1 is not detected by the method of detection through secular excitation because HD⁺ and H_3^+ have the same mass-to-charge ratio. This means that the measured values of γ_{bg} only represent the rates for reaction (2). As explained in Sec. 4.4.4, the reaction rate of (3) is a factor of three lower, which is taken into account.

We correct the data set of each session individually for the background signal following an iterative procedure. During the first step we insert an estimated \bar{T}_0 value in Eq. (4.26), and we simply subtract the signal predicted by the model without background losses (based on Eq. (4.12)) from the signal prediction including background losses (based on Eq. (4.27)). In this way an estimate of the background signal is obtained which is subsequently subtracted from the raw measurement data. Then the spectral fit function S_{fit} (see Sec. 4.4.1) is

fitted to the corrected data points with free fit parameters \bar{T}_0 , T_{HD^+} , I_{laser} and $\nu_{0,\text{fit}}$. The first three parameters are reinserted into equations 4.12 and 4.27 and after a few iterations, convergence is achieved.

Reactions (4) and (5) in Table 4.1 result in the production of H_3^+ during REMPD, which is falsely detected as extra HD^+ during the secular scans. To correct for these processes we insert correction factors in front of N_i and N_f (see Eq. (4.16)) based on the reaction rates of (4) and (5). From the rate equations corresponding to these reactions, a time-dependent multiplication factor which accounts for the excess signal due to H_3^+ , $R(t) \equiv 1 + N_{\text{H}_3^+}(t)/N_{\text{HD}^+}(t)$, can be derived, which modifies ϵ in the following way:

$$\epsilon' = \frac{N_f R(t_f) - N_i(R(t_i))}{N_f R(t_f)}, \quad (4.28)$$

where $t_i = 10$ s is the duration from the time of loading of HD^+ ($t_0 = 0$ s) until halfway the first secular scan, and $t_f = 26$ s is the duration between halfway the first and halfway the second secular scans (see Fig. 4.5). This results in a REMPD signal that is corrected by approximately 2% (with respect to the unmodified signal strength) due to the increased fraction of H_3^+ .

Another correction we include is the amount of HD^+ reacting with the background gas during the secular scans themselves (see reactions (2) and (3) in Table 4.1) and during tuning of the 313 nm laser directly before and after REMPD (see Fig 4.5). This yields the following modifications of N_i and N_f :

$$N_i \rightarrow N'_i(t_a, t_c) \equiv N_i e^{\gamma_2 t_a} e^{\gamma_3 t_c} \simeq N_i (1 + \gamma_2 t_a + \gamma_3 t_c) \quad (4.29)$$

$$N_f \rightarrow N'_f(t_b) \equiv N_f e^{-\gamma_2 t_b} \simeq N_f (1 - \gamma_2 t_b), \quad (4.30)$$

where γ_2 ($= \gamma_{bg}$) and γ_3 are the rates of reactions (2) and (3), respectively. The last step in both equations is justified given the slow rate constants (about $1/500$ s $^{-1}$ or slower, see Table 4.1) compared to the secular scan duration (10 s), thus $\gamma_2 t_a \ll 1$, $\gamma_2 t_b \ll 1$ and $\gamma_3 t_c \ll 1$. Note the positive signs in the exponents of Eq. (4.29), which correspond to a measured N'_i larger than the number of trapped HD^+ ions during REMPD.

The choices for t_a , t_b and t_c are made as follows: we assume that reaction (3) does not affect the secular scan fluorescence signals because the change of charge-to-mass ratio of the ion is negligible in this case. Therefore, t_c is the full period between creation of HD^+ and REMPD, *i.e.* $t_c = 18$ s (see Fig. 4.5). After REMPD, there is no need to distinguish between HD^+ and H_3^+ , and therefore t_c is absent in Eq. (4.30).

Concerning reaction (2), HD^+ losses at the beginning of a secular scan result in lower integrated fluorescence signals than losses at the end of a secular scan. In our analysis, we use the average time (mean value) of the distribution

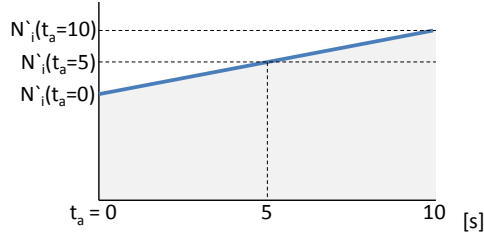


Figure 4.16: $N'_i(t_a) = 1 + \gamma_2 t_a$ is represented by the blue line (in this example we can ignore the $\gamma_3 t_c$ term which is in fact a constant factor). The average of N'_i is its integrated value (grey area) divided by the secular scan duration of 10 seconds. This is equal to $N'_i(t_a = 5)$.

of ‘early’ and ‘late’ losses via this channel of $t_a = 5$, in order to obtain the time averaged value of N'_i in the secular scan period (see Fig 4.16). After the first secular scan, and before REMPLD, three seconds are required for laser frequency tuning (see Fig. 4.5), giving us a total of duration $t_a = 8$ s to insert in Eq. (4.29). Analogously, in case of N'_f , related to the second secular scan and second 313 nm laser tuning, we obtain $t_b = 8$ s.

Expressed numerically, for the loss rates in our experiment, the modifications are:

$$N_i \rightarrow 1.06N_i \quad (4.31)$$

$$N_f \rightarrow 0.97N_f \quad (4.32)$$

4.4.6 Spectrum, systematic effects and final result

The function S_{fit} is fitted to the REMPLD data set after correction for the background signal. Figure 4.17 shows the REMPLD data set and fit function for scenario 1a. The noise in the spectrum has several origins. Firstly, the number of trapped ions is relatively small and varies from shot to shot. Secondly, the population in the various hyperfine states of the $L=2$ state varies from shot to shot, as expected for hyperfine states with a mean occupancy of order unity. The (stochastic) BBR interaction, which couples the states with $L = 2$ with other rotational states, adds another factor of noise. Furthermore, the variation of the number of reactions of HD⁺ with the background gas is in the order of a few per shot, which dominates the noise for low REMPLD signals. Finally, part of the noise originates from intensity variations due to spatial alignment variations of the 313 nm, 782 nm and 532 nm lasers.

For each of the four scenarios we obtain a particular set of fit parameters, which are listed in Table 4.3. The correlation coefficients of the fit parameters

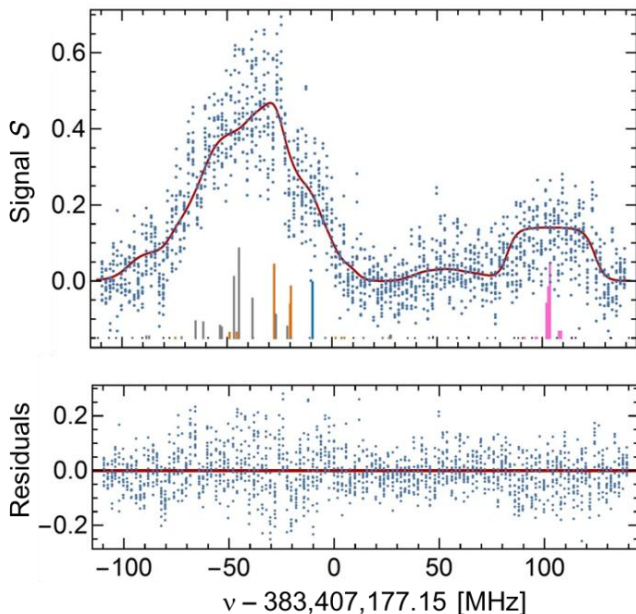


Figure 4.17: Upper panel: Measured spectrum (dots), least-squares fit (solid curve); lower panel: fit residuals. All 1772 data points are plotted together with the fit function corresponding to scenario 1a. The fitted functions corresponding to the different scenarios are visually indistinguishable from the result shown here. The colored sticks represent the theoretical lines at represent the positions and linestrengths of the individual hyperfine components, shown schematically in Fig. 4.4b

are presented in Table 4.4 and the values for $\nu_{0,\text{fit}} - \nu_{\text{th}}$ are graphically shown in Fig. 4.18. The error bars represent the 1σ statistical fit uncertainty which can be considered as the precision of the spectroscopy measurement. We remark that the sensitivity to the chemistry processes (scenario 1 and 2) is much stronger than the sensitivity to the numbers of HD^+ ions in the trap (scenario a and b). We note that the values $\nu_{0,\text{fit}}$ for 1a and 2a represent extreme upper and lower limits (with respect to the line shift due to chemistry) for the average number of HD^+ ions. We therefore chose to obtain our final result for $\nu_{0,\text{fit}}$ by taking the mean of these two values, while interpreting the mean single-fit error of (which is virtually the same for all four results) as the statistical uncertainty of the final result. We subsequently quantify the 'which-scenario' uncertainty as follows. For scenarios 1a and 1b (and similarly for 2a and 2b) the difference is due to a 1σ variation in the number of HD^+ ions. Therefore, we treat

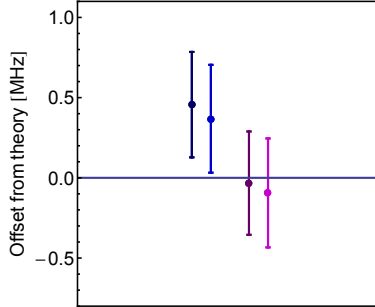


Figure 4.18: Values of $\nu_{0,\text{fit}} - \nu_{\text{th}}$ found for the four different scenarios 1a, 1b, 2a and 2b. Error bars indicate the 1σ fit uncertainty. All values are plotted with respect to the theoretical frequency (blue horizontal line) [2].

the frequency interval between the two values corresponding to scenario a and b as the corresponding 1σ interval, which amounts to 80 kHz when averaged over the two scenarios 1 and 2. To find the error corresponding to scenarios 1 and 2, we take frequency interval between the values found for scenarios 1a and 2a (which are essentially extreme limits) and conservatively equate the interval to a 68 % confidence interval. The interval thus corresponds to 2σ , with $\sigma = 0.23$ MHz. The uncertainty of 0.5 mK in the temperature difference between top and wings of the spectrum (see Sec. 4.4.4) results in 0.028 MHz difference in $\nu_{0,\text{fit}}$, which is treated as 1σ variation. The frequency shifts due to these systematic effects together with their uncertainties are listed in Table 4.5.

Table 4.3: The fit results of the free fit parameters per scenario. Scenario 1 and 2 give a clear difference in $\nu_{0,\text{fit}}$ results. Scenario a and b give different results for \bar{T}_0 . This can be explained by the different amount of trapped molecular species, which result in different Be^+ temperatures during a secular scan.

fit parameter	Scenario			
	1a	1b	2a	2b
$\nu_{0,\text{fit}} - \nu_{\text{th}}(\text{MHz})$	0.46(33)	0.37(34)	-0.03(32)	-0.12(33)
$T_{\text{HD}^+}(\text{mK})$	10.9(8)	11.0(8)	10.6(8)	10.35(80)
$I_{\text{laser}} (\times 10^7 \text{ Wm}^{-2})$	0.99(14)	1.04(15)	0.95(14)	0.98(15)
$\bar{T}_0(\text{K})$	2.79(3)	3.85(5)	2.82(5)	3.84(5)

Frequency uncertainty of the 782 nm laser

The beat note of the frequency-locked 782 nm laser with the optical frequency comb is counted during REMPD. We use the beat-note frequencies to compute the Allan deviation, which is of the order of 0.1 MHz after 10 s averaging. The uncertainty of the 782 nm laser frequency can be transferred to an uncertainty in the $(0,2) \rightarrow (8,3)$ fit result $\nu_{0,\text{fit}}$ by taking the Allan deviation as a measure of the standard deviation of a Gaussian noise distribution, describing the laser frequency offset from the set frequency during each REMPD cycle. We perform a Monte Carlo simulation in which each of the 140 measurement frequencies is assigned a frequency offset, selected at random from the Gaussian distribution. Repeating this 100 times generates 100 different spectral data sets. Fitting S_{fit} to each of the data sets gives 100 different values of $\nu_{0,\text{fit}}$. A histogram of the resulting distribution of $\nu_{0,\text{fit}}$ values is shown in Fig. 4.19, where the x -axis denotes the difference between $\nu_{0,\text{fit}}$ and the fit value of scenario 1a, $\nu_{0,\text{fit},s1a}$. The mean and standard deviation of this list of fit values are 0.5 kHz and 8 kHz, respectively. Based on these simulations we set the frequency uncertainty due to the frequency lock at 0.01 MHz.

The 782 nm laser has a Gaussian linewidth of ~ 0.5 MHz. The convolution of this lineshape with the (Gaussian) Doppler-broadened line (16 MHz) will give rise to another Gaussian lineshape. Since the linewidths add up quadratically, the increase in linewidth is smaller than the uncertainty of the linewidth due to the fit uncertainty of the temperatures, which is ~ 0.8 mK. Therefore, we consider the laser linewidth to be completely absorbed into the fitted temperature T_{HD^+} with no significant effect on its value.

Zeeman and Stark and other shifts

So far we have neglected the Zeeman splitting of the lines in the spectrum. Incorporating the Zeeman effect makes the hyperfine transition matrices very large and MATHEMATICA is only able to solve the rate equations [Eq. (4.12)] effectively if lineshapes are not too complicated. We circumvent these issues as

Table 4.4: The correlation coefficients for the fit of scenario 1a to the data.

	$\nu_{0,\text{fit}} - \nu_{\text{th}}$	T_{HD^+}	I_{laser}	T_0
$\nu_{0,\text{fit}} - \nu_{\text{th}}$	1	-0.609	0.483	0.049
T_{HD^+}	-0.609	1	-0.690	0.038
I_{laser}	0.483	-0.690	1	0.579
T_0	0.049	0.038	0.579	1

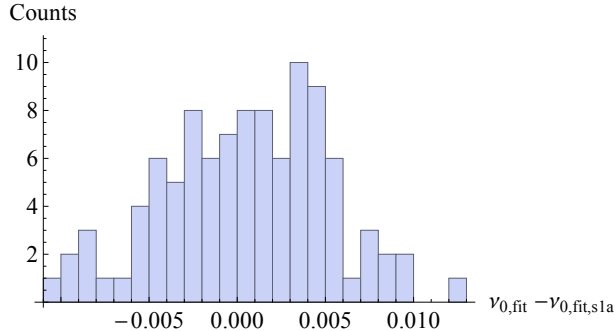


Figure 4.19: Variation of spectroscopic $(0,2) \rightarrow (8,3)$ results due to the 782 nm laser linewidth based on 100 Monte Carlo simulations. The $\nu_{0,\text{fit}} - \nu_{0,\text{fit},s1a}$ values are plotted in a histogram where $\nu_{0,\text{fit},s1a}$ is the $\nu_{0,\text{fit}}$ result of scenario 1a.

follows. First, we calculate the lineshifts and linestrengths of the magnetic sub-components of individual hyperfine lines. This is done by diagonalizing the sum of the hyperfine and Zeeman Hamiltonians, after which the eigenvectors and energy values are used to compute the stick spectrum of the $(v,L):(0,2) \rightarrow (8,3)$ transition. This procedure is similar to that followed in Refs. [63, 125]. As the Zeeman splitting is small compared to the Doppler width, the magnetic sub-components belonging to the same hyperfine component overlap well within the profile of the lineshape function D_z , forming a new composite (and Zeeman-shifted) lineshape function D'_z . This new lineshape function is subsequently used in Eq. (4.13). For simplicity, we do not implement effects of micromotion and chemistry in this analysis, and we compare $\nu_{0,\text{fit}}$ fit results based on versions with $B=0.19$ mT with a version with zero B field. It is important to note that during the $(0,2) \rightarrow (8,3)$ excitation only σ^+ and σ^- transitions are driven as the 782 nm laser and B-field directions are parallel. The practically linear polarization of the laser can be decomposed into two circularly polarized components with an estimated maximum intensity imbalance of 2%. Figure 4.20 shows the $\nu_{0,\text{fit}}$ fit results of several σ^+/σ^- ratios with respect to a fit performed for the case of zero magnetic field. For the 0.19 mT field in our experiment, a shift of $-0.017(3)$ MHz is obtained, with the uncertainty due to the possible polarization imbalance.

The ac Stark shifts due to the 782 nm, 532 nm and 313 nm lasers are -869 Hz, -452 Hz and 8 Hz respectively. These values represent the shift of the center of gravity of the spectral line and thus can be considered as weighted means of all the shifts of the single hyperfine components. The calculations of the Stark shifts are shortly explained in Appendix D. Stark shifts due to the BBR and trap rf field are calculated in [111] and are smaller than 1 Hz.

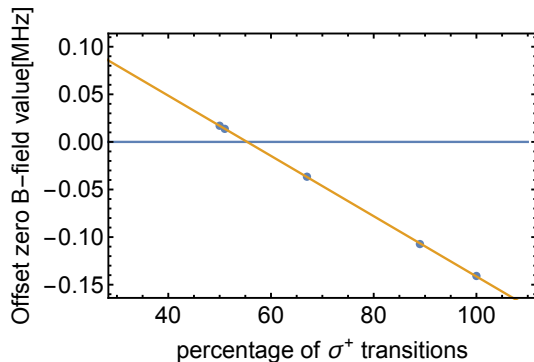


Figure 4.20: Zeeman shift of $\nu_{0,\text{fit}}$ found with a spectral fit function including the Zeeman effect due to a 0.19 mT magnetic field, for different ratios of σ^+/σ^- transitions. The horizontal line at 0 MHz corresponds to the value obtained using a fit function assuming zero magnetic field.

Together, this gives us a total Stark shift of 1.3(1) kHz. The uncertainty in this value stems almost exclusively from the accuracy to which the laser beam intensities are known.

A conservative upper limit of 100 Hz to the electric-quadrupole shift for the $(v,L):(0,2)\rightarrow(8,3)$ transition is obtained from [16]. The 2nd order Doppler effect is calculated from the average micromotion velocity of the HD⁺ ions, and is found to be less than 5 Hz. The values of the mentioned shifts and their uncertainties are listed in Table 4.5.

If we compare $\nu_{0,\text{fit}}$ from scenario 1a based on the model containing rotational states $L \leq 5$ with a version containing $L \leq 6$ states we find a shift of $\nu_{0,\text{fit}}$ of 28 kHz which we use as uncertainty due to the neglect of population in $L = 6$. By comparing the $\nu_{0,\text{fit}}$ value from scenario 1a that includes micromotion with a the result of a version with zero micromotion, a shift of 0.055(20) MHz is obtained. The estimated uncertainty of the BBR temperature is about 5 K, and caused by day-to-day variations of the temperature in the laboratory, and to a possible elevated temperature of the trap electrodes due to rf current dissipation. If we compare the $\nu_{0,\text{fit}}$ values after inserting BBR temperature of 300 K and 305 K, we obtain a difference of 5 kHz. The uncertainty of spin coefficient E_4 (see Eq. (4.1)), which is estimated at a value of 50 kHz [109] has an effect of ~ 1 Hz on the ν_0 result.

Table 4.5: Systematic shifts and uncertainty budget.

Origin	Shift (MHz)	Uncertainty	
		(MHz)	(ppb)
Resolution (statistical fit error)	0	0.33	0.85
Uncertainty q value	-0.25 ¹	0.23	0.61
Uncertainty N_{HD^+}	0	0.080	0.21
Ignoring population $L=6$ in rate equations	0	0.032	0.083
T_{HD^+} variation in spectrum	0	0.028	0.072
Doppler effect due to micromotion	-0.055 ¹	0.020	0.052
Frequency measurement	0	0.010	0.026
BBR temperature	0	0.005	0.013
Zeeman effect	-0.0169	0.003	0.008
Stark effect	-0.0013	0.0001	0.0004
Electric-quadrupole shift	0 ²	0.0001	0.0003
2 nd order Doppler effect	0 ²	0.000005	0.00001
Uncertainty E_4	0 ²	0.000001	0.000003
Total	-0.0182	0.41	1.1

¹ This is a shift with respect to a scenario with a zero effect of q or micromotion, and serve to illustrate the size of the effect. The shift itself, however, is absorbed in the value of $\nu_{0,\text{fit}}$.

² The value of these shifts is actually nonzero but negligibly small, and therefore ignored here.

Result of ν_0

We take average of the fit values obtained from scenarios 1a and 2a as the $(v,L):(0,2)\rightarrow(8,3)$ frequency result, which yields 383,407,177.38 MHz. Table 4.5 shows the error budget, with a total uncertainty of 0.41 MHz that corresponds to 1.1 ppb. This result differs 0.21 MHz (0.6 ppb) from the more accurate theoretical value of the $(v,L):(0,2)\rightarrow(8,3)$ frequency, $\nu_{\text{th}} = 383,407,177.150(15)$ MHz [2]. The two main uncertainty contributions are the statistical fit error of 0.33 MHz and the uncertainty in the q -factor scenario of 0.23 MHz.

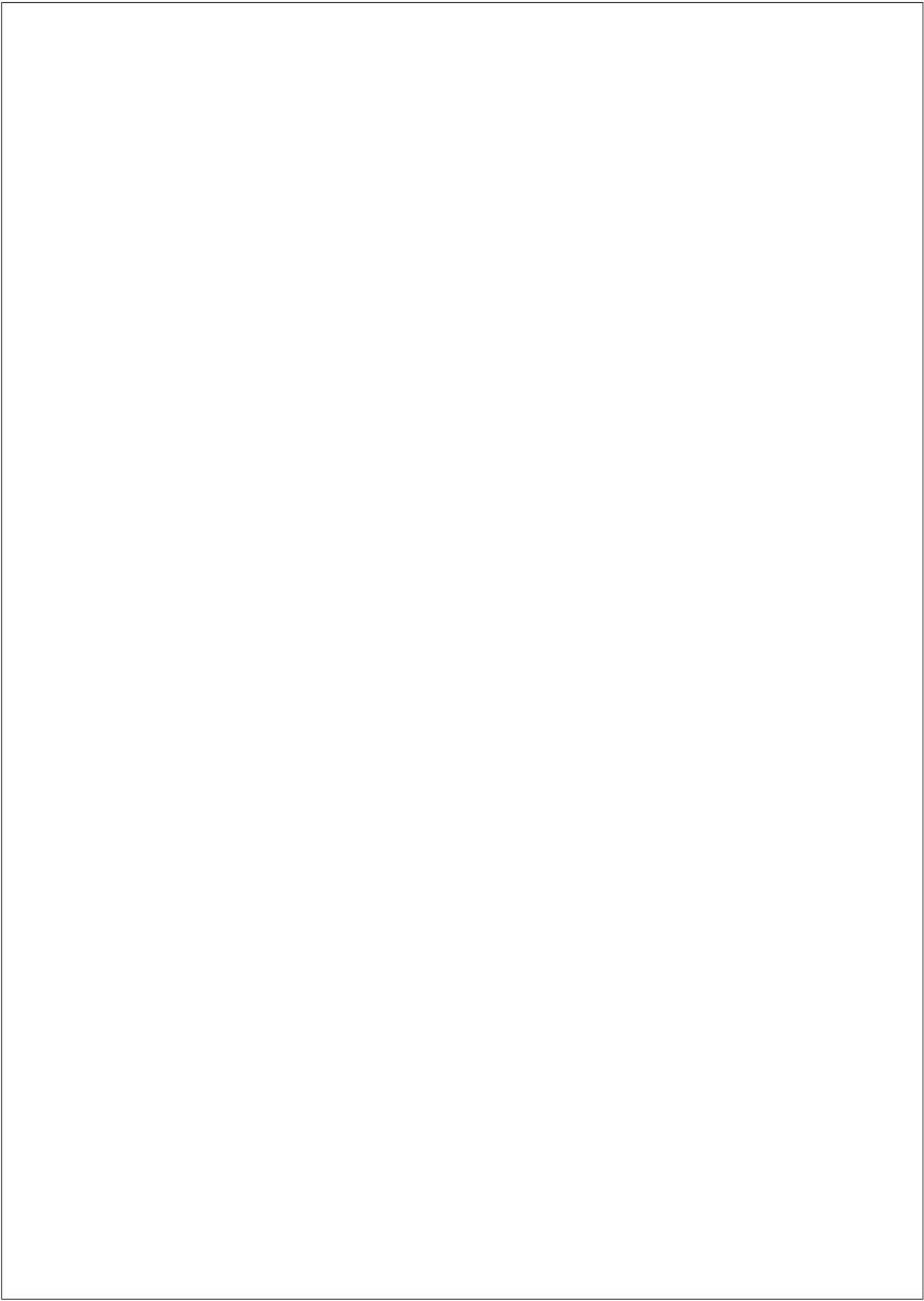
4.5 Conclusion

We have measured the $(v,L):(0,2)\rightarrow(8,3)$ transition in the HD⁺ molecule with 0.85 p.p.b (0.33 MHz) precision, which is the first sub-p.p.b. resolution achieved in molecular spectroscopy. The result differs by only 0.6 p.p.b. from the theoretically predicted value, and a thorough analysis of systematic effects

points out that the total uncertainty is 1.1 p.p.b. A large contribution to the systematics is the effect of chemical reactions in the Coulomb crystal, of which the 1σ uncertainty is 0.61 p.p.b (0.23 MHz). This effect, which had not been recognized before, causes a nonthermal velocity distribution that can be approximated by a q -Gaussian function, and which significantly influences the final value of ν_0 .

The agreement between experimental and theoretical data allows us to put new bounds on the existence of hypothetical fifth forces, and put new limits on the compactification radius of higher dimensions, which is explained in [69, 72, 76]. Furthermore, for the first time, a new value the proton-to-electron mass ratio based on molecular spectroscopy can be found [76].

Our analysis clearly demonstrates that the first-order Doppler effect is responsible for the largest contribution to the uncertainty. In fact, a measurement that is first-order Doppler-free can improve the precision by a factor of 100 to 1000. In [126] an experiment was proposed in which the $(v, L) = (0, 3) \rightarrow (9, 3)$ line in HD^+ is addressed through a two-photon transition with nearly degenerate photons. Using counter-propagating laser beams with a narrow linewidth, the Lamb-Dicke regime may be reached in which first-order Doppler broadening is virtually eliminated.



Probing QED and fundamental constants through laser spectroscopy of vibrational transitions in HD^+

The simplest molecules in nature, molecular hydrogen ions in the form of H_2^+ and HD^+ , provide an important benchmark system for tests of quantum electrodynamics in complex forms of matter. Here, we report on such a test based on a frequency measurement of a vibrational overtone transition in HD^+ by laser spectroscopy. We find that the theoretical and experimental frequencies are equal to within 0.6(1.1) parts per billion, which represents the most stringent test of molecular theory so far. Our measurement not only confirms the validity of high-order quantum electrodynamics in molecules, but also enables the long predicted determination of the proton-to-electron mass ratio from a molecular system, as well as improved constraints on hypothetical fifth forces and compactified higher dimensions at the molecular scale. With the perspective of comparisons between theory and experiment at the 0.01 part-per-billion level, our work demonstrates the potential of molecular hydrogen ions as a probe of fundamental physical constants and laws.

5.1 Introduction

The possibility of accurate quantum electrodynamics (QED) calculations and the presence of narrow optical transitions between long-lived vibrational levels make laser spectroscopy of H_2^+ and HD^+ a sensitive tool to test fundamental physics at the molecular scale. Examples include tests of relativistic quantum mechanics and QED [1, 2, 57, 64], and searches for physics beyond the Standard Model at the molecular scale [69, 72] and beyond General Relativity [15, 46]. Furthermore, spectroscopy of the molecular hydrogen ion has long been proposed as a means to determine the value of fundamental physical constants [1, 2, 57, 126], and to realise precise molecular clocks [14, 15].

Nearly all the above applications involve a comparison of state-of-the-art molecular theory with accurate results from (most often laser) spectroscopy. The most accurate results so far have been obtained using HD^+ ions stored in radiofrequency (r.f.) traps, sympathetically cooled by laser-cooled Be^+ ions [63, 64], allowing tests at a relative uncertainty of a few parts per billion (p.p.b.) However, the most precise experimental result [64], a frequency measurement of the $(v, L):(0,0) \rightarrow (1,1)$ rovibrational line at $5.1 \mu\text{m}$ in HD^+ with a relative uncertainty of 1.1 p.p.b., was found to disagree by 2.7 p.p.b. with a more accurate theoretical value obtained from state-of-the-art ab initio molecular theory [1, 2]. This disagreement has thus far been unresolved, and additional high-precision experimental data are needed to draw conclusions about the validity of the theoretical framework, and to open up the wide range of applications of molecular hydrogen ion spectroscopy mentioned above.

Here, we report on an optical frequency measurement of the $(v, L):(0,2) \rightarrow (8,3)$ vibrational overtone transition in HD^+ at 782 nm. Our experimental result is found to be in agreement with the theoretical prediction to within 0.6(1.1) p.p.b., thereby confirming the validity of relativistic quantum mechanics and QED in a vibrating molecular system at an unprecedented level. We subsequently exploit the agreement between theory and experiment for the first determination of the proton-electron mass ratio from a molecular system, and to put tighter constraints on the strength and range of fifth forces at the molecular scale.

5.2 Results

5.2.1 Experimental Procedure

Our experimental apparatus and procedure for HD^+ spectroscopy are described in detail in Sec. 5.3. In brief, trapped HD^+ molecular ions are cooled to ~ 10 mK by storing them together with laser-cooled Be^+ ions, and we excite and detect the $(v, L):(0,2) \rightarrow (8,3)$ transition by resonance-enhanced $(1+1')$ multipho-

ton dissociation (REMPD) spectroscopy, see Fig. 5.1a. We acquire a spectrum by observing the loss of HD^+ due to REMPD, inferred from the change in the monitored Be^+ fluorescence induced by r.f. excitation of the HD^+ secular motion, for different values of the 782 nm spectroscopy laser frequency (Sec. 5.3 and Fig. 5.2a). The latter is stabilized and counted using an optical frequency comb laser (Sec. 5.3).

5.2.2 Line shape model for nonlinear least-squares fitting

Hyperfine interactions lead to a manifold of 83 lines (Figs. 1b,c), the ~ 25 strongest of which are located within the range (-110 MHz, 140 MHz) around the hyperfine-less rovibrational frequency, ν_0 . Each hyperfine component is Doppler broadened to ~ 16 MHz, and the hyperfine structure is only partially resolved. Using a realistic spectral line shape function (Sec. 5.3), we employ nonlinear least squares fitting to extract not only the transition frequency, $\nu_{0,\text{fit}}$, but also the intensity of the 782 nm laser, I_{laser} , the motional temperature of the HD^+ ions, T_{HD^+} , and the temperature of the Be^+ ions during secular excitation, \bar{T}_0 , which are relevant parameters for the spectral analysis (see Sec. 5.3). The 782 nm intensity we find agrees (within the fit error) with the intensity estimated from the laser beam waist and beam alignment uncertainty. Likewise, the fitted temperature agrees well with the results of molecular dynamics (MD) simulations.

The relevance of the additional fit parameters is illustrated by the correlation matrix, Ω , of the estimated parameters, which reveals significant correlations between $\nu_{0,\text{fit}}$ and T_{HD^+} , and $\nu_{0,\text{fit}}$ and I_{laser} (Fig. 5.2c). Adding fit parameters results in an increased error in the fitted value $\nu_{0,\text{fit}}$ which rises from 0.25 MHz (0.65 p.p.b. relative to $\nu_{0,\text{fit}}$) to 0.33 MHz (0.85 p.p.b.) when \bar{T}_0 , T_{HD^+} , and I_{laser} are added as free fit parameters. Even so, the spectral fit result presented here marks the first time that a sub-p.p.b. resolution is achieved in molecular-ion spectroscopy.

5.2.3 Systematic effects and frequency value

The fit result $\nu_{0,\text{fit}}$ is corrected for various systematic frequency offsets due to electric and magnetic fields. We calculate the a.c. and d.c. Stark effect *ab initio* with high accuracy following the approach of Karr [14] to find the frequency shift due blackbody radiation, the r.f. trap field, and the electric fields of the lasers (see also Appendix D). The total Stark shift of $-1.3(1)$ kHz is dominated by the shifts due to the 313 nm, 532 nm and 782 nm lasers (which are all on during excitation), with individual contributions of $0.008(1)$ kHz, $-0.45(7)$ kHz, and $-0.87(13)$ kHz, respectively. Here, the uncertainties of the laser beam intensities are the dominant source of frequency uncertainty. We

5. PROBING QED AND FUNDAMENTAL CONSTANTS THROUGH LASER SPECTROSCOPY OF VIBRATIONAL TRANSITIONS IN HD^+

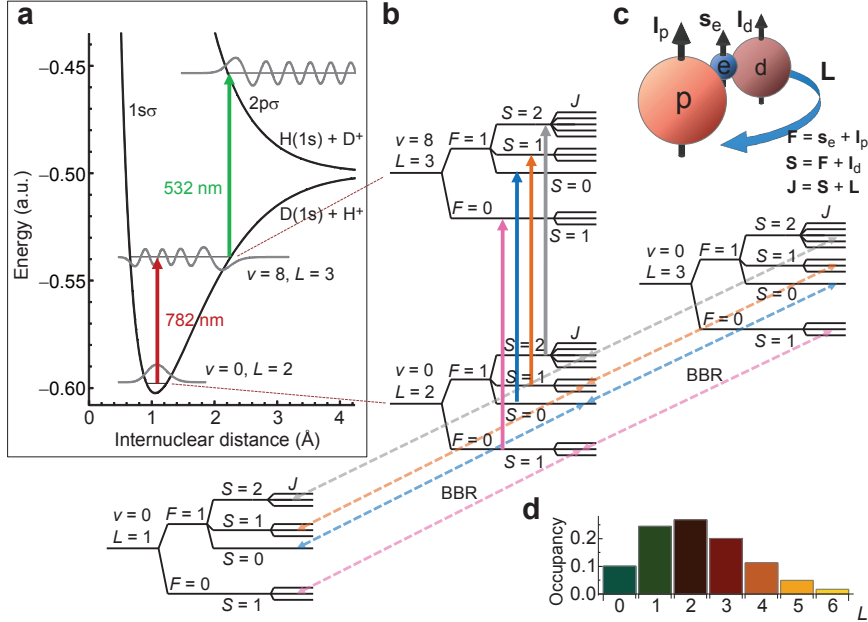


Figure 5.1: Partial level diagram, excitation scheme and interaction with blackbody radiation. The $(v,L):(0,2)\rightarrow(8,3)$ rovibrational transition is excited and detected through REMPD by 782 nm and 532 nm laser radiation (a, solid arrows), which leads to the loss of HD^+ by dissociation into either the $\text{H}(1s) + \text{D}^+$ or the $\text{D}(1s) + \text{H}^+$ channel [115]. Magnetic interactions between the proton spin I_p , deuteron spin, I_d , electron spin, s_e , and molecular rotation, L , lead to hyperfine structure in the excitation spectrum (b, c). Blackbody radiation induces rotational transitions (b, dashed arrows) between $v=0, L=2$ and states with $L=1,3$ which are in turn coupled to $L=0,4$ (not shown), and the population in each hyperfine state depends on the balance between the REMPD rate and the rate at which BBR replenishes population. These effects are included in a hyperfine rate equation model which is used to obtain a realistic spectral line shape function. Treating this at the level of individual hyperfine states naturally subdivides the HD^+ population into different spin configuration classes, which are only weakly coupled by the electric dipole transitions induced by the lasers and BBR, and therefore evolve independently during REMPD. d, Rotational distribution of HD^+ ($v=0$) at an ambient BBR temperature of 300 K. The population of the $v=0, L=2$ initial state amounts to 27%.

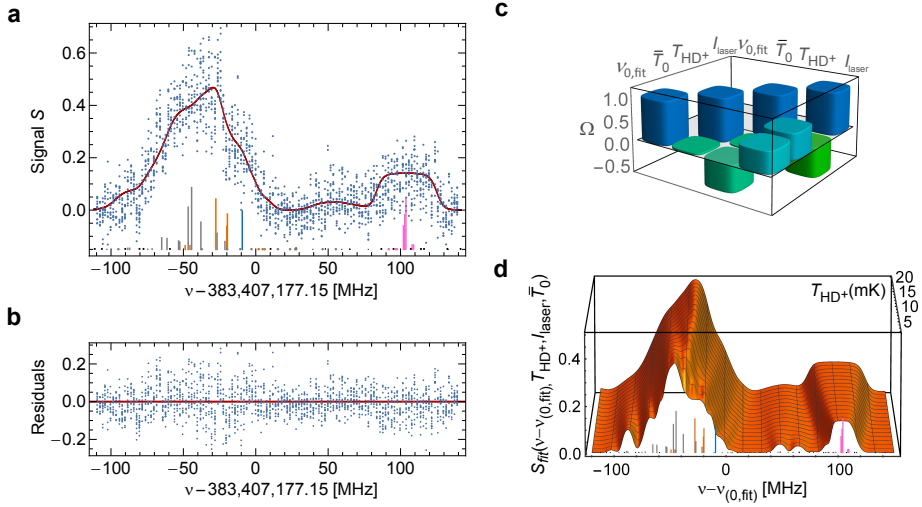


Figure 5.2: Spectral line shape function and fit to REMPD spectrum. a, Measured dimensionless REMPD signal S versus 782 nm laser frequency (blue dots) and fitted line shape function (red curve). The underlying individual hyperfine components are also shown, following the same colour coding as used in Fig. 5.2b. The hyperfine components are offset vertically for clarity. b, Fit residuals versus 782 nm laser frequency (blue dots). c, The correlation matrix, Ω , reveals correlations between $\nu_{0,\text{fit}}$ and the other fitted parameters, and the uncertainty in the fitted value $\nu_{0,\text{fit}}$ rises from 0.25 MHz (0.65 p.p.b. relative to $\nu_{0,\text{fit}}$) to 0.33 MHz (0.85 p.p.b.) when \bar{T}_0 , \bar{T}_{HD^+} , and I_{laser} are added as free fit parameters. d, Dimensionless spectral line shape function S_{fit} obtained with the rate equation model (Sec. 5.3) assuming $I_{\text{laser}} = 1 \times 10^7 \text{ Wm}^{-2}$ and $\bar{T}_0 = 4 \text{ K}$, showing the non-trivial combined effect of Doppler broadening, line overlap and saturation versus HD⁺ temperature (axis shown in perspective).

5. PROBING QED AND FUNDAMENTAL CONSTANTS THROUGH LASER SPECTROSCOPY OF VIBRATIONAL TRANSITIONS IN HD⁺

also evaluate the Zeeman effect, which stems from the static quantization field of 0.19 mT directed along the z -axis of the trap (Sec. 5.3). The polarization of the 782 nm laser is such that it induces σ^- and σ^+ transitions at equal rates. The Zeeman effect leads to a shift to $\nu_{0,\text{fit}}$ by $-16.9(3.2)$ kHz, the uncertainty of which is due to a possible 2% imbalance between the σ^- and σ^+ rates caused by imperfect polarization optics and depolarization due to the windows of the vacuum chamber. Another uncertainty stems from the accuracy of the theoretical hyperfine structure [109], which enters through our spectral line shape function. We repeated the fit procedure with a spectral line shape function based on the hyperfine structure obtained with slightly altered spin coefficients (within their uncertainty range), for which we observe essentially no shift of $\nu_{0,\text{fit}}$. Compared to the 0.33 MHz statistical fit uncertainty of $\nu_{0,\text{fit}}$, the contribution of the above line shifts to the total frequency value and uncertainty is negligible, as are the frequency shifts due to the second-order Doppler effect [87] (<5 Hz) and the electric-quadrupole shift [16] (<0.1 kHz).

During REMPD, the motional dynamics in the laser-cooled Coulomb crystal are significantly influenced by several (laser-induced) chemical processes. For example, REMPD of an HD⁺ ion leads to the formation of energetic fragments, and previously it was observed that the two reactions



and



occur with about equal probability (here k.e. stands for kinetic energy, and ν_1 and ν_2 for the frequencies of the 782 nm and 532 nm lasers, respectively) [115]. Due to their relatively high charge-to-mass ratio, the produced protons are not stably trapped in our apparatus. Indeed, we observe only cold, trapped deuterons after REMPD, indicating that each deuteron transferred most of its 0.41 eV kinetic energy to the ions in the Coulomb crystal (which itself contains only 2 meV of thermal energy at 10 mK), causing (at least transiently) significant heating of the crystal. Other reactions with energetic ionic products are the result of collisions with H₂ molecules in the background vapour, and we also take the reactions $\text{Be}^+(^2\text{P}_{3/2}) + \text{H}_2 \rightarrow \text{BeH}^+ + \text{H}(1s) + \text{k.e.}$, $\text{HD}^+ + \text{H}_2 \rightarrow \text{H}_2\text{D}^+ + \text{H}(1s) + \text{k.e.}$, and $\text{HD}^+ + \text{H}_2 \rightarrow \text{H}_3^+ + \text{D}(1s) + \text{k.e.}$ (with ionic product kinetic energies of 0.25, 0.36, and 0.66 eV, respectively) into account here. We determine reaction rates from measured loss rates of Be⁺ and HD⁺, which are in agreement with expected Langevin reaction rates given the pressure of 1×10^{-8} Pa in our vacuum apparatus [120]. We include these processes in realistic MD simulations (Sec. 5.3) employing leapfrog integration with an adaptive time step, to ensure that collisions between energetic ions are correctly handled. Under these conditions, our MD simulations reveal

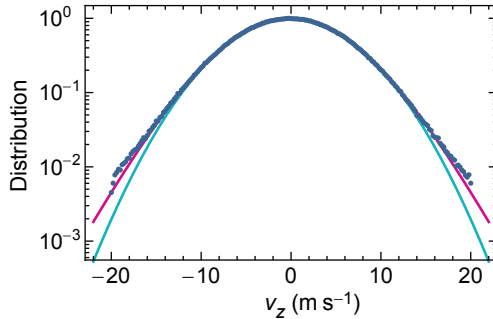


Figure 5.3: Non-thermal velocity distributions. When kinematic effects of (laser-induced) chemistry are included in MD simulations, the HD^+ z -velocity distribution exhibits non-thermal distributions with pronounced tails (blue data points). Indeed, a least-squares fit with a q -Gaussian (magenta curve, with fitted temperature $T=11.00(3)$ mK and $q = 1.070(3)$) produces a visibly better result than a fit with a thermal (normal) distribution (turquoise curve, fit with $T= 11.60(3)$ mK)

average HD^+ z -velocity distributions which deviate significantly from thermal (Gaussian) distributions, an effect which has hitherto been neglected by the widespread assumption that laser-cooled ion ensembles exhibit thermal velocity distributions. As shown in Fig. 5.3, we empirically find that the velocity distributions are better represented by q -Gaussians [122], which have the additional advantage that the effect of a given chemical reaction can be parameterized by a corresponding q -value (with $q=1$ corresponding to a Gaussian distribution). Taking all reactions and reaction rates into account, we find that the velocity distribution is best characterized by a q -Gaussian with q ranging between 1.00 and 1.07, depending on the assumed thermalisation rate and the REMPD rate. We therefore include q -Gaussians in our spectral line shape function (Sec. 5.3). Comparing scenarios with minimum and maximum expected thermalisation rates (corresponding to $q=1.07$ and $q=1.00$, respectively) we find a mean shift of $-0.25(25)$ MHz with respect to the case of $q=1.00$. The origin of this shift lies in the overlap and saturation of Doppler-broadened hyperfine components in the spectrum (Fig. 5.2d). A similar frequency shift may occur when micromotion sidebands are present. Here we make a distinction between excess radial micromotion caused by radial static offset fields, and axial micromotion which could arise from an axial r.f. field due to geometrical imperfections of our

ion trap. A finite-element analysis of the trap's electric field reveals that such an axial field will be approximately constant over the extent of the Coulomb crystal, which implies that the corresponding micromotion contribution to the line shape will be homogeneous. We use the fluorescence correlation method of Berkeland *et al.* [87] to find a small micromotion amplitude of 11(4) nm amplitude along the 782 nm laser beam as follows. Measurements of the r.f. field amplitude are performed on the Be^+ ions using the 313 nm laser beam (which co-propagates with the 782 nm laser beam). Repeating such measurements for various values of the trap r.f. voltage allows separating the axial and the radial component (the latter being due to the residual projection of the laser beam onto the radial direction). We find that the axial micromotion component is dominant, which is explained as follows. Firstly, the 782 nm laser is aligned parallel to the trap axis, so that the radial micromotion amplitude is suppressed by the near-zero angle between the 782 nm laser and the radial directions. Secondly, since the surrounding Be^+ ions shield the HD^+ from static radial offset fields, the HD^+ ions are trapped symmetrically about (and close to) the nodal line of the r.f. field. These two conditions limit the contribution of the radial micromotion to well below the measured axial amplitude of 11(4) nm. The resulting sidebands are included in the spectral line shape function, leading to an additional frequency shift of $-55(20)$ kHz with respect to the case of zero micromotion. After correcting for all systematic frequency shifts (Tab. 5.1), we finally obtain $\nu_0 = 383,407,177.38(41)$ MHz.

5.2.4 Discussion

Our frequency value ν_0 of the $(v,L):(0,2) \rightarrow (8,3)$ transition is in good agreement with the more accurate theoretical value [2] $\nu_{\text{th}} = 383,407,177.150(15)$ MHz. The contribution of the QED terms [1, 2, 127] to this frequency amounts to $-1547.225(15)$ MHz ($-4035.46(4)$ p.p.b.), and our measurement therefore confirms the validity of QED in a molecular system at an unprecedented level of 2.7×10^{-4} . We furthermore note that our measurement is sensitive to (and in agreement with) QED terms up to order $m_e \alpha^7$, given that the $m_e \alpha^7$ term contributes 780(15) kHz (i.e. 2.03(4) p.p.b.) to the transition frequency.

Salumbides *et al.* [69] showed that spectroscopic tests of molecular QED can be used to set upper bounds on a hypothetical fifth force, acting between hadrons at separations of the order of 1 Å, and arising from the exchange of unknown, massive virtual particles. Modelling such a hadron-hadron interaction with a Yukawa-type potential of the form $\hbar c \alpha_5 e^{-r/\lambda}/r$ and computing the resulting frequency shift to ν_0 , we can exploit the 1 p.p.b. agreement between theory and experiment to rule out (at the 90% confidence level) interactions at a range $\lambda = 1-2$ Å (corresponding to force-carrying particles with mass $m_Y = 1-2$ keV c^{-2}) with an interaction strength relative to the

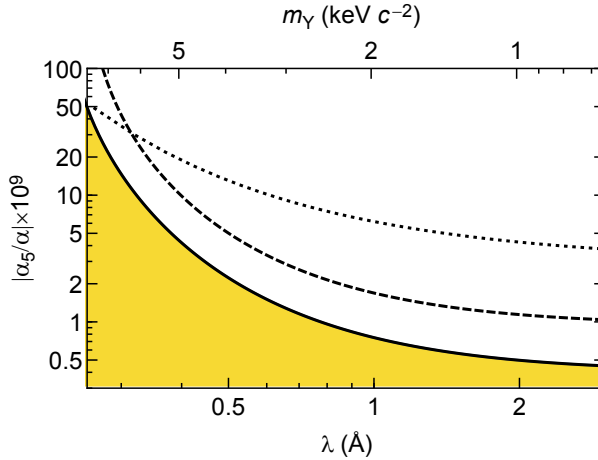


Figure 5.4: Constraint on fifth forces between hadrons at the Ångstrom scale. The high accuracy of our result and the good agreement with theory allow constraining the strength of hypothetical hadron-hadron interactions [69] with a characteristic range of the order of 1 Å, mediated through virtual particles with a mass of order 1 keVc⁻². The present result (solid curve) improves several times on the previous best constraints obtained from HD⁺ (dashed curve) and neutral molecular hydrogen (D₂, dotted curve) [69], ruling out interactions with strengths $|\alpha_5/\alpha| \geq 5 \times 10^{-10}$ (90% confidence level). The yellow region remains unexplored by this experiment.

fine-structure constant, $|\alpha/\alpha_5|$, larger than $5\text{--}8 \times 10^{-10}$ (Fig. 5.4). In a similar way, applying the Arkani-Hamed-Dimopoulos-Dvali formulation to probe the effect of compactified higher dimensions on energy levels in molecules [71, 72], we place an improved upper bound of $0.5 \mu\text{m}$ on the compactification radius of higher dimensions in eleven-dimensional M-theory.

Four decades ago, Wing *et al.* [57] suggested that molecular theory could one day be used to translate measured vibrational frequencies of HD⁺ to a new value of the proton-electron mass ratio, μ . The high accuracy of our result and the good agreement with theory, which assumes the 2010 Committee on Data for Science and Technology (CODATA) recommended value $\mu_{\text{CODATA}10}$, now allow the first determination of μ from molecular vibrations. Previously [93] we had derived the sensitivity relation $\delta\mu/\mu = -2.66 \delta\nu/\nu$, which we employ to adjust $\mu_{\text{CODATA}10}$ to a new value, μ_{HD^+} , such that the theoretical frequency matches our experimental value. We thus find $\mu_{\text{HD}^+} = 1,836.1526695(53)$, with a relative uncertainty of 2.9 p.p.b. which approaches that of the values taken into account in the 2010 CODATA adjustment [128]. For example, the value

reported by Farnham *et al.* is only a factor of 1.3 more precise than our result [129]. While the precision of a very recent determination by Sturm *et al.* is still 31 times higher [130], we point out that our method yields μ as a single parameter from molecular vibrations, whereas most other μ values are ratios of individual determinations of the electron and proton relative atomic masses (exceptions are μ determinations from atomic laser spectroscopy [131, 132]). Therefore, the agreement of μ_{HD^+} with all other values of μ forms an additional consistency check of the various (and vastly different) methods used (Fig. 5.5b). In particular, it implies that relativistic quantum mechanics and QED consistently describe at the few-p.p.b. level such diverse systems as the bound electron [130, 133, 134] antiprotonic helium [131], and the molecular hydrogen ion. Furthermore, of all the methods which produce μ as a single parameter, our approach is surpassed only by spectroscopy of antiprotonic helium, which is 2.3 times more precise but additionally requires charge, parity and time reversal invariance [131] (Fig. 5.5a).

In principle, the transition frequency ν_0 depends on the value of other fundamental constants as well, such as the deuteron-proton mass ratio [46], m_d/m_p , the fine structure constant, and the proton charge radius [1, 2]. However, the sensitivity of ν_0 to changes in μ is known to be three times larger than the second largest one, the m_d/m_p sensitivity [46]. Moreover, if we propagate the uncertainties of the 2010 CODATA values of the fundamental constants through the sensitivity relations, we find that the relative contributions by μ , m_d/m_p , α and the proton radius to the theoretical uncertainty of ν_0 are 154, 11.6, 0.004, and 5.13 parts per trillion, respectively. We therefore conclude that μ is the correct parameter to constrain.

The error budget in Table 5.1 reveals that the experimental uncertainty is limited by Doppler broadening. To overcome this, more involved Doppler-free two-photon spectroscopy of HD^+ has been proposed [126], which should reduce the uncertainty to below 1×10^{-12} . This should enable a comparison between theory and experiment which would not only test the QED description of chemically bonded particles at an unprecedented level, but also produce a new value of μ with an uncertainty below 0.1 p.p.b., surpassing the most precise determination of μ obtained from independent electron and proton relative atomic mass measurements [130], which represent a completely different method (Fig. 5.5c). Our work demonstrates the potential of molecular hydrogen ions for the determination of mass ratios of fundamental particles, as well as stringent tests of QED, and searches for new physics.

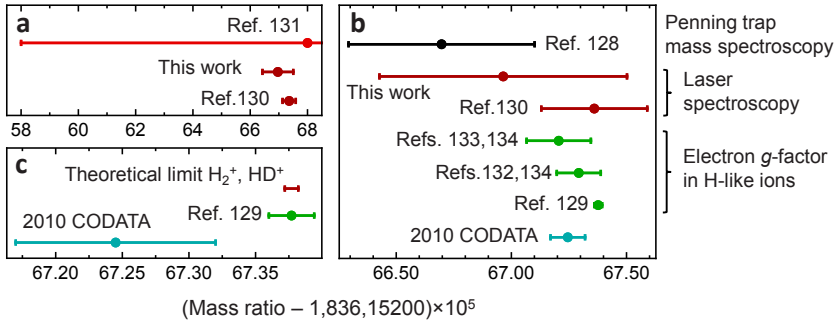


Figure 5.5: Determination of the proton-electron mass ratio. a, Comparison of values of μ obtained as a single parameter from laser spectroscopy. Shown are results from atomic hydrogen [132], atomic antiprotonic helium (which assumes charge, parity and time reversal invariance) [131], and molecular spectroscopy (this work). Error bars represent one standard deviation. b, Overview of the values included in the 2010 CODATA value of μ , obtained through different methods, in comparison with this work. c, If experimental accuracy is improved beyond the $\sim 1 \times 10^{-11}$ relative uncertainty of state-of-the-art QED theory [1, 2], μ could in principle be determined from the molecular hydrogen ion with a precision (red bar) which exceeds that of the current best μ determinations.

5.3 Supplementary methods informations

5.3.1 Experimental procedure

We typically store 40 to 85 HD^+ ions in a linear rf trap, together with about 750 Be^+ ions, which are laser cooled to a temperature of 5–10 mK using a continuous-wave (CW) 313 nm laser beam propagating along the symmetry (z) axis of the trap. As a consequence, only the axial motion of the Be^+ ions is laser-cooled directly. However, the three-dimensional extent of the Coulomb crystal ensures good coupling of the axial motion to the radial motion of the Be^+ and HD^+ ions, so that both Be^+ and HD^+ are efficiently cooled in all three dimensions. Although larger numbers of ions may be trapped, smaller ion numbers ensure better reproducibility of the experimental conditions. The stronger confinement of HD^+ by the pseudopotential leads to the formation of a string or zig-zag structure of HD^+ ions along the nodal line of the r.f. field, which coincides with the z -axis. Be^+ ions arrange themselves in a three-dimensional ellipsoidal structure surrounding the HD^+ . At temperatures below 0.1 K, the two-species ion ensemble solidifies into a Coulomb crystal. 313 nm fluorescence

5. PROBING QED AND FUNDAMENTAL CONSTANTS THROUGH LASER SPECTROSCOPY OF VIBRATIONAL TRANSITIONS IN HD⁺

photons emitted by Be⁺ are imaged onto an electron multiplied charge-coupled device (EMCCD) camera and a photomultiplier tube. We obtain a measure of the number of trapped HD⁺ ions by resonantly driving their radial secular motion (800 kHz) using an a.c. electric field [93]. MD simulations indicate that this secular excitation heats up and melts the ion ensemble, heating the Be⁺ ions to an average temperature (in the z -direction) \bar{T}_0 proportional to the number of HD⁺, N_{HD^+} . Typically, $\bar{T}_0 = 2\text{--}4$ K. For a fixed cooling-laser detuning $\Delta = -18 \Gamma$ (with $\Gamma = 2\pi \times 19.4$ MHz the natural linewidth of the 313 nm cooling transition), this temperature rise leads to Doppler broadening and, thus, to a significant rise in the 313 nm fluorescence rate with average value F . Whereas previous work approximated the fluorescence rise versus N_{HD^+} by a linear dependence [117], we realistically model the (nonlinear) dependence of F on N_{HD^+} , and take this into account in our analysis (see Spectral line shape function for fitting).

To excite the $(v, L): (0, 2) \rightarrow (8, 3)$ rovibrational transition at 782 nm, we send a CW 782 nm laser beam along the z -axis, counter-propagating the 313 nm laser beam. The 782 nm radiation is obtained from a titanium:sapphire laser with a linewidth of 0.5 MHz, which is frequency locked to an optical frequency comb laser as follows. The frequency of the optical beat note of the 782 nm laser with a nearby mode of the comb is measured by a counter every 30 ms. From the measured beat-note frequency, the comb repetition rate, comb carrier-envelope offset frequency, and the comb mode number we determine the lasers optical frequency. The counter output is fed into a digital feedback loop, which controls the 782 nm laser so as to stabilise the beat-note frequency to a pre-set value. The comb is fully referenced to a GPS-disciplined rubidium atomic clock (providing long-term relative accuracy at the level of 2×10^{-12}), and the frequency uncertainty of our optical frequency measurement system (10 kHz) is limited solely by the frequency instability of the locked 782 nm laser averaged over the 10 s of REMPD. To detect excitation to the $v=8$ state by the 782 nm laser, we overlap this beam with a CW 532 nm laser beam, leading to REMPD of HD⁺ (Fig. 5.1a). An experimental cycle looks as follows. We first load a fresh sample of HD⁺ and find a measure, F_i , of the initial ion number, N_i , by secular excitation. We subsequently lower the 313 nm cooling laser intensity and detuning to reduce the ion temperature to ~ 10 mK, and expose the ions to the 313 nm, 782 nm and 532 nm lasers for 10 s. Afterwards, we apply secular excitation to determine the fluorescence level F_f corresponding to the remaining ion number, N_f , and we define a signal $S = (F_i - F_f)/F_i$. Repeating this cycle for different values of the 782 nm laser frequency, ν , we obtain a spectrum consisting of 1772 points (Fig. 5.2a). Noise in the spectrum is primarily due to the stochastic nature of REMPD of small HD⁺ ensembles with a mean rotational-hyperfine occupancy of the order of one ion per state.

5.3.2 Spectral line shape function for fitting

Hyperfine rate equations allow computing the evolution of a sample of HD^+ ions, with an initial thermal rotational distribution [116] corresponding to $T = 300(5)$ K, under the influence of REMPD lasers, BBR and losses due to chemical reactions with background-gas molecules (Figs. 1b,d). Population in rotational states with $L = 0 - 5$ is included, thus ignoring the 2.4% population in $L = 6$ and higher. Accurate hyperfine line strengths at the magnetic sub-state level are obtained by extending the approach of Koelemeij [111] so as to include hyperfine structure and the Zeeman effect. The response to the 782 nm laser of each hyperfine level is modelled using a Doppler-broadened profile based on q -Gaussians. For the assessment of the Zeeman effect, the hyperfine rate equations are adapted to include Zeeman line shifts and broadening due to hyperfine line splitting (which remains much smaller than the 16 MHz Doppler width). The q parameter is determined from realistic MD simulations (which take into account the time-dependent trap potential and momentum changes by scattering of photons from the cooling laser) with an uncertainty limited by the minimum and maximum expected rates of heating events. Solving the rate equations allows predicting the fractional loss of HD^+ , ϵ , as a function of the 782 nm laser frequency relative to the hyperfine-less frequency, $\nu - \nu_0$, the intensity, I_{laser} , of the 782 nm laser, and the HD^+ motional temperature, T_{HD^+} . We obtain a smooth, continuous spectral line shape function for fitting as follows. First, we compute ϵ on a dense three-dimensional grid of values $(\nu, I_{\text{laser}}, T_{\text{HD}^+})$, which we subsequently interpolate to obtain a four-dimensional function $\epsilon(\nu - \nu_{0,\text{fit}}, I_{\text{laser}}, T_{\text{HD}^+})$. Using the shorthand notation $\epsilon(\nu - \nu_{0,\text{fit}}, I_{\text{laser}}, T_{\text{HD}^+}) = \epsilon$, and making use of the linear dependence of \bar{T}_0 on N_{HD^+} found from MD simulations, the average Be^+ temperatures during secular excitation of HD^+ before and after REMPD are given by $T_i = \bar{T}_0(N_i)$ and $T_f = \bar{T}_0((1 - \epsilon)N_f)$, respectively. We consecutively insert these temperature values in the scattering rate function R^{MB} , defined as

$$R^{\text{MB}}(T) = \frac{\Gamma}{2} \sqrt{\frac{m_{\text{Be}}}{2\pi k_B T}} \int \frac{I/I_{\text{sat}}}{I/I_{\text{sat}} + 1 + (2(\Delta - \mathbf{k}v_k)/\Gamma)^2} \exp\left(-\frac{m_{\text{Be}}v^2}{2k_B T}\right) dv_k, \quad (5.3)$$

which includes the beryllium mass, m_{Be} , and the fixed 313 nm laser detuning, wave vector, \mathbf{k} , and saturation parameter, I/I_{sat} . The integration is performed over the distribution of Be^+ velocities \mathbf{v} along \mathbf{k} , i.e. $v_k \equiv \mathbf{k} \cdot \mathbf{v}/|\mathbf{k}|$. This function is used to model the fluorescence rise F observed in the experiment, and allows us to construct a five-dimensional fit function $S_{\text{fit}}(\nu - \nu_{0,\text{fit}}, I_{\text{laser}}, T_{\text{HD}^+}) = [R^{\text{MB}}(T_i) - R^{\text{MB}}(T_f)]/[R^{\text{MB}}(T_i)R_0^{\text{MB}}]$, with R_0^{MB} the steady-state scattering rate before secular excitation. The function S_{fit} realistically models the signal S (Fig. 5.2c), and is used for fitting.

5. PROBING QED AND FUNDAMENTAL CONSTANTS THROUGH LASER SPECTROSCOPY OF VIBRATIONAL TRANSITIONS IN HD^+

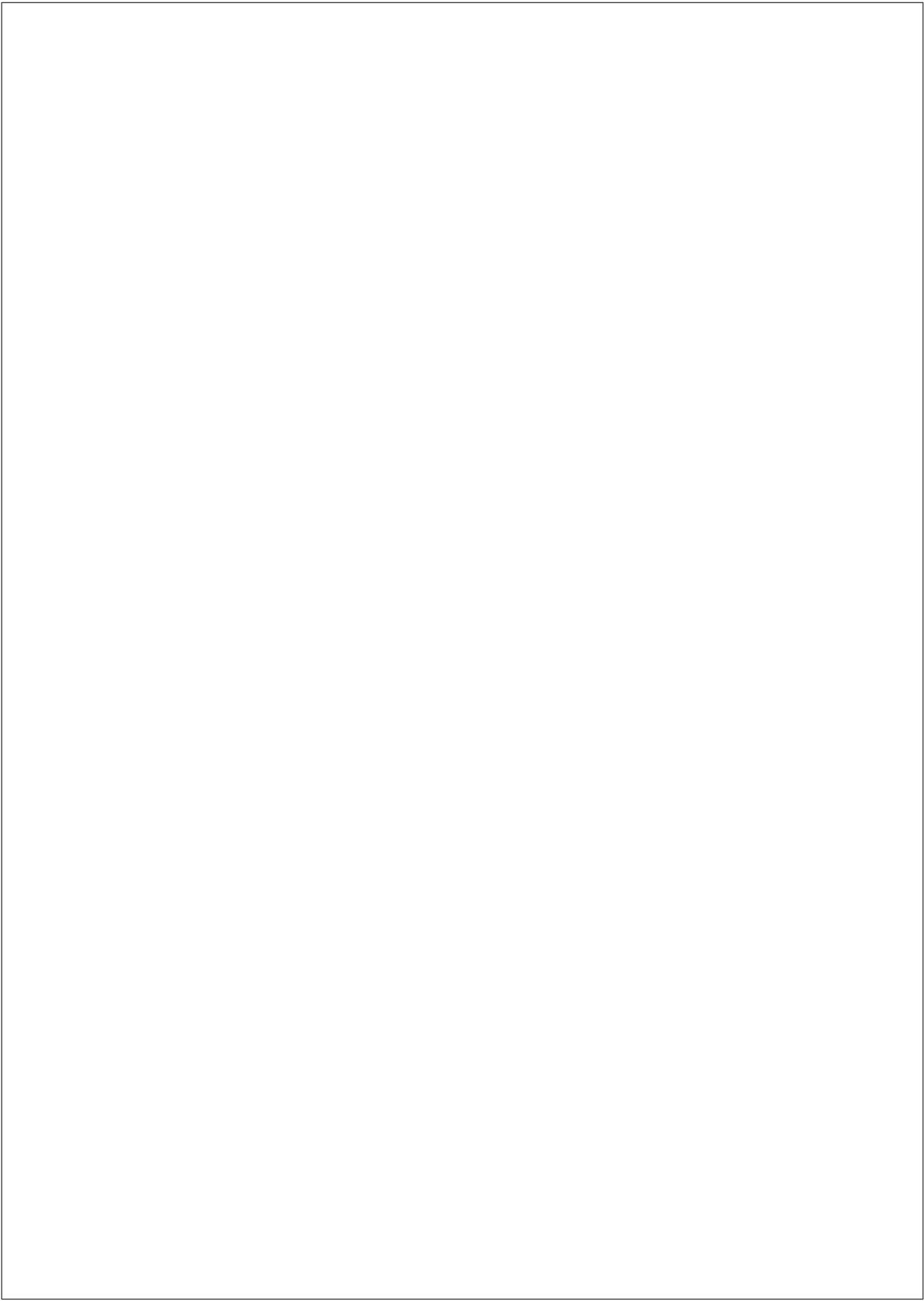
We employ the above model also to estimate the uncertainties due to several systematic effects. For example, MD simulations predict a slight increase of T_{HD^+} and q with increased REMPD rates in the scenario of inefficient thermalisation of fast D^+ . We can estimate the frequency shift due to this effect by making both T_{HD^+} and q REMPD-rate dependent. This leads to an additional frequency uncertainty of 61 kHz, which is included in the error associated with Doppler effects due to chemistry (Table 5.1). From our model we furthermore deduce that ignoring states with $L \geq 6$ introduces an uncertainty of 32 kHz, while the possible 5 K error in the BBR temperature estimate (which takes into account day-to-day temperature variations and the possibility that the trap electrodes may be at a slightly higher temperature due to r.f. dissipation) translates to a 5 Hz effect [135].

Table 5.1: Systematic shifts and uncertainty budget.

Origin	Shift (MHz)	Uncertainty	
		(MHz)	(ppb)
Resolution (statistical fit error)	0	0.33	0.85
Doppler effect due to chemistry	-0.25 ¹	0.25	0.66
Ignoring population $L=6$ in rate equations	0	0.032	0.083
T_{HD^+} variation in spectrum	0	0.028	0.072
Doppler effect due to micromotion	-0.055 ¹	0.020	0.052
Frequency measurement	0	0.010	0.026
BBR temperature	0	0.005	0.013
Zeeman effect	-0.0169	0.003	0.008
Stark effect	-0.0013	0.0001	0.0004
Electric-quadrupole shift	0 ²	0.0001	0.0003
2 nd order Doppler effect	0 ²	0.000005	0.00001
Total	-0.0182	0.41	1.1

¹ This is a shift with respect to a scenario with a zero effect of q or micromotion, and serve to illustrate the size of the effect. The shift itself, however, is absorbed in the value of $\nu_{0,\text{fit}}$.

² The value of these shifts is actually nonzero but negligibly small, and therefore ignored here.



Molecular dynamics simulations

MD simulations are implemented in FORTRAN code in order to realistically describe the dynamics of trapped and laser-cooled ions in the presence of the time-dependent trap field, 313 nm photon scattering by the Be^+ ions, and fast ionic products from chemical reactions. A cycle of one time step starts by computing the sum of the forces acting on each ion, which consists of the Coulomb force, \vec{F}_C , the time-dependent force from the trapping field field, F_{trap} , and an optional rf electric field, F_{SS} which drives the secular motion:

$$\vec{F}_{\text{tot}} = \sum \vec{F} = \vec{F}_C + \vec{F}_{\text{trap}} + \vec{F}_{\text{SS}}. \quad (\text{A.1})$$

Note that we here use arrow symbols to indicate vectors, instead of bold symbols as used elsewhere in this thesis. The radial and axial part of \vec{F}_{trap} are given by

$$F_{\text{trap},x,y} = -\frac{QV_0}{R'^2}(x\hat{x} - y\hat{y})\cos(\Omega t) + \frac{1}{2}Q\omega_z^2(x\hat{x} + y\hat{y}) \quad (\text{A.2})$$

and

$$F_{\text{trap},z} = az + bz^3 + cz^5, \quad (\text{A.3})$$

where ω_z is the secular angular frequency in the z -direction. The constants a , b and c depend on the trap geometry, which are determined through a finite-element analysis performed with the software package SIMION. The forces exerted on each ion are calculated, and leapfrog integration [136] provides the new velocities \vec{v}_{i+1} and positions \vec{x}_{i+1} at the i^{th} time step Δt :

$$\begin{aligned} \vec{v}_{i+1} &= \vec{v}_i + (\vec{F}_{\text{tot},i}/m_j)\Delta t \\ \vec{x}_{i+1} &= \vec{x}_i + \vec{v}_{i+1}\Delta t \end{aligned} \quad (\text{A.4})$$

where m_j is the mass of the j^{th} ion. The new positions, \vec{x}_{i+1} , are inserted into A.1, after which the next cycle starts.

Doppler-cooling is included at the level of single-photon scattering. Photon momentum kicks are simulated as velocity changes where absorption only takes place in the laser direction. In order to include ion motional heating which occurs in the trap, we implemented additional stochastic velocity kicks with a size of the recoil momentum of a single 313 nm photon with random directions. If an average kick rate of 75 MHz is used, realistic ion temperatures of around 10 mK are obtained.

The processes of elastic and inelastic neutral-ion collisions are simulated as velocity kicks in random directions. For example, simulating reaction (7) in Table 4.1, a BeH^+ is created at 10 mK and then its speed is modified.

Simulation of particles which in some cases have high velocities requires the use of a variable time step size. (If the proper step size is not observed, two particles with a high velocity difference at close distance could skip each other within one time step instead of colliding). The default step size is $\Delta t = 0.2$ ns. However, if for any of the trapped particles the condition $v_j \Delta t > 10 \times \min\{\Delta x_{jk}\}$ is met, where $\min\{\Delta x_{jk}\}$ is the distance between particle j with velocity v_j and the nearest particle k , the time step Δt is reduced by a factor of 10 and *vice versa*.

To simulate EMCCD images, we made use of a simpler MD implementation, which treats the motion of the ions in the pseudopotential approximation and which does not include high-energy ions. This allows for a larger time integration step (10 ns) and, thus, faster MD simulations.

Derivation of the non-linear fluorescence function

The relative HD⁺ loss during REMP, ϵ , is related to the spectroscopic signal S through the non-linear function f_{NL} , which we derive here. The fluorescence yield during a secular scan depends on the Be⁺ temperature, T , and is described by the scattering rate formula integrated over a Maxwell-Boltzmann velocity distribution. If we neglect micromotion effects, we find the overall scattering rate R^{MB} :

$$R^{MB}(T) = \frac{\Gamma}{2} \sqrt{\frac{m_{Be}}{2\pi k_B T}} \int \frac{I/I_{sat}}{I/I_{sat} + 1 + (2(\Delta - \mathbf{k}v_k)/\Gamma)^2} \exp\left(-\frac{m_{Be}v^2}{2k_B T}\right) dv_k, \quad (\text{B.1})$$

where \mathbf{v} along \mathbf{k} , i.e. $v_k \equiv \mathbf{k} \cdot \mathbf{v}/|\mathbf{k}|$ is integrated over the distribution of Be⁺ velocities. During the experiment we used the values $\Delta = 2\pi \times -300$ MHz and $I/I_{sat} = 67$.

During a secular scan, the temperature T varies, which leads to a fluorescence peak as described by Eq. (B.1). The spectroscopic signal S is the relative difference between the areas under the fluorescence peaks (see equation 4.11). We may rewrite the area, A , as

$$A = C \left(\frac{R^{MB}(\bar{T})}{\Delta t} - \frac{R^{MB}(\bar{T}_{bl})}{\Delta t} \right), \quad (\text{B.2})$$

where C is a constant taking into account the collection and quantum efficiencies of the PMT or EMCCD imaging system, Δt denotes the duration of the secular scan (10 s), \bar{T} stands for the average value of T during a secular scan, and \bar{T}_{bl} is the average baseline temperature during Δt . In the experiment, the

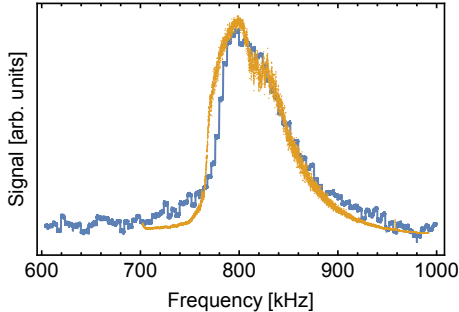


Figure B.1: A simulated (yellow) and a real (blue) secular scan peak plotted in the same window.

baseline may have a slope corresponding to the wing of the secular resonance of particles with mass 4 and 5 amu (see for example, Fig. 4.7). This slope is detected and removed by the MATHEMATICA code we use to analyze the PMT signal traces. Inserting equation B.2 into Eq. (4.11), we obtain

$$S = \frac{R^{MB}(\bar{T}_i) - R^{MB}(\bar{T}_f)}{R^{MB}(\bar{T}_i) - R^{MB}(\bar{T}_{bl})}, \quad (\text{B.3})$$

which is a relationship between the spectroscopic signal S and the average ion temperatures during the initial and final secular scan, \bar{T}_i and \bar{T}_f respectively.

The relationship between the number of trapped HD^+ molecules and \bar{T} can be obtained from MD simulations. A realistic Coulomb crystal is simulated containing 750 trapped Doppler-cooled Be^+ ions and with HD^+ numbers varying from 0 to 100 (for details see appendix A). Concerning the number of particles with mass 4 and 5 amu (H_2D^+ and HD_2^+), we take the two scenarios a and b into account that are introduced in 4.4.2. The simulated secular scans over the HD^+ secular resonance frequency produce fluorescence peaks which agree qualitatively with those obtained in the laboratory as shown in Fig. B.1.

The simulated duration of a secular scan is approximately 100 ms, which is much shorter than the ten seconds of a real secular scan. The time scale at which temperature and fluorescence changes take place in the simulation is 1 ms or longer, which is much longer than the time scale of fluorescence dynamics during laser cooling, which takes place at time scales of the order of $10 \mu\text{s}$ [137]. Therefore, we can rely on results of the simulated secular scan peaks.

The MD simulations reveal a linear relationship between the number of trapped HD^+ ions and \bar{T} . This confirms the intuitive picture in which the Be^+ temperature rise during secular excitation is directly proportional to the

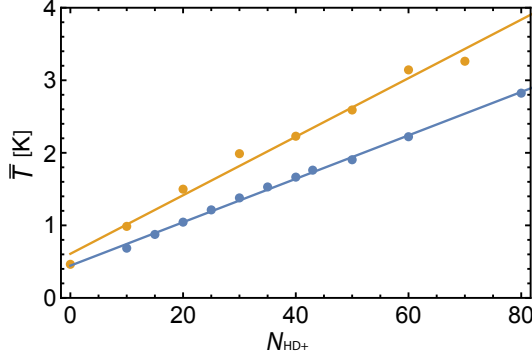


Figure B.2: Results from MD simulations that give the average ion temperature during a secular scan \bar{T} versus the number of HD^+ ions N_{HD^+} for both the scenarios a (blue dots) and b (yellow dots). The blue and yellow lines represent least-squares fits, showing a linear relationship between \bar{T} and N_{HD^+} .

number of HD^+ ions. Figure B.2 shows the $(N_{\text{HD}^+}, \bar{T})$ relationship for the two scenarios a and b. Having established that \bar{T} is a measure of the number of trapped HD^+ molecules, we now combine the relations $\epsilon = (N_i - N_f)/N_i$, $\bar{T}_i = c_1 N_i + c_2$ and $\bar{T}_f = c_1 N_f + c_2$, where c_1 and c_2 are constants derived from MD simulations (Fig. B.2), to obtain

$$\bar{T}_f(\epsilon) = \bar{T}_i(1 - \epsilon) + c_2\epsilon. \quad (\text{B.4})$$

\bar{T}_i can also be defined as the average temperature with zero HD^+ loss ($\bar{T}_i = \bar{T}_f(\epsilon = 0) \equiv \bar{T}_0$), and the term c_2 can be considered as the average baseline temperature ($c_2 = \bar{T}_f(\epsilon=1) = \bar{T}_{\text{bl}}$). Inserting Eq. (B.4) into Eq. (B.3) results in the nonlinear function

$$f_{\text{NL}}(\bar{T}_0, \epsilon) \equiv \frac{R^{MB}(\bar{T}_0) - R^{MB}((\bar{T}_{\text{bl}} - \bar{T}_0)\epsilon + \bar{T}_0)}{R^{MB}(\bar{T}_0) - R^{MB}(\bar{T}_{\text{bl}})}, \quad (\text{B.5})$$

which is plotted for scenario a in Fig. B.3.

In the analysis \bar{T}_0 is treated as a free fit parameter. \bar{T}_{bl} is kept at a fixed value which is obtained from MD simulations. From Fig. B.2 it can be seen that $\bar{T}_{\text{bl}} \simeq 0.5$ K for scenarios a and b. This indicates that the rf field used for secular excitation already induces heating of Be^+ while the field is still off resonance. This effect is also seen in the experiment.

The nonlinear function f_{NL} is used to map the relative HD^+ loss ϵ onto the spectroscopic signal S . In Sec. 4.4.5 we need to map S to ϵ , which requires the inverse non-linear function f_{NL}^{-1} . This inverse function is obtained by use of MATHEMATICA.

B. DERIVATION OF THE NON-LINEAR FLUORESCENCE FUNCTION

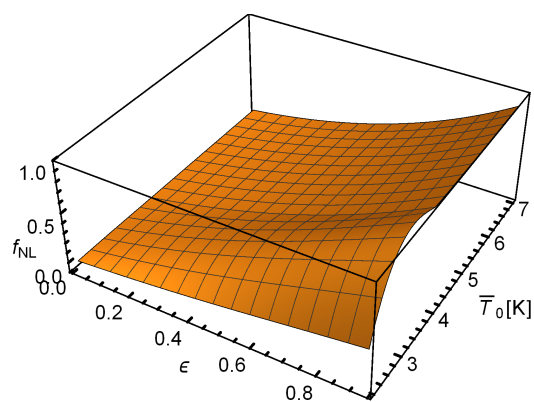


Figure B.3: 3D plot of the function $f_{\text{NL}}(\bar{T}_0, \epsilon)$ (here plotted for scenario a) which connects the raw measurement signal S to the actual fractional loss of HD^+ , ϵ .

Micromotion fit function

The Be^+ micromotion amplitude can be written as

$$\mathbf{x}_0 = \frac{Q}{m_{\text{Be}}\Omega^2} \mathbf{E}_t(x, y, z, t) \quad (\text{C.1})$$

where Q is the elementary charge. The measured micromotion amplitude can be written as

$$x_{0,k} = \frac{\mathbf{k} \cdot \mathbf{x}_0}{\|\mathbf{k}\|}, \quad (\text{C.2})$$

which is the projection of the 313 nm laser direction onto \mathbf{x}_0 . \mathbf{E}_t in Eq. (C.1) is the E-field in the ion trap, which can be expressed as [87]

$$\begin{aligned} \mathbf{E}_t(x, y, z, t) \cong & -\frac{V_0}{R^2}(x\hat{x} - y\hat{y}) \cos(\Omega t) \\ & -\frac{\kappa U_0}{Z_0^2} \times (2z\hat{z} - x\hat{x} - y\hat{y}), \end{aligned} \quad (\text{C.3})$$

where R is half the distance between two diagonally opposing electrodes, U_0 is the endcap voltage, Z_0 stands for half the end cap-to-end cap distance and κ is a shielding factor. From simulations of the rf trap circuitry with the simulation software SPICE, we find a very small phase difference ϕ_{ac} of 4 mrad in between the rf electrodes, which has a negligible effect on the ion micromotion and is ignored here. With the program SIMION, we have calculated the shielding factor κ and the static electric fields \mathbf{E}_{dc} as a function of the dc voltages applied to the trap electrodes. From the static electric fields, the radial ion displacement r_d is obtained by balancing the ponderomotive force and static E -field in the radial direction:

$$m_{\text{Be}}\omega_r^2 r_d = -qE_{\text{dc}} \quad (\text{C.4})$$

C. MICROMOTION FIT FUNCTION

where ω_r is the radial secular trap frequency. By inserting the x - and y -components of r_d in Eq. (C.3), the value of E_t at the location of the ions is obtained.

A geometric imperfection of the trap could lead to an axial rf field, which can be written as (here we ignore the small modification of the radial rf field of the trap due to the same imperfection):

$$E_{\text{ax,HD}^+}(V_0, t) = \frac{1}{Q} \frac{V_0}{V_{0,e}} m_{\text{HD}} x_{\text{HD}} \Omega^2 \cos \Omega t \quad (\text{C.5})$$

where x_{HD} is the HD^+ micromotion amplitude along the trap z -axis, m_{HD} is the mass of HD^+ , and $V_{0,e}$ is the rf voltage used during the spectroscopy measurement, which is 270 V.

Now, we turn to the case of a linear string of Be^+ ions, which is the configuration used to determine the axial rf field amplitude. Adding $E_{\text{ax,HD}^+}$ to the z -component of \mathbf{E}_t gives a new expression for \mathbf{E}_t which is inserted into Eq. (C.1). We then obtain the following expression for \mathbf{x}_0 :

$$\mathbf{x}_0 = \left(\begin{array}{c} \frac{2E_{t,x}qR^2V_0Z_0^2}{qV_0^2Z_0^2 - 2m_{\text{Be}}R^4U_0\kappa\Omega^2}, \\ \frac{2E_{t,y}qR^2V_0Z_0^2}{qV_0^2Z_0^2 - 2m_{\text{Be}}R^4U_0\kappa\Omega^2}, \\ \frac{m_{\text{HD}}V_0x_{\text{HD}}}{m_{\text{Be}}V_{0,e}} \end{array} \right), \quad (\text{C.6})$$

which is subsequently inserted into Eq. (C.2), together with the wavevector, which is written as

$$\mathbf{k} = \frac{2\pi}{\lambda} (\sin(\theta) \cos(\phi), \sin(\theta) \sin(\phi), \cos(\theta)). \quad (\text{C.7})$$

Here θ is the angle between \mathbf{k} , and the trap z -axis and ϕ is the angle between \mathbf{k} and the trap y -axis, which is very close to $\pi/4$ in our setup. The value of θ lies between ± 10 mrad and is treated as a free fit parameter. We insert Eqs. (C.7) and (C.6) into Eq. (C.2) and then expand the expression in powers of θ . This gives us the following fit function:

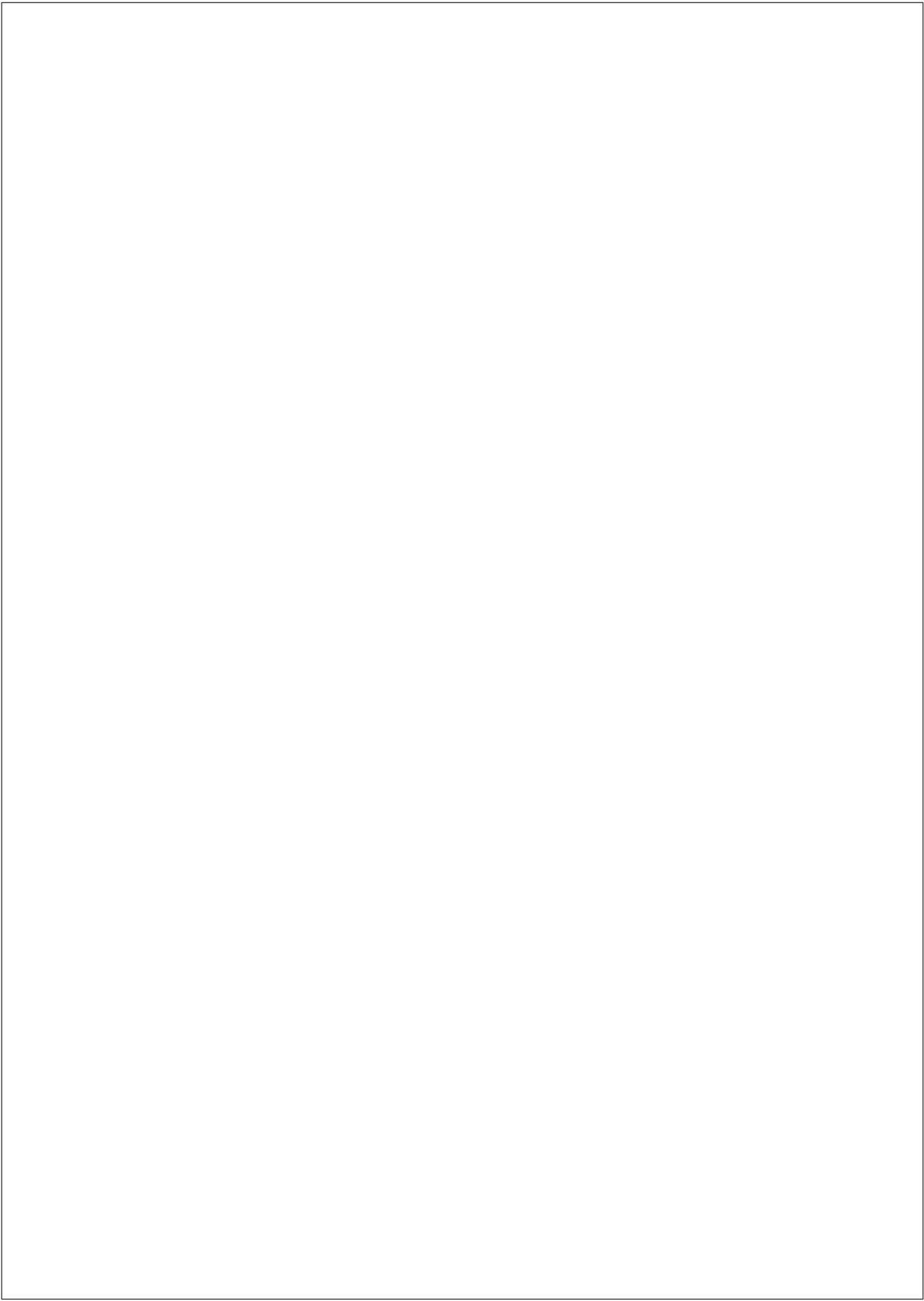
$$x_{0,k}(V_0) = \frac{m_{\text{HD}}}{m_{\text{Be}}} \frac{V_0 x_{\text{HD}}}{V_{\text{cal}}} - \frac{8(E_{\text{h,offs}} - E_{\text{v,offs}} + \delta E_{\text{h}} - \delta E_{\text{v}})Q^2V_0}{m_{\text{Be}}R^2\Omega^4(2a_{\text{M}} + q_{\text{M}}^2)}\theta + \mathcal{O}(\theta^2). \quad (\text{C.8})$$

Here $E_{h,\text{offs}}$, $E_{v,\text{offs}}$ are the applied static electric fields, and δE_h , δE_v the unknown offset electric fields in the horizontal and vertical directions (due to *e.g.* charging of electrodes). The Mathieu parameters a_M and q_M are defined as:

$$a_M = \frac{-4Q\kappa U_0}{m_{\text{Be}}Z_0^2\Omega^2}, \quad q_M = \frac{2QV_0}{m_{\text{Be}}R^2\Omega^2}. \quad (\text{C.9})$$

The displacement of the Be^+ string in the vertical direction can be accurately determined with images of the EMCCD camera, and therefore δE_h can be zeroed (for example by minimizing the displacement of the Be^+ string while the radial confinement of the trap is modulated by varying the rf amplitude). However, the displacement in the horizontal direction is not accurately known and therefore we treat δE_h as another free fit parameter. In summary, we use Eq. (C.8) as a fit function with x_{HD^+} , θ and δE_h as free fit parameters while neglecting higher orders of θ . The fitted curves and the result for $x_{0,k}$ are shown in Sec. 4.4.3.

The question arises what happens if the 782 nm laser propagates at a small angle with respect to the trap axis, while the HD^+ ions form a shell structure around the trap axis. In this case a small fraction of the radial micromotion is projected onto the wavevector. However, from Eqs. (C.1-C.3) it follows that the sign of this additional micromotion alternates for each quadrant in the (x, y) plane. As long as the radial micromotion component does not exceed the axial micromotion amplitude (which is the case here), the former averages out to zero given the radial symmetry of the HD^+ crystal.



Stark shift calculations

Here we summarize the formulas that are used to calculate the ac Stark shift of a ro-vibrational transition $(v, L) \rightarrow (v', L')$ in the HD^+ molecule induced by a laser with intensity I and polarization state p . A general expression for the second-order energy shift depending on the angle θ between the polarization direction and the quantization axis is:

$$\Delta E = -\frac{1}{2} \frac{I}{c} \left[\alpha_{vL}^{(0)}(\omega) + P_2(\cos \theta) \frac{3M^2 - L(L+1)}{L(2L-1)} \alpha_{vL}^{(2)}(\omega) \right], \quad (\text{D.1})$$

where $P_2(x) = \frac{1}{2}(3x^2 - 1)$ is a Legendre polynomial. This expression contains the scalar and tensor polarizabilities

$$\begin{aligned} \alpha_{vL}^{(0)}(\omega) &= 4\pi a_0^3 Q_s, \\ \alpha_{vL}^{(2)}(\omega) &= 4\pi a_0^3 \sqrt{\frac{L(2L-1)}{(L+1)(2L+3)}} Q_t, \end{aligned} \quad (\text{D.2})$$

where a_0 is the Bohr radius and Q_s and Q_t stand for the two-photon scalar and tensor matrix elements:

$$\begin{aligned} Q_s &= \frac{\langle vL \| Q^{(0)} \| v'L \rangle}{\sqrt{2L+1}} \\ Q_t &= \frac{\langle vL \| Q^{(2)} \| vL \rangle}{\sqrt{2L+1}}. \end{aligned} \quad (\text{D.3})$$

Here $Q^{(0)}$ and $Q^{(2)}$ are the irreducible scalar and tensor components that belong to the two-photon operator (in atomic units):

$$Q_{pp}(E) = \mathbf{d} \cdot \boldsymbol{\epsilon}_p \frac{1}{H - E} \mathbf{d} \cdot \boldsymbol{\epsilon}_p, \quad (\text{D.4})$$

D. STARK SHIFT CALCULATIONS

with Hamiltonian H , dipole moment operator, \mathbf{d} and polarization vector $\epsilon_{\mathbf{p}}$. The matrix elements Q_s and Q_t were calculated numerically by J.-Ph. Karr using the three-body variational wave functions described in [14].

Since the hyperfine structure is partially resolved in this spectrum, we also have to consider the contribution of the Stark shifts to off-resonant coupling to hyperfine levels in $v = 0$ and $v = 8$ by the 782 nm laser during spectroscopy. Here, the situation is more complicated as the 782 nm laser also non-resonantly couples $v = 8$ states to continuum states above the dissociation limit of the $1s\sigma$ electronic ground state. The 782-nm contribution to the Stark shift was calculated by J.-Ph. Karr at the hyperfine level. The corresponding shifts turn out to be negligible for our experiment, contributing only at the level of a few Hertz.

Bibliography

- [1] Korobov, V. I., Hilico, L. & Karr, J.-Ph. $m\alpha^7$ -order corrections in the hydrogen molecular ions and antiprotonic helium. *Phys. Rev. Lett.* **112**, 103003 (2014).
- [2] Korobov, V. I., Hilico, L. & Karr, J.-Ph. Theoretical transition frequencies beyond 0.1 ppb accuracy in H_2^+ , HD^+ , and antiprotonic helium. *Phys. Rev. A* **89**, 032511 (2014).
- [3] Rosenband, T. *et al.* Frequency ratio of Al^+ and Hg^+ single-ion optical clocks; metrology at the 17th decimal place. *Science* **319**, 1808–1812 (2008).
- [4] Chou, C. W., Hume, D. B., Koelemeij, J. C. J., Wineland, D. J. & Rosenband, T. Frequency comparison of two high-accuracy Al^+ optical clocks. *Phys. Rev. Lett.* **104**, 070802 (2010).
- [5] Huntemann, N. *et al.* High-accuracy optical clock based on the octupole transition in $^{171}\text{Yb}^+$. *Phys. Rev. Lett.* **108**, 090801 (2012).
- [6] Godun, R. *et al.* Frequency ratio of two optical clock transitions in $^{171}\text{Yb}^+$ and constraints on the time-variation of fundamental constants. *Phys. Rev. Lett.* **113**, 210801 (2014).
- [7] Huntemann, N. *et al.* Improved limit on a temporal variation of m_p/m_e from comparisons of Yb^+ and Cs atomic clocks. *Phys. Rev. Lett.* **113**, 210802 (2014).
- [8] Takamoto, M., Hong, F.-L., Higashi, R. & Katori, H. An optical lattice clock. *Nature* **435**, 321–324 (2005).
- [9] Ye, J., Kimble, H. J. & Katori, H. Quantum state engineering and precision metrology using state-insensitive light traps. *Science* **320**, 1734–1738 (2008).

BIBLIOGRAPHY

- [10] Swallows, M. D. *et al.* Suppression of collisional shifts in a strongly interacting lattice clock. *Science* **331**, 1043–1046 (2011).
- [11] Hinkley, N. *et al.* An atomic clock with 10^{-18} instability. *Science* **341**, 1215–1218 (2013).
- [12] Bloom, B. *et al.* An optical lattice clock with accuracy and stability at the 10^{-18} level. *Nature* **506**, 71–75 (2014).
- [13] Bureau International de Poids et Mesures. Unité SI de temps (seconde). Website: <http://www.bipm.org/metrology/time-frequency>.
- [14] Karr, J.-Ph. H_2^+ and HD^+ : Candidates for a molecular clock. *J. Mol. Spectr.* **300**, 37 – 43 (2014).
- [15] Schiller, S., Bakalov, D. & Korobov, V. I. Simplest molecules as candidates for precise optical clocks. *Phys. Rev. Lett.* **113**, 023004 (2014).
- [16] Bakalov, D. & Schiller, S. The electric quadrupole moment of molecular hydrogen ions and their potential for a molecular ion clock. *Appl. Phys. B* **114**, 213–230 (2014).
- [17] Schmidt, P. O. *et al.* Spectroscopy using quantum logic. *Science* **309**, 749–752 (2005).
- [18] Schmidt, P. O. *et al.* Spectroscopy of atomic and molecular ions using quantum logic. *Non-Neutral Plasma Physics VI* **862**, 305–312 (2006).
- [19] Mur-Petit, J. *et al.* Temperature-independent quantum logic for molecular spectroscopy. *Phys. Rev. A* **85**, 022308 (2012).
- [20] Sta anum, P. F., Hojbjerg, K., Skyt, P. S., Hansen, A. K. & Drewsen, M. Rotational laser cooling of vibrationally and translationally cold molecular ions. *Nat. Phys.* **6**, 271–274 (2010).
- [21] Shen, J., Borodin, A., Hansen, M. & Schiller, S. Observation of a rotational transition of trapped and sympathetically cooled molecular ions. *Phys. Rev. A* **85**, 032519 (2012).
- [22] Ryder, L. H. *Quantum Field Theory* (Cambridge University Press, 1996).
- [23] Dyson, F. J. The radiation theories of Tomonaga, Schwinger, and Feynman. *Phys. Rev.* **75**, 486–502 (1949).
- [24] Feynman, R. P. Space-time approach to non-relativistic quantum mechanics. *Rev. Mod. Phys.* **20**, 367–387 (1948).

-
- [25] Feynman, R. P. The theory of positrons. *Phys. Rev.* **76**, 749–759 (1949).
- [26] Lamb, W. E. & Retherford, R. C. Fine structure of the hydrogen atom by a microwave method. *Phys. Rev.* **72**, 241–243 (1947).
- [27] Hanneke, D., Fogwell, S. & Gabrielse, G. New measurement of the electron magnetic moment and the fine structure constant. *Phys. Rev. Lett.* **100**, 120801 (2008).
- [28] Hanneke, D., Fogwell Hoogerheide, S. & Gabrielse, G. Cavity control of a single-electron quantum cyclotron: Measuring the electron magnetic moment. *Phys. Rev. A* **83**, 052122 (2011).
- [29] Aoyama, T., Hayakawa, M., Kinoshita, T. & Nio, M. Revised value of the eighth-order QED contribution to the anomalous magnetic moment of the electron. *Phys. Rev. D* **77**, 053012 (2008).
- [30] Aoyama, T., Hayakawa, M., Kinoshita, T. & Nio, M. Tenth-order QED contribution to the electron $g-2$ and an improved value of the fine structure constant. *Phys. Rev. Lett.* **109**, 111807 (2012).
- [31] Bouchendir, R., Cladé, P., Guellati-Khélifa, S., Nez & Biraben, F. New determination of the fine structure constant and test of the quantum electrodynamics. *Phys. Rev. Lett.* **106**, 080801 (2011).
- [32] Bradley, M. P., Porto, J. V., Rainville, S., Thompson, J. K. & Pritchard, D. E. Penning trap measurements of the masses of ^{133}Cs , $^{87,85}\text{Rb}$, and ^{23}Na with uncertainties ≤ 0.2 ppb. *Phys. Rev. Lett.* **83**, 4510–4513 (1999).
- [33] Mount, B. J., Redshaw, M. & Myers, E. G. Atomic masses of ^6Li , ^{23}Na , $^{39,41}\text{K}$, $^{85,87}\text{Rb}$, and ^{133}Cs . *Phys. Rev. A* **82**, 042513 (2010).
- [34] F. Dyson, “Letter to G. Gabrielse”, quoted in *Physics Today*, August 2006, pp. 15–17 .
- [35] Moss, R. Calculations for vibration-rotation levels of HD^+ , in particular for high N . *Mol. Phys.* **78**, 371–405 (1993).
- [36] Moss, R. Calculations for the vibration-rotation levels of H_2^+ in its ground and first excited electronic states. *Mol. Phys.* **80**, 1541–1554 (1993).
- [37] Bethe, H. & Salpeter, E. *Quantum mechanics of one-and two-electrons systems*, vol. 35 (Springer Berlin Heidelberg, 1957).
- [38] Berestetskii, V. B., Lifshitz, E. M. & Pitaevskii, V. *Relativistic quantum theory*, vol. 1 (Pergamon Press, 1974).

- [39] Born, M. & Oppenheimer, R. Zur Quantentheorie der Molekulen. *Annalen der Physik* **389**, 457–484 (1927).
- [40] Bunker, P. & Moss, R. The breakdown of the Born-Oppenheimer approximation: the effective vibration-rotation hamiltonian for a diatomic molecule. *Mol. Phys.* **33**, 417–424 (1977).
- [41] Brown, J. & Carrington, A. *Rotational Spectroscopy of Diatomic Molecules* (Cambridge University Press, Cambridge, 2003), 1 edn.
- [42] Esry, B. D. & Sadeghpour, H. R. Adiabatic formulation of heteronuclear hydrogen molecular ion. *Phys. Rev. A* **60**, 3604–3617 (1999).
- [43] Hilico, L., Billy, N., Grémaud, B. & Delande, D. Ab initio calculation of the $J = 0$ and $J = 1$ states of the H_2^+ , D_2^+ and HD^+ molecular ions. *Eur. Phys. J. D* **12**, 449–466 (2000).
- [44] Korobov, V. I. Coulomb three-body bound-state problem: Variational calculations of nonrelativistic energies. *Phys. Rev. A* **61**, 064503 (2000).
- [45] Cassar, M. M. & Drake, G. W. F. High precision variational calculations for H_2^+ . *J. Phys. B: At. Mol. Opt. Phys.* **37**, 2485 (2004).
- [46] Schiller, S. & Korobov, V. I. Tests of time independence of the electron and nuclear masses with ultracold molecules. *Phys. Rev. A* **71**, 032505 (2005).
- [47] J.-Ph. Karr & Hilico, L. High accuracy results for the energy levels of the molecular ions H_2^+ , D_2^+ and HD^+ , up to $J = 2$. *J. Phys. B: At. Mol. Opt. Phys.* **39**, 2095 (2006).
- [48] Li, H., Wu, J., Zhou, B.-L., Zhu, J.-M. & Yan, Z.-C. Calculations of energies of the hydrogen molecular ion. *Phys. Rev. A* **75**, 012504 (2007).
- [49] Kullie, O. & Kolb, D. High accuracy Dirac-finite-element (FEM) calculations for H_2^+ and Th_2^{179+} . *Eur. Phys. J. D* **17**, 167–173 (2001).
- [50] Ishikawa, A., Nakashima, H. & Nakatsuji, H. Accurate solutions of the Schrödinger and Dirac equations of, HD^+ , and HT^+ : With and without Born-Oppenheimer approximation and under magnetic field. *Chem. Phys.* **401**, 62 – 72 (2012).
- [51] Korobov, V. I., Hilico, L. & Karr, J.-Ph. Calculation of the relativistic Bethe logarithm in the two-center problem. *Phys. Rev. A* **87**, 062506 (2013).

-
- [52] Shuter, W. L. H., Williams, D. R. W., Kulkarni, S. R. & Heiles, C. A search for vibrationally excited interstellar H_2^+ . *Astroph. J.* **306**, 255–258 (1986).
- [53] Oka, T. The infrared spectrum of H_3^+ in laboratory and space plasmas. *Rev. Mod. Phys.* **64**, 1141–1149 (1992).
- [54] Jefferts, K. B. Hyperfine structure in the molecular ion H_2^+ . *Phys. Rev. Lett.* **23**, 1476–1478 (1969).
- [55] Korobov, V. I., Hilico, L. & Karr, J.-Ph. Hyperfine structure in the hydrogen molecular ion. *Phys. Rev. A* **74**, 040502 (2006).
- [56] Korobov, V. I., Koelemeij, J. C. J., Hilico, L. & Karr, J.-Ph. Test of the theoretical hyperfine structure of the molecular hydrogen ion at the 1-ppm level. *available from: arXiv:1510.05206* (2015).
- [57] Wing, W. H., Ruff, G. A., Lamb, W. E. & Spezeski, J. J. Observation of the infrared spectrum of the hydrogen molecular ion HD^+ . *Phys. Rev. Lett.* **36**, 1488–1491 (1976).
- [58] Carrington, A. & Kennedy, R. A. Vibration-rotation spectroscopy of the HD^+ ion near the dissociation limit. *Mol. Phys.* **56**, 935–975 (1985).
- [59] Carrington, A., McNab, I. R. & Montgomerie, C. A. Spectroscopy of the hydrogen molecular ion. *Journal of Physics B: Atomic, Molecular and Optical Physics* **22**, 3551 (1989).
- [60] Carrington, A. *et al.* Spectroscopy of HD^+ in high angular momentum states. *Chem. Phys.* **166**, 145 – 166 (1992).
- [61] Carrington, A. *et al.* Microwave spectra of the D_2^+ and HD^+ ions near their dissociation limits. *J. Chem. Phys.* **98**, 5290–5301 (1993).
- [62] Carrington, A., Leach, C. A. & Viant, M. R. Nuclear hyperfine structure in the electronic millimetre wave spectrum of H_2^+ . *Chem. Phys. Lett.* **206**, 77 – 82 (1993).
- [63] Koelemeij, J. C. J., Roth, B., Wicht, A., Ernsting, I. & Schiller, S. Vibrational spectroscopy of HD^+ with 2-ppb accuracy. *Phys. Rev. Lett.* **98**, 173002 (2007).
- [64] Bressel, U. *et al.* Manipulation of individual hyperfine states in cold trapped molecular ions and application to HD^+ frequency metrology. *Phys. Rev. Lett.* **108**, 183003 (2012).

BIBLIOGRAPHY

- [65] Haase, C., Beyer, M., Jungen, C. & Merkt, F. The fundamental rotational interval of para- H_2^+ by MQDT-assisted Rydberg spectroscopy of H_2 . *J. Chem. Phys.* **142** (2015).
- [66] Fano, U. Quantum defect theory of l uncoupling in H_2 as an example of channel-interaction treatment. *Phys. Rev. A* **2**, 353 (1970).
- [67] Greene, C. H. & Jungen, Ch. Molecular applications of quantum defect theory. *Adv. At. Mol. Opt. Phys.* **21**, 51 (1985).
- [68] Cavendish, H. Experiments to determine the density of the earth. *Philosophical Transactions of the Royal Society of London* 469–526 (1798).
- [69] Salumbides, E. J. *et al.* Bounds on fifth forces from precision measurements on molecules. *Phys. Rev. D* **87**, 112008 (2013).
- [70] Salumbides, E. J., Ubachs, W. & Korobov, V. I. Bounds on fifth forces at the sub-Ångström length scale. *J. Mol. Spectr.* **300**, 65 – 69 (2014).
- [71] Arkani-Hamed, N., Dimopoulos, S. & Dvali, G. The hierarchy problem and new dimensions at a millimeter. *Phys. Lett. B* **429**.
- [72] Salumbides, E. J., Schellekens, A. N., Gato-Rivera, B. & Ubachs, W. Constraints on extra dimensions from precision molecular spectroscopy. *New J. Phys.* **17**, 033015 (2015).
- [73] Randall, L. & Sundrum, R. Large mass hierarchy from a small extra dimension. *Phys. Rev. Lett.* **83**, 3370–3373 (1999).
- [74] Randall, L. & Sundrum, R. An alternative to compactification. *Phys. Rev. Lett.* **83**, 4690–4693 (1999).
- [75] Biesheuvel, J. *et al.* Widely tunable laser frequency offset lock with 30 GHz range and 5 THz offset. *Opt. Express* **21**, 14008–14016 (2013).
- [76] Biesheuvel, J. *et al.* Probing QED and fundamental constants through laser spectroscopy of vibrational transitions in HD^+ . *Nat Commun* **7** (2016).
- [77] Earnshaw, S. On the nature of the molecular forces which regulate the constitution of the luminiferous ether. *Trans. Camb. Phil. Soc* **7**, 97–112 (1842).
- [78] Paul, W. Electromagnetic traps for charged and neutral particles. *Rev. Mod. Phys.* **62**, 531–540 (1990).

-
- [79] Dawson, P. H. *Quadrupole mass spectrometry and its applications* (Elsevier, 2013).
- [80] Gerlich, D. Ion-neutral collisions in a 22-pole trap at very low energies. *Physica Scripta* **1995**, 256 (1995).
- [81] Willitsch, S., Bell, M. T., Gingell, A. D. & Softley, T. P. Chemical applications of laser- and sympathetically-cooled ions in ion traps. *Phys. Chem. Chem. Phys.* **10**, 7200–7210 (2008).
- [82] Cirac, J. I. & Zoller, P. Quantum computations with cold trapped ions. *Phys. Rev. Lett.* **74**, 4091–4094 (1995).
- [83] Monroe, C., Meekhof, D. M., King, B. E., Itano, W. M. & Wineland, D. J. Demonstration of a fundamental quantum logic gate. *Phys. Rev. Lett.* **75**, 4714–4717 (1995).
- [84] Mermin, N. D. *Quantum computer science: an introduction* (Cambridge University Press, 2007).
- [85] Wineland, D. J. Nobel Lecture: Superposition, entanglement, and raising schrödinger's cat*. *Rev. Mod. Phys.* **85**, 1103–1114 (2013).
- [86] Perez, P. & Sacquin, Y. The GBAR experiment: gravitational behaviour of antihydrogen at rest. *Classical and Quantum Gravity* **29**, 184008 (2012).
- [87] Berkeland, D. J., Miller, J. D., Bergquist, J. C., Itano, W. M. & Wineland, D. J. Minimization of ion micromotion in a Paul trap. *J. Appl. Phys.* **83**, 5025–5033 (1998).
- [88] Denison, D. Operating parameters of a quadrupole in a grounded cylindrical housing. *Journal of Vacuum Science & Technology* **8**, 266–269 (1971).
- [89] Morigi, G. & Walther, H. Two-species Coulomb chains for quantum information. *The European Physical Journal D-Atomic, Molecular, Optical and Plasma Physics* **13**, 261–269 (2001).
- [90] Noom, D. W. E. A tunable frequency-stabilized laser for cooling and detection of beryllium ions in a trap (2011).
- [91] Rapp, D., Englander-Golden, P. & Briglia, D. D. Cross sections for dissociative ionization of molecules by electron impact. *J. Chem. Phys.* **42**, 4081–4085 (1965).

BIBLIOGRAPHY

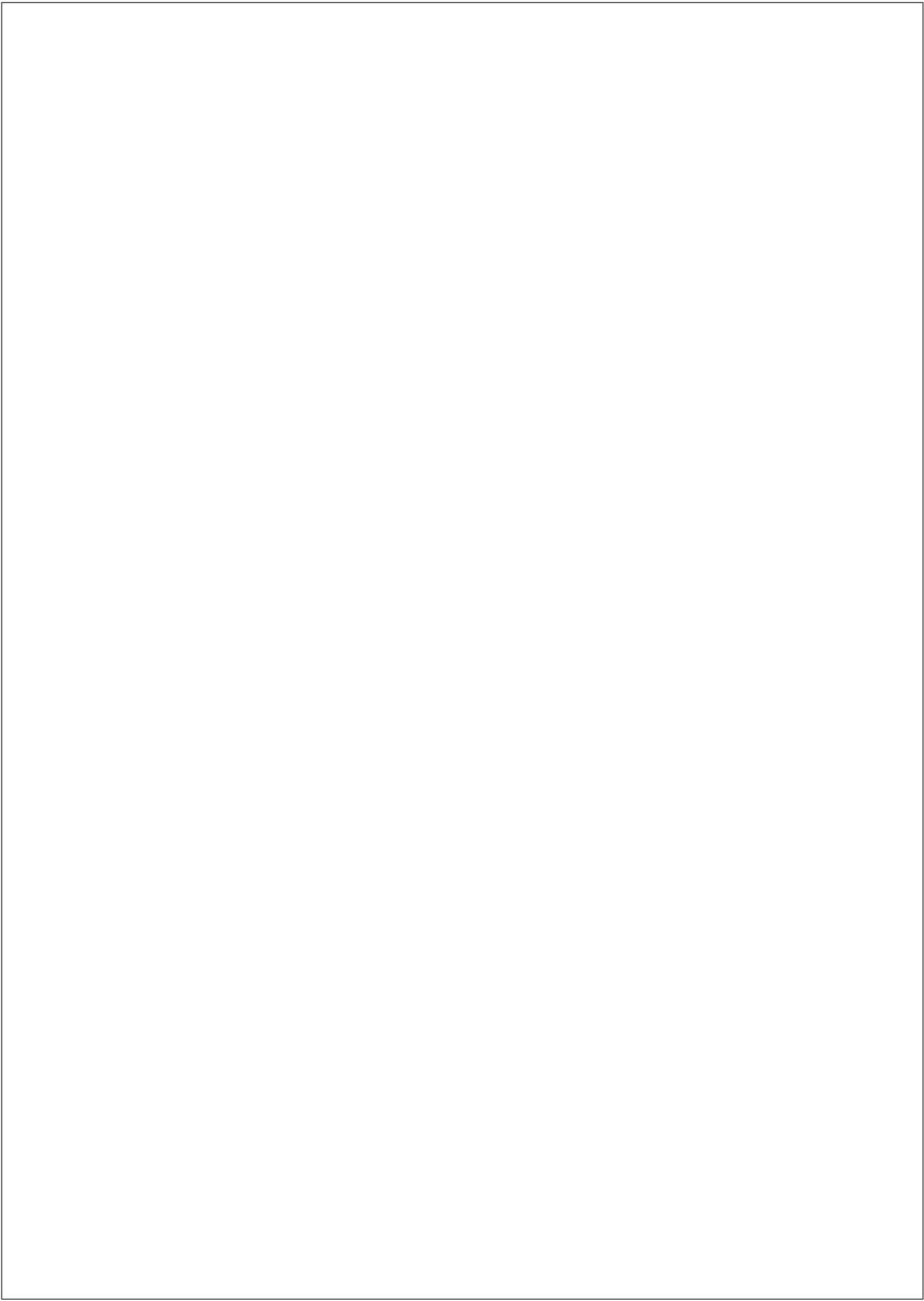
- [92] Hänsch, T. W. & Couillaud, B. Laser frequency stabilization by polarization spectroscopy of a reflecting reference cavity. *Opt. Comm.* **35**, 441–444 (1980).
- [93] Koelemeij, J. C. J., Noom, D. W. E., de Jong, D., Haddad, M. A. & Ubachs, W. Observation of the $v'=8 \leftarrow v=0$ vibrational overtone in cold trapped HD^+ . *Appl. Phys. B* **107**, 1075–1085 (2012).
- [94] Johnson, D. M. S., Hogan, J., S.-w. Chiow & Kasevich, M. A. Broadband optical serrodyne frequency shifting. *Opt. Lett.* **35**, 745–747 (2010).
- [95] Houtz, R., Chan, C. & Müller, H. Wideband, efficient optical serrodyne frequency shifting with a phase modulator and a nonlinear transmission line. *Opt. Express* **17**, 19235–19240 (2009).
- [96] Hisatake, S., Konishi, T. & Nagatsuma, T. Multiplication of optical frequency shift by cascaded electro-optic traveling phase gratings operating above 10 GHz. *Opt. Lett.* **36**, 1350–1352 (2011).
- [97] Haubrich, D. & Wynands, R. A modified commercial Ti:sapphire laser with 4 kHz rms linewidth. *Opt. Comm.* **123**, 558–562 (1996).
- [98] Schünemann, U., Engler, H., Grimm, R., Weidemüller, M. & Zielonkowski, M. Simple scheme for tunable frequency offset locking of two lasers. *Rev. Sci. Instrum.* **70**, 242 (1999).
- [99] Rohde, F. *et al.* A diode laser stabilization scheme for $^{40}\text{Ca}^+$ single-ion spectroscopy. *J. Phys. B* **43**, 115401 (2010).
- [100] Hänsch, T. W. Nobel lecture: Passion for precision .
- [101] Velchev, I., van Dierendock, R., Hogervorst, W. & Ubachs, W. A dense grid of reference iodine lines for optical frequency calibration in the range 571–596 nm. *J. Mol. Spectr.* **187**, 21–27 (1998).
- [102] Donley, E., Heavner, T. & Jefferts, S. R. Double-pass acousto-optic modulator system. *Rev. Sci. Instrum.* **67**, 063112 (2005).
- [103] Salumbides, E. J. *et al.* Improved potentials and Born-Oppenheimer corrections by new measurements of transitions of $^{129}\text{I}_2$ and $^{127}\text{I}^{129}\text{I}$ in the $B^3\Pi - X^1\Sigma_g$ band system. *Eur. Phys. J. D* **47**, 171–179 (2008).
- [104] Katô, H. *et al.* *Doppler-free high resolution spectral atlas of iodine molecule* (Japan Society for the Promotion of Science, 2000).

- [105] Knöckel, H., Boderman, B. & Tiemann, B. High precision description of the rovibronic structure of the I₂ B-X spectrum. *Eur. Phys. J. D* **28**, 199–209 (2004).
- [106] We used the "IodineSpec" program, kindly provided to us by H. Knöckel (Leibniz University, Hannover). See also B. Bodermann, H. Knöckel, and E. Tiemann, "Widely usable interpolation formulae for hyperfine splittings in the ¹²⁷I₂ spectrum," *Eur. Phys. J. D.* **19** 13-44 (2002).
- [107] S.-w. Chiow, Kovachy, T., H.-C. Chien & Kasevich, M. A. 102ħk large area atom interferometers. *Phys. Rev. Lett.* **107**, 130403 (2011).
- [108] Ozeri, R. *et al.* Errors in trapped-ion quantum gates due to spontaneous photon scattering. *Phys. Rev. A* **75**, 042329 (2007).
- [109] Bakalov, D., Korobov, V. I. & Schiller, S. *Phys. Rev. Lett.* **97**, 243001 (2006).
- [110] Brown, J. M. & Carrington, A. *Rotational spectroscopy of diatomic molecules* (Cambridge University Press, 2003).
- [111] Koelemeij, J. C. J. Infrared dynamic polarizability of HD⁺ rovibrational states. *Phys. Chem. Chem. Phys.* **13**, 18844–18851 (2011).
- [112] Hilborn, R. C. Einstein coefficients, cross sections, f values, dipole moments, and all that. *Am. J. Phys.* **50**, 982–986 (1982).
- [113] Cozijn, F. M. J. *et al.* Laser cooling of beryllium ions using a frequency-doubled 626 nm diode laser. *Opt. Lett.* **38**, 2370–2372 (2013).
- [114] Blythe, P., Roth, B., Fröhlich, U., Wenz, H. & Schiller, S. Production of ultracold trapped molecular hydrogen ions. *Phys. Rev. Lett.* **95**, 183002 (2005).
- [115] Roth, B., Koelemeij, J. C. J., Daerr, H. & Schiller, S. Rovibrational spectroscopy of trapped molecular hydrogen ions at millikelvin temperatures. *Phys. Rev. A* **74**, 040501 (2006).
- [116] Koelemeij, J. C. J., Roth, B. & Schiller, S. Blackbody thermometry with cold molecular ions and application to ion-based frequency standards. *Phys. Rev. A* **76**, 023413 (2007).
- [117] Schneider, T., Roth, B., Duncker, H., Ernsting, I. & Schiller, S. All-optical preparation of molecular ions in the rovibrational ground state. *Nat. Phys.* **6**, 275–278 (2010).

BIBLIOGRAPHY

- [118] Pollard, J. E., Johnson, L. K., Lichtin, D. A. & Cohen, R. B. State selected reactive scattering. $\text{H}_2^+ + \text{H}_2 \rightarrow \text{H}_3^+ + \text{H}$. *J. Chem. Phys.* **95**, 4877–4893 (1991).
- [119] Hasted, J. B. *Physics of Atom Collisions* (Butterworths, 1964).
- [120] Wineland, D. J. *et al.* Experimental issues in coherent quantum state manipulation of trapped atomic ions. *J. Res. Natl. Inst. Stand. Tech.* **103**, 259 (1998).
- [121] Giles, K., Adams, N. G. & Smith, D. A study of the reactions of trihydrogen(1+), H_2D^+ , HD_2^+ , and D_3^+ with hydrogen molecule, HD, and D_2 using a variable-temperature selected ion flow tube. *J. Phys. Chem.* **96**, 7645–7650 (1992).
- [122] Umarov, S., Tsallis, C. & Steinberg, S. On a q-central limit theorem consistent with nonextensive statistical mechanics. *Milan Journal of mathematics* **76**, 307–328 (2008).
- [123] Rouse, I. & Willitsch, S. Superstatistical velocity distributions of cold trapped ions in molecular-dynamics simulations. *Phys. Rev. A* **92**, 053420 (2015).
- [124] Chen, K., Sullivan, S. T., Rellergert, W. G. & Hudson, E. R. Measurement of the coulomb logarithm in a radio-frequency Paul trap. *Phys. Rev. Lett.* **110**, 173003 (2013).
- [125] Bakalov, D., Korobov, V. I. & Schiller, S. *J. Phys. B: At. Mol. Opt. Phys.* **44**, 025003 (2011).
- [126] Tran, V. Q., Karr, J.-Ph., Douillet, A., Koelemeij, J. C. J. & Hilico, L. Two-photon spectroscopy of trapped HD^+ ions in the Lamb-Dicke regime. *Phys. Rev. A* **88**, 033421 (2013).
- [127] Korobov, V. I. Relativistic corrections of $m\alpha^6$ order to the rovibrational spectrum of H_2^+ and HD^+ molecular ions. *Phys. Rev. A* **77**, 022509 (2008).
- [128] Mohr, P. J., Taylor, B. N. & Newell, D. B. CODATA recommended values of the fundamental physical constants: 2010. *Rev. Mod. Phys.* **84**, 1527–1605 (2012).
- [129] Farnham, D. L., Van Dyck, R. S. & Schwinberg, P. B. Determination of the electron's atomic mass and the proton/electron mass ratio via penning trap mass spectroscopy. *Phys. Rev. Lett.* **75**, 3598–3601 (1995).

-
- [130] Sturm, S. *et al.* High-precision measurement of the atomic mass of the electron. *Nature* **506**, 467–470 (2014).
- [131] Hori, M. *et al.* Two-photon laser spectroscopy of antiprotonic helium and the antiproton-to-electron mass ratio. *Nature* **475**, 484–488 (2011).
- [132] de Beauvoir, B. *et al.* Absolute frequency measurement of the $2S - 8S/D$ transitions in hydrogen and deuterium: New determination of the Rydberg constant. *Phys. Rev. Lett.* **78**, 440–443 (1997).
- [133] Beier, T. *et al.* New determination of the electron’s mass. *Phys. Rev. Lett.* **88**, 011603 (2001).
- [134] Verdú, J. *et al.* Electronic g factor of hydrogenlike oxygen $^{16}\text{O}^{7+}$. *Phys. Rev. Lett.* **92**, 093002 (2004).
- [135] Mohr, P. J., Taylor, B. N. & Newell, D. B. CODATA recommended values of the fundamental physical constants: 2006a). *Journal of Physical and Chemical Reference Data* **37**, 1187–1284 (2008).
- [136] Verlet, L. Computer ”experiments” on classical fluids. I. Thermodynamical properties of Lennard-Jones molecules. *Phys. Rev.* **159**, 98 (1967).
- [137] Wesenberg, J. H. *et al.* Fluorescence during Doppler cooling of a single trapped atom. *Phys. Rev. A* **76**, 053416 (2007).



Publications

This thesis is based on the following publications:

Chapter 3:

Widely tunable laser frequency offset lock with 30 GHz range and 5 THz offset
J. Biesheuvel, D. W. E. Noom, E. J. Salumbides, K. T. Sheridan, W. Ubachs
and J. C. J. Koelemeij
Optics Express 21, 14008-14016 (2013)

Chapter 4:

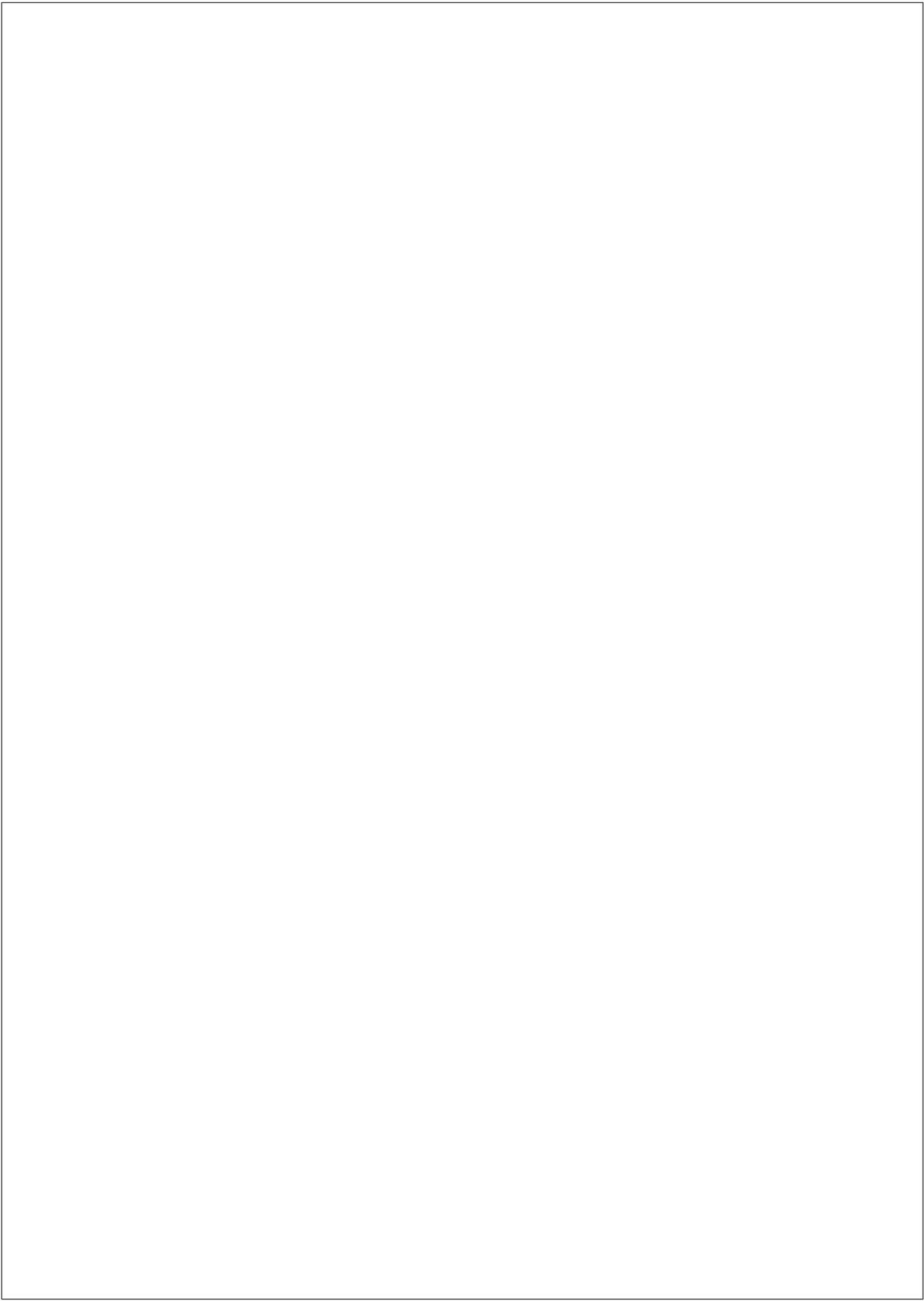
High-precision spectroscopy of the HD^+ molecule at the 1-p.p.b. level
J. Biesheuvel, J.-Ph. Karr, L. Hilico, K. S. E. Eikema, W. Ubachs
and J. C. J. Koelemeij
In preparation

Chapter 5:

Probing QED and fundamental constants through laser spectroscopy of vibrational transitions in HD^+
J. Biesheuvel, J.-Ph. Karr, L. Hilico, K. S. E. Eikema, W. Ubachs
and J. C. J. Koelemeij
Nat. Commun. 7:10385 doi: 10.1038/ncomms10385 (2016).

Other publications to which the author contributed:

- *Laser cooling of beryllium ions using a frequency doubled 626 nm diode laser*
F. M. J. Cozijn, J. Biesheuvel, A. S. Flores, W. Ubachs, G. Blume,
A. Wicht, K. Paschke, G. Erbert, and J. C. J. Koelemeij
Optics Letters 38, 2370-2372 (2013)



Summary

In the world of science, scientific theories are used to describe features in the observable world. Often, such theories can be empirically tested on their correctness. Practically, one takes an observable variable like the charge of an electron or the wavelength of a light ray, and if the predicted theoretical value of this variable agrees with the experimentally obtained value, the theory is indicated to be correct. In this research, the theory named quantum electrodynamics has been experimentally tested with very high precision. This theory describes the mutual interaction between electrically charged particles and their interaction with light. As all ordinary atoms and molecules in the universe contain electrically charged particles, most phenomena are at a fundamental level described by this theory.

This thesis describes a measurement which is carried out on one of the simplest known molecules, HD^+ , which only consist of two nuclei (a proton and a deuteron) a single electron. The variable compared to theory, is the required energy to bring the molecule in a state of vibration. This energy is delivered by an infrared laser which is directed at a bunch of HD^+ molecules in a laboratory setup. Such experiments, also called spectroscopy measurements, can be performed with very high accuracy, and in this case, a precision of less than one billionth is achieved.

In Chapter 1, the idea and motivation of this experiment are introduced, and a short summary of quantum electrodynamics is presented together with a historical overview of high precision measurements and high precision calculations on three body molecules.

During the experiment, HD^+ molecules are trapped in an ion trap and cooled down to a fraction above the absolute zero temperature ($-273.15\text{ }^\circ\text{C}$). The cooling is done indirectly by the use of very cold beryllium ions, which are cooled themselves with an ultraviolet laser. In Chapter 2, in which the setup of the experiment is described, the operation of the ion trap, lasers and the necessary electronic equipment is explained. In chapter 3 a new technique is presented which enables high speed tuning of the ultraviolet cooling-laser frequency over a large frequency range; this has been very useful during the experiment.

Chapter 4 is the core of this thesis and describes the spectroscopic measurement on HD^+ in detail. During the measurement some chemistry processes were involved which could not be characterized in the laboratory directly, but affected the result significantly. The effect of those processes onto the result is determined with the help of computer simulations using supercomputers of SURFsara.

By repeating a single HD^+ measurement almost two thousand times, sufficient data has been collected in order to obtain a spectroscopic result with an inaccuracy, as mentioned, of one about one billionth. This experimentally obtained value of vibrational energy in HD^+ agrees, within its uncertainty, with the theoretically predicted value. Therefore, we can conclude that the theory of quantum electrodynamics describes the system of HD^+ correctly onto the one part-per-billion level. This measurement is currently the most stringent test of quantum electrodynamics in an ordinary molecule.

In Chapter 5 the same experiment is explained in short and the spectroscopic result is used to determine a new value of the proton-to-electron mass ratio. Also new bounds are obtained on the presence of new physics, like the existence of ‘fifth forces’ between hadrons (particles like protons or neutrons). Furthermore a new upperlimit is given on the compactification radius of unobserved higher spatial dimensions.

Samenvatting

In de wetenschap is het gebruikelijk om theorieën die iets vertellen over de waarneembare wereld te testen op hun correctheid. Men neemt dan een meetbare variabele, zoals de elektrische lading van een deeltje of de golflengte van een lichtgolf en als een theoretisch voorspelde waarde van die variabele overeenkomt met de uitkomst van diezelfde meetbare variabele in een experiment, dan is dit een aanwijzing voor een correcte theorie. In het hier beschreven onderzoek is de theorie genaamd kwantumelectrodynamica experimenteel getest met een zeer hoge precisie. Deze theorie beschrijft de onderlinge interactie van elektrisch geladen deeltjes en hun interactie met lichtstralen. Aangezien alle atomen en moleculen elektrisch geladen deeltjes bevatten, komt het erop neer dat bijna alles wat men waarneemt op een fundamenteel niveau beschreven wordt door deze theorie.

Dit proefschrift beschrijft een meting verricht aan één van de simpelste moleculen, HD^+ , dat slechts bestaat uit een proton, deutron en een electron. De gemeten variabele die vergeleken wordt met de theoretische voorspelling is in dit geval de energie die nodig is om het HD^+ molecuul in een vibrationeel aangeslagen toestand te brengen. Deze energie wordt geleverd door een infraroodlaser die op een groepje HD^+ moleculen geschoten wordt. Zulk soort experimenten worden spectroscopie metingen genoemd en kunnen doorgaans zeer nauwkeurige resultaten opleveren. In dit geval is er een precisie gehaald beneden het niveau van één miljardste.

In Hoofdstuk 1 worden idee en motivatie van dit experiment gintroduceerd. Hier wordt een korte conceptuele samenvatting gegeven van de kwantumelectrodynamica en er wordt een historische uiteenzetting gegeven van hoge precisie metingen en berekeningen aan kleine moleculen zoals HD^+ .

Tijdens het experiment worden de HD^+ moleculen opgesloten in een zogenaamde ionenval zodat ze lang genoeg op hun plek blijven zitten voor het uitvoeren van de meting. Ondertussen worden ze afgekoeld tot een temperatuur van een fractie boven het absolute nulpunt ($-273.15\text{ }^\circ\text{C}$). Dit afkoelen gebeurt met behulp van beryllium ionen die zelf gekoeld worden met een ultravioletlaser. In Hoofdstuk 2, waarin de opstelling van dit experiment staat

beschreven, wordt de werking van de ionenval, de lasers, en benodigde elektronische apparatuur uitgelegd. In Hoofdstuk 3 wordt vervolgens een nieuwe techniek gepresenteerd, die het mogelijk maakt om de frequentie van de ultravioletlaser met hoge snelheid te tunen over een groot bereik. Dit is van groot nut gebleken tijdens de meting.

Hoofdstuk 4 is de kern van dit proefschrift waarin het spectroscopie experiment zelf tot in detail wordt beschreven. Tijdens de meting bleken er in de opstelling chemische processen aanwezig die het meetresultaat significant beïnvloedden, maar zelf niet gekarakteriseerd konden worden in het laboratorium. Het effect van deze processen is daarom bepaald met behulp van computersimulaties op de supercomputers van SURFsara.

Door een enkele meting aan het HD^+ molecuul bijna tweeduizend keer te herhalen, is er voldoende data verzameld om een relatieve nauwkeurigheid van rond de miljardste te halen, zoals hierboven al werd genoemd. Dit experimenteel behaalde resultaat komt, binnen de onzekerheidsmarge, overeen met de theoretische voorspelling. Hieruit kunnen we concluderen dat de kwantumelectrodynamica het HD^+ molecuul correct beschrijft tot op het niveau van een miljardste. Dit is tot op heden de meest nauwkeurige test van kwantumelectrodynamica die is uitgevoerd met behulp van een ‘gewoon’ molecuul.

Het laatste deel van dit proefschrift, Hoofdstuk 5, beschrijft dit experiment kort en er wordt uit het verkregen resultaat een nieuwe bepaling van de proton-electron massa verhouding geleverd. Daarnaast worden uit het resultaat nieuwe grenzen afgeleid van mogelijk aanwezige maar niet waargenomen fysica, zoals de hypothetische aanwezigheid van een vijfde fundamentele kracht tussen hadronen (deeltjes zoals protonen of neutronen). Daarnaast wordt er een nieuwe bovenlimiet gegeven voor de compactificatiestraal van hogere, niet waargenomen, ruimtelijke dimensies.

Acknowledgements

Firstly, I would like to thank my copromotor Jeroen Koelemeij and my promotor Wim Ubachs for their strong support and advice during this research. Thanks also to Laurent Hilico who provided an outstanding MD simulation code and Jean-Philippe Karr who helped me with some theoretical issues. I thank Albane Douillet for her great hospitality during my STSM visit in Paris. Furthermore, I am grateful to my fellow researchers Kevin Sheridan, Edcel Salumbides, Frank Cozijn, Jonas Morgenweg, Remy Notermans, Sayan Patra, Tjeerd Pinkert, and Subhadeep De, technicians Jacques Bouma and Rob Kortekaas, and electro-mechanical technicians Tim Kortekaas and Mario Moleenaar who all contributed to a well functioning laboratory HD⁺ experiment. I want to say thanks to everybody in Atomic, Molecular and Laser Physics Group for spending some good years at the VU University. At last, I would like to thank Elisa for her support. Elisa, ohne dich würde dieser Doktorarbeit überhaupt nicht geschrieben werden. Danke.